UNIVERSITY OF HELSINKI REPORT SERIES IN ASTRONOMY No. 3

Characterization of non-imaging semiconductor X-ray solar monitors

Lauri Alha

Department of Physics
Faculty of Science
University of Helsinki
Helsinki, Finland

ACADEMIC DISSERTATION

To be presented, with the permission of
the Faculty of Science of the University of Helsinki,
for public criticism in Auditorium 2 (A129)
A. I. Virtasen aukio 1 - Chemicum
on November 4, 2010, at 12 o'clock noon.

Helsinki 2010

Cover figure: *A visible solar corona during an eclipse (ESA).*

ISSN 1799-3024 (printed version)
ISBN 978-952-10-5985-8 (printed version)
Helsinki 2010
Helsinki University Printing House (Yliopistopaino)

ISSN 1799-3032 (pdf version)
ISBN 978-952-10-5986-5 (pdf version)
ISSN-L 1799-3024
http://ethesis.helsinki.fi/
Helsinki 2010
Electronic Publications @ University of Helsinki (Helsingin yliopiston verkkojulkaisut)

Abstract

The first observations of solar X-rays date back to late 1940's. In order to observe solar X-rays the instruments have to be lifted above the Earth's atmosphere, since all high energy radiation from the space is almost totally attenuated by it. This is a good thing for all living creatures, but bad for X-ray astronomers. Detectors observing X-ray emission from space must be placed on-board satellites, which makes this particular discipline of astronomy technologically and operationally demanding, as well as very expensive.

In this thesis, I have focused on detectors dedicated to observing solar X-rays in the energy range 1-20 keV. The purpose of these detectors was to measure solar X-rays simultaneously with another X-ray spectrometer measuring fluorescence X-ray emission from the Moon surface. The X-ray fluorescence emission is induced by the primary solar X-rays. If the elemental abundances on the Moon were to be determined with fluorescence analysis methods, the shape and intensity of the simultaneous solar X-ray spectrum must be known. The aim of this thesis is to describe the characterization and operation of our X-ray instruments on-board two Moon missions, SMART-1 and Chandrayaan-1. Also the independent solar science performance of these two almost similar X-ray spectrometers is described.

These detectors have the following two features in common. Firstly, the primary detection element is made of a single crystal silicon diode. Secondly, the field of view is circular and very large. The data obtained from these detectors are spectra with a 16 second time resolution. Before launching an instrument into space, its performance must be characterized by ground calibrations. The basic operation of these detectors and their ground calibrations are described in detail.

Two C-flares are analyzed as examples for introducing the spectral fitting process. The first flare analysis shows the fit of a single spectrum of the C1-flare obtained during the peak phase. The other analysis example shows how to derive the time evolution of fluxes, emission measures (EM) and temperatures through the whole single C4 flare with the time resolution of 16 s. The preparatory data analysis procedures are also introduced in detail. These are required in spectral fittings of the data.

A new solar monitor design equipped with a concentrator optics and a moderate size of field of view is also introduced.

Acknowledgments

I would like to express my gratitude to the supervisor of my thesis, Dr. Juhani Huovelin. I also wish to thank Dr. Lauri Jetsu for his supervision of the introduction of this thesis, as well as of Papers IV and V. I'm also grateful to all members of our research group for their advice and assistance in completing this thesis.
Special thanks are also given to the staff of the X-ray laboratory of the University of Helsinki for helping me in performing the calibration measurements for the SMART-1 and Chandrayaan-1 XSM instruments.
I would also like to acknowledge the detector manufacturer, Oxford Instruments Analytical for technical help and valuable advice.
This work has been largely supported by funding from the Academy of Finland. The agency for Technology and Innovation (TEKES) has financed the development of the XSM instrument for SMART-1, and ESA has financed the development of the XSM for Chandrayaan-1.
Finally, I want to thank my family.

Helsinki, September 30, 2010

Lauri Alha

Acronyms used in the text

Acronym	Description
ACIS	AXAF CCD Imaging Spectrometer
AR	Active Region
ARF	Ancillary Response File
AU	Astronomical Unit
BeppoSAX	Giuseppe "Beppo" Occhialini Satellite per Astronomia X
BoL	Beginning of Life
C1XS	Chandrayaan-1 X-ray Spectrometer
CH-1	Chandrayaan-1
D-CIXS	Demonstration of a Compact Imaging X-ray Spectrometer
EM	Emission Measure
EPIC	European Photon Imaging Camera
ESA	European Space Agency
EUV	Extreme Ultra-Violet
FET	Field Effect Transistor
FITS	Flexible Image Transport System
FM	Flight Model
FoV	Field of View
FS	Flight Spare
FWHM	Full Width at Half Maximum
GaAs	Gallium Arsenide
GTO	Geostationary Transfer Orbit
GOES	Geostationary Operational Environmental Satellite
HEASARC	High Energy Astrophysics Science Archive
HK	House Keeping
HP	High Purity
HV	High Voltage
IDL	Interactive Data Language
ISRO	Indian Space Research Organization
LMSAL	Lockheed Martin Solar & Astrophysics Labs
MCA	Multi Channel Analyzer
MESSENGER	MErcury Surface, Space ENvironment, GEochemistry, and Ranging
MHD	Magneto Hydro Dynamics
MPO	Mercury Polar Orbiter
NASA	National Aviation and Space Administration
NEAR	Near Earth Asteroid Rendezvous
NOAA	National Oceanic and Atmospheric Administration
OF	Obscuration Factor
OIA	Oxford Instruments Analytical
PIN	Positive-Intrinsic-Negative
QE	Quantum Efficiency
RAL	Rutherford Appleton Laboratory
RESIK	REntgenovsky Spektrometr es Izognutymi Kristalami
RHESSI	Reuven Ramaty High Energy Solar Spectroscopic Imager
RMF	Redistribution Matrix File
SEM	Space Environment Monitor
SIXS	Solar Intensity and particle X-ray Spectrometer
SMART-1	Small Missions for Advanced Research in Technology-1
SOHO	Solar and Heliospheric Observatory
SoXS	Solar X-ray Spectrometer
STEREO	Solar TErrestrial RElations Observatory
S/W	Soft Ware
SXI	Solar X-ray Imager
SXT	Soft X-ray Telescope
TRACE	Transition Region and Coronal Explorer
XMM	X-ray Multi Mirror
XRT	X-Ray Telescope
XSM	X-ray Solar Monitor

Contents

1 Introduction

1.1 A brief history of the study of solar corona

The origin of solar coronal emission was a mystery during the early era of spectroscopic photography in the late 18th century. The photographs of coronal spectrum during a total eclipse showed a strange emission line in the green region of the electromagnetic spectrum at about 530.3 nm. A photograph of a total solar eclipse is illustrated in Fig. 1.

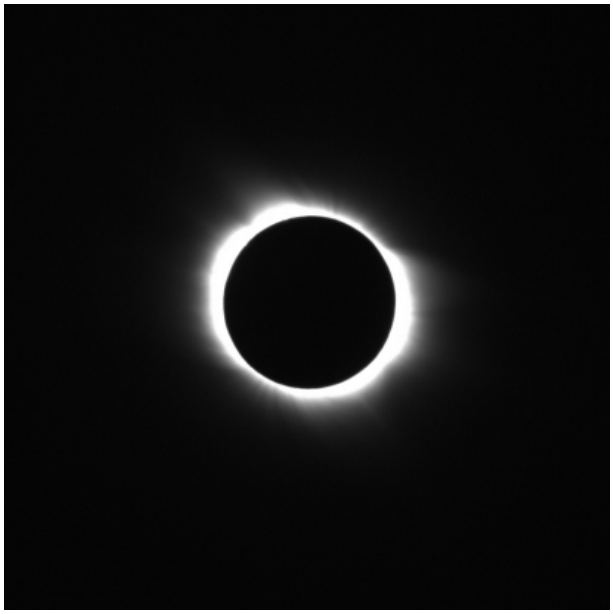

Figure 1: *A photograph of a total solar eclipse (ESA).*

This green line did not correspond to that of any known material and it was proposed that the line belonged to an unknown element. This hypothetical new element was provisionally named "Coronium". This name referred to the solar corona, like the name "Helium" referring to the Greek word for Sun, Helios. The green emission line was the first hint of the extremely high temperatures within solar corona, but it took several decades to understand the connection between this line and high temperature. There also was one other physical phenomenon, which indicated that the Sun was also radiating very energetic photons invisible to human eyes. In 1901, G. Marconi's first transatlantic wireless radio experiment revealed that there must be a reflecting layer higher in the atmosphere. The propagation of radio waves was supposed to obey a straight line in a homogeneous medium. Due to the curvature of the Earth's surface, the radio signals should have propagated into the empty space without being received on the opposite coast line at the distance of about 3000 km. The transmission would not succeed without reflections in the upper atmosphere. Two pioneers of the theory of electricity, Kennely and Heaviside, suggested independently that there must exist a conductive layer at about 100 km above the ground level, which made Marconi's experiment possible. This raised a new question of the origin of this conductive ionized layer. The potential high energy radiation coming from the Sun was correctly under investigation as the reason for the ionization in the upper atmosphere. Unfortunately, there were no direct methods to observe and verify the solar EUV- or X-ray emission at that time. The era of rockets started in late 1940's. The green coronal forbidden emission line was identified to originate from a highly ionized iron by I.S Bowen in 1927 (Bowen 1927). The ion Fe XIV is stripped of 13 electrons of its total of 26. W. Grotrian and B. Edlen were the first to understand that the solar coronal spectrum

shows highly ionized emission lines of iron corresponding to a temperature of a million K or more (Culhane & Sanford 1981). It was an extreme and radical idea to suggest that the coronal plasma temperature could reach 10^6 K, because the photospheric temperature is below 6000 K. The invention of the coronagraph by B. Lyot in 1939 (Lyot 1939) was also essential in the spectral analysis of this coronal line. The high temperature of the solar corona motivated astronomers to start developing instruments and practical methods for observing possible X-ray emission from the Sun.

1.2 Observing solar coronal X-ray emission

The first successful attempt to observe the solar X-ray emission was carried out in 1948 by T. Burnight with the aid of an Aerobee rocket. The detector element on-board this sounding rocket was a soft X-ray sensitive photographic emulsion plate fixed behind a beryllium filter. After the parachute descend, the film was investigated and was found to have been exposed by solar X-rays. The exposed X-ray film did not include any spatial or spectral information on the Sun, but it is regarded as a starting point of the era of X-ray astronomy. The first X-ray photograph with spatial resolution was taken with a pinhole camera designed by R.L. Blake in 1960 (Blake et al. 1963). The camera obscura system used in this particular experiment is shown in Fig. 2. A detailed theoretical study of the physics of the solar corona can be found in (Parker 1958).

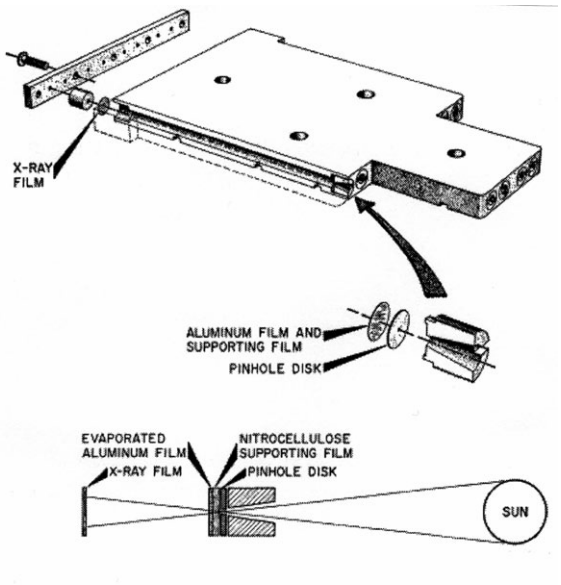

Figure 2: *The pinhole camera assembly applied in the first X-ray image of the Sun. This camera had several pin holes with different focal lengths (Blake et al. 1963).*

The Sun has since been observed over a wide spectral range by ground-based telescopes and instruments on-board satellites. There are currently several on-going missions observing solar X-ray and EUV radiation. These include GOES program satellites (Data 1996), SOHO (Delaboudinière et al. 1995), RHESSI (Lin et al. 2002), TRACE (Handy et al. 1999), STEREO (Howard et al. 2002) and HINODE (Kosugi et al. 2007). The Chandrayaan-1 (Bhandari 2005) mission equipped with our XSM was terminated in August 2009. The GOES program has 2 fully operational satellites and one satellite is in a standby mode currently. Each of the satellites carries a space environment monitor (SEM)

including an X-ray detector. GOES SEM detectors measure X-rays in two overlapping energy ranges. The author of this thesis has had an interest in the GOES lower X-ray band of 1.55-12.4 keV, because our solar monitors operated in roughly same energy range. The GOES X-ray data can be freely accessed and several flux comparison analyzes have been carried out between GOES SEM and SMART-1 XSM data. Two of the GOES satellites also have a solar X-ray imager (SXI) instrument equipped with Wolter optics (Hill et al. 2005). The SOHO, TRACE and STEREO satellites operate mainly in the EUV band, whilst the RHESSI satellite is a hard X-ray and gamma-ray observatory operating mainly above 10 keV. The imaging is based on multilayer optics in the telescopes of SOHO, TRACE and STEREO. The imaging technique of the RHESSI telescope utilizes a novel rotating collimator system reaching a spatial resolution of $2''$. The instrument under consideration in this thesis is the XSM (X-ray Solar Monitor). The detector of XSM is a single pixel spectrometer without imaging capabilities. Two XSM instruments developed by our team at the University of Helsinki have been launched since 2003. A third instrument with similar X-ray detectors is being developed for BepiColombo (Huovelin et al. 2009) taking into account the experience obtained from the SMART-1 and Chandrayaan-1 missions. There are also at least two other planetary missions with a similar X-ray spectrometer for solar observations, NEAR (Starr et al. 2000) and MESSENGER (Schlemm et al. 2007).

1.3 XSM compared to the existing solar X-ray instruments

The main improvement of our solar monitors with respect to former solar observing X-ray instruments is the capability to measure the solar spectral continuum and line emission simultaneously during a relatively short integration time (16 s). Both detectors include 512 energy channels, which enables them to operate as spectrometers with good energy resolution (200 eV FWHM or less at 5.9 keV). The operational energy range of the solar monitors is wide, covering from 1.8 keV to 20 keV. The dynamic range is also large and enables observations of solar X-ray fluxes from the A-glass flares up to the X-level flares with one static aperture and filter assembly. The instrument background is insignificant due to the small size of the detectors. Despite of the large detector FoV, the diffuse sky background count rate is less than 2 % of the total count rate even at a quiescent solar activity. The operation was pointing free due to the large FoV (*Field of View*). Our solar monitors measured the X-ray Sun like space borne astrophysical X-ray observatories, (e.g. XMM Newton and Chandra) measure stars. Hence the solar coronal data obtained by XSM can be compared with the coronal X-ray emission of distant active stars observed by XMM/EPIC and Chandra/ACIS. Thus, the solar coronal analysis can be used to interpret X-ray observations of other late-type stars, i.e. gaining further understanding of the so-called "solar-stellar connection" (Orlando et al. 1998).

1.3.1 Similar single crystal PIN detectors used in other missions

The Si PIN (*Positive Intrinsic Negative*) detector on-board the NEAR mission was similar to ours, but the performance was not as good. The energy resolution of the NEAR PIN was about 600 eV FWHM at 5.9 keV, which is 3 times worse that of our PINs. The thickness of the beryllium window in the NEAR Si-PIN was 76μm, which increased the practical low energy limit to above 2 keV. The effective area was 0.1 mm^2. The NEAR PIN failed during the cruise phase due to charge build-up in the SiO_2 surface layer (Starr et al. 1999) caused by solar wind electron flux. There was also a gas detector on the NEAR for the solar flux measurements, which had a lower energy resolution.

A similar Si-PIN photo-diode spectrometer on-board the MESSENGER has an energy resolution of about 300 eV FWHM at 5.9 keV. The aperture PIN hole diameter is 0.2 mm (corresponds to an effective area of 0.03 mm^2) and the Be-window thickness is 75μm. Unfortunately, the author couldn't find any papers describing the scientific performance of the MESSENGER PIN spectrometer for comparison purposes. The only performance related information was found on the Internet (Dennis & Starr 2008). The spectral fit of the MESSENGER X-ray spectrometer (*XRS*) data obtained during a M2-glass flare is shown in Fig. 3. This data is of about the same quality as that of obtained by our XSMs. The only drawback in the quality of the data obtained by the XRS, is the lack of an in-flight calibration source. This may cause problems in the determination of the energy scale.

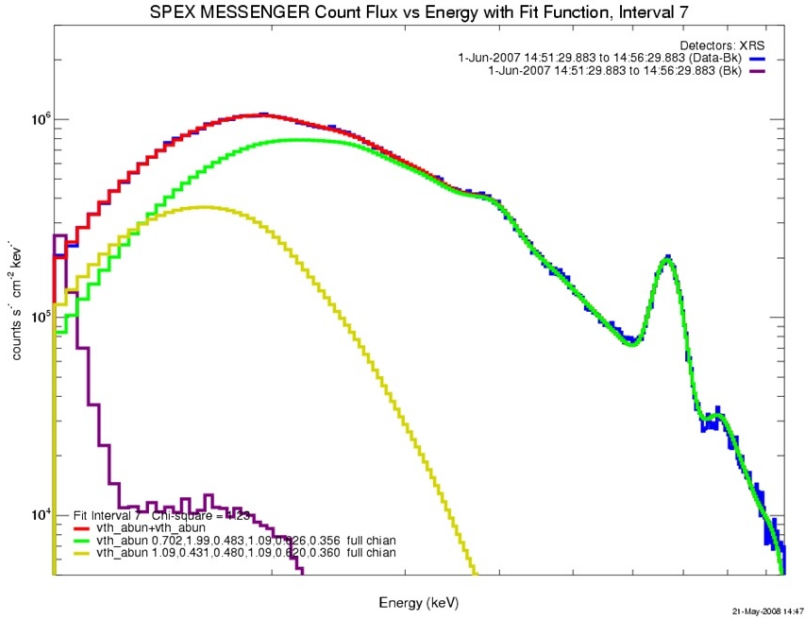

Figure 3: *MESSENGER XRS spectrum with thermal best-fits made. Blue histogram: background-subtracted X-ray count-rate spectrum measured with XRS at the epoch of peak temperature during the flare starting at 14:30 UT on 1 June 2007. Green and yellow curves: predicted line-plus-continuum thermal spectra that were summed (red curve) to give the best fit to the data. Purple histogram: pre-flare background spectrum (Dennis et Starr 2008). The emission line between 6 and 7 keV belongs to highly ionized iron atoms.*

Two similar Si PIN spectrometers were also on-board the Indian GSAT-2 satellite launched on 8 May 2008. These Solar X-ray Spectrometer (SoXS, Low energy) detectors monitored solar X-ray flux at the energy range of 4-25 keV with a energy resolution of 700 eV FWHM at 6.0 keV (Jain, Dave & Desphande 2001). The Be window thicknesses were 25.4 μm. No description about the SoXS aperture sizes was given in the available publications (Jain, Bhatt & Bharti 2001). The SoXS data analysis is in principle similar to our XSM data analysis, including the determination of the emission measure (*EM*), plasma temperature T_p and line intensities of the solar thermal plasma.

1.3.2 Bragg crystal spectrometers

Solar X-ray emission lines have been observed with Bragg crystal spectrometers since the late 1960's and plenty of elements with different ionization stages have been found within solar corona. There are three major limitations related to the Bragg crystals used in solar X-ray observations. The first feature is the low reflectance of the Bragg crystal at high photon energies, which limits the practical upper energy to about 6 keV. Secondly, Bragg crystals need to be movable in front of the detector to optimally adjust the reflection angle for different emission lines. Bragg crystals do not measure the continuum simultaneously with the lines. The thermal continuum spectrum has generally been difficult to measure, because of fluorescence radiation from the Bragg-scattering crystals. An example of a solar X-ray spectrum composed of simultaneous observations of RHESSI (above 3 keV) and CORONAS-F RESIK (2.0-3.7 keV) Bragg spectrometer (Dennis et al. 2005) on 2003 April 23 03:00 UT is shown in Fig. 4. The energy resolution of RHESSI is about 1.0 keV FWHM in the range of 3-10 keV and the respective ADC channel width is 330 eV. Thus, line spectroscopy appears challenging at soft X-ray wavelenghts using RHESSI data.

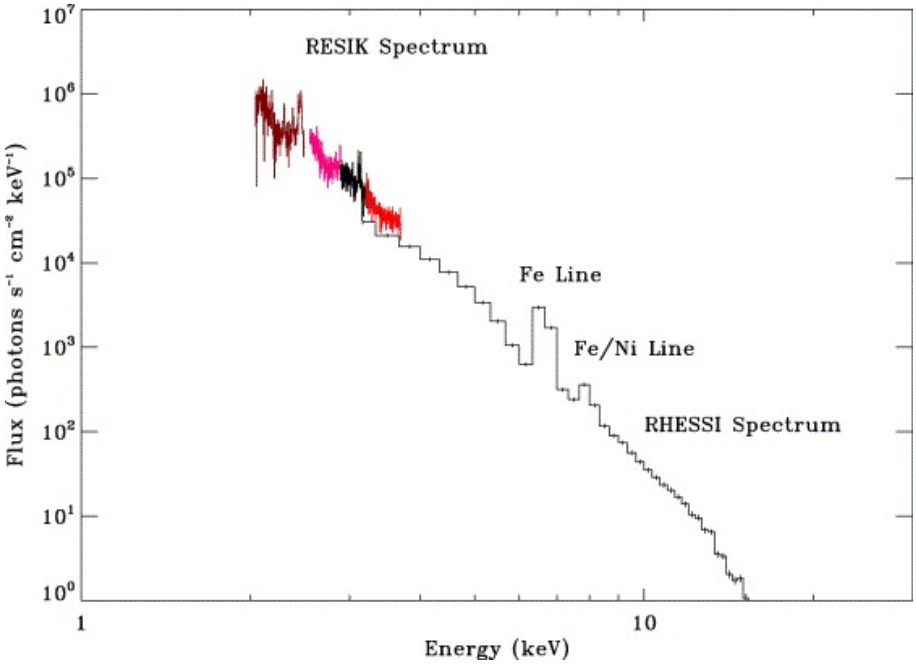

Figure 4: *Combined RHESSI and RESIK (Dennis et al. 2005) solar spectrum. The spectral thermal parameters for this fitted data are T=18.6 MK and EM=2.1E47 cm^{-3}. The simultaneous lower band GOES flux was 1.5E-6 Wm^{-2}. This agrees well with the C-flare data obtained with XSM (See section 6.3.2).*

1.3.3 XSM versus GOES Space Environment Monitors

The GOES SEM X-ray detectors observe solar X-ray emission at two overlapping bands. The lower band covers the energy range 1.55-12.4 keV and the hard band covers energies 3.12 to 25.01 keV. The plot in Fig. 5. illustrates these two on-line fluxes obtained from the GOES data website (www.swpc.noaa.gov/r_plots/Xray _1m.gif). However, the GOES SEM detectors are not X-ray spectrometers, but perform their task as flux monitoring devices, i.e. photometers very accurately, at least in the lower energy band, as was confirmed by our flux cross calibration with the SMART-1 XSM.

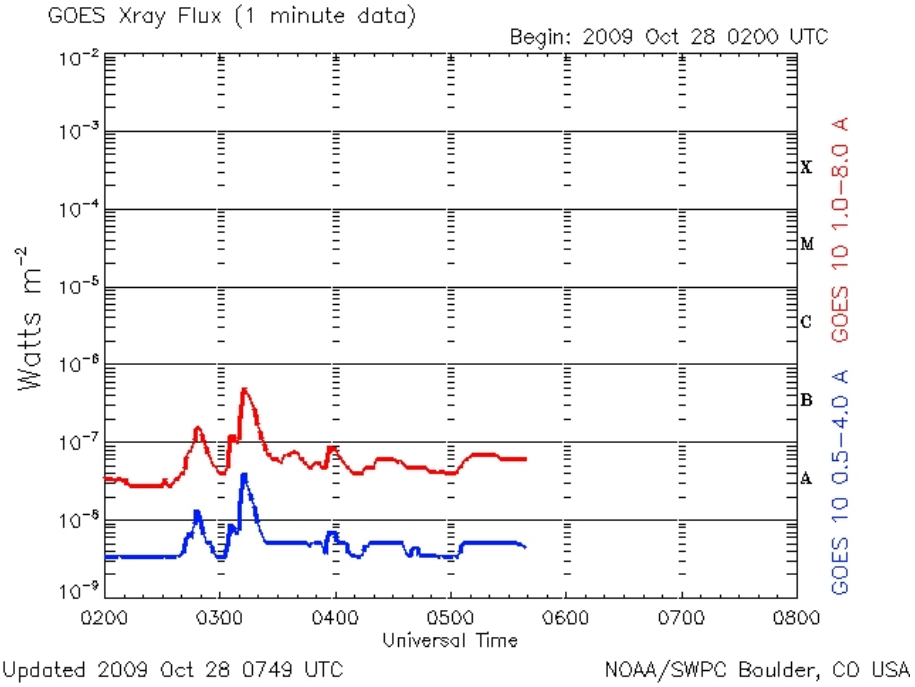

Figure 5: *The GOES SEM X-ray flux data with time resolutions of 1 and 5 min can be freely accessed on Internet. The above plot illustrates the GOES-10 satellite SEM on-line flux data, updating at a time interval of 1 min (www.swpc.noaa.gov/r_plots/Xray_1m.gif).*

1.3.4 Solar X-ray telescopes

X-ray telescopes with Wolter type 1 optics, enable imaging of the Sun at soft X-ray band. These instruments provide high resolution images of the X-ray Sun taken at different temperatures. The HINODE X-ray Telescope (XRT) is the state of a art device among the on-going solar missions (DeLuca et al. 2005). Solar magnetic structures can be resolved with a spatial resolution of 2.0", corresponding to a distance of about 1500 km on the solar disc. A GOES SXI image of the X-ray Sun is shown in Fig. 6. Despite of the high quality imaging performance, the coronal temperature information is derived roughly with two focal plane wheels containing 9 different X-ray filters in total. The low energy cut-off can be changed by filtering and one integration requires the use of several different filter configurations to enable diagnostics of the isothermal plasma. The specified XRT temperature range is $6.1 < \log T < 7.5$ ($\approx$ 1.3 - 31.6 MK), with a temperature discrimination of $\Delta \log T = 0.2$, i.e. the energy resolution at 2.0 keV ($\approx$ 23.2 MK) is 1260 eV ($\approx$ 14.6 MK). The XRT energy resolution is an order of magnitude lower than in our solar monitors. (It is worth to remember that 1eV is equal to 11600K.)

1.4 The Sun as an X-ray star

The average solar X-ray luminosity is about one millionth of the total luminosity of the Sun. The source of the solar X-ray emission originates in the extremely hot, but low density plasma of the corona (Giacconi & Gursky 1974). The coronal heating mechanism has been a big puzzle to solar physicists, since the coronal temperature was measured in late 1930's. The coronal heating is connected to the activity of the Sun, where the solar magnetic field plays a major role.

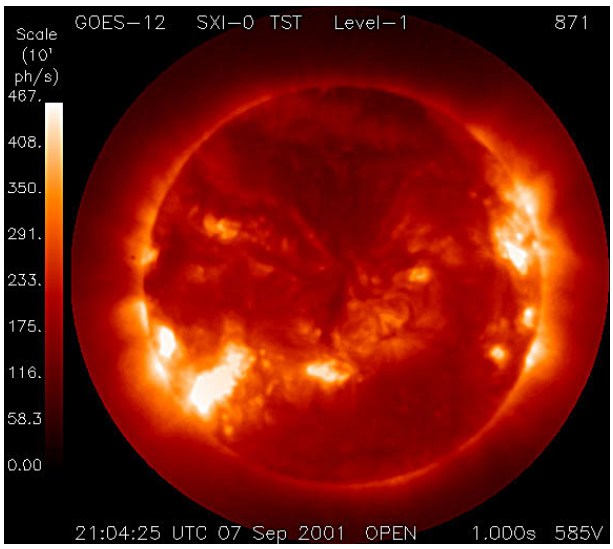

Figure 6: *The first GOES-12 SXI X-ray image of the Sun on 7 September 2001. The solar flux at GOES SEM lower range was 2.0E-06 Wm^{-2}. No focal plane filter was used during this exposure. Hence the photographic brightness corresponds to the X-ray intensity obtained in the energy range 0.2-2.0 keV (NOAA).*

1.4.1 Solar activity

The solar activity is a manifestation of the magnetic field originating from the solar convective zone. The magnetic field is caused by the so-called solar dynamo. The magnetic dynamo is maintained and amplified by differential rotation and turbulence in the outer convective zone of the Sun and other stars with a similar structure. This phenomenon has been modeled with Magneto Hydro Dynamics, e.g. (Yoshimura 1992). The MHD analysis of the solar dynamo is a very complex subject, and beyond the scope of this thesis. A simple qualitative description of the behavior of stellar dynamos could be as follows. The more rapidly a star rotates and the deeper is the convective zone, the more active a star is, i.e. the stronger is the dynamo effect and the generated magnetic field. Visual manifestations of the solar activity and magnetic field are the sunspots. Sunspots are created by the magnetic flux ropes swelling out of the photosphere and they have about 1000 K lower temperature than the surrounding photosphere. This is also the reason for their apparent darkness. The differential rotation elongates the magnetic field lines, which are frozen in the plasma and the radial convective motion causes them to finally break through the photosphere. This gives rise to dark sunspots and bright plage areas within the active areas in the solar atmosphere. Long term observations of the visual Sun have shown that the sunspot cycle is on the average about 11 years, but the length has varied between 8 and 15 years (Eddy 1980). The sunspot maximum represents the peak of the solar magnetic activity, while the minimum corresponds to the Sun without spots. Active regions contribute to the total X-ray emission of the Sun. The size of the solar corona depends on the activity level of the Sun. During low activity the visible corona is also weak, as shown in Fig. 1. When the activity of the Sun is strong, the corona can extend several solar radii above the photosphere. The most significant manifestations of the coronal activity are flares. The reason of strong enhancements in X-ray and Gamma-ray emission associated with a flare is the powerful heating of the gas due to magnetic reconnection, e.g. (Huovelin 2006) and references therein.

1.4.2 Solar coronal X-ray emission mechanisms

The solar corona is composed of a thin hot thermal plasma. Free electrons and ions interact with each other to produce X-rays in several different ways. X-rays in solar corona are produced via several processes. 1) A free electron approaching an ion decelerates under the Coulomb force and emits Bremsstrahlung, i.e free-free emission. This radiation falls in the soft X-ray band in the solar corona, where the plasma temperature is above 1MK. 2) Free-bound, i.e. radiative recombination emission is another process producing continuum X-ray emission in the solar corona. In this process a free electron is captured into a vacant quantum shell of the ion. 3) A third X-ray radiation mechanism is line emission. In this case, the incoming electron excites a bound electron to a new energy level. This excitation releases a photon when the bound electron falls back to its unexcited state. The energy of the photon corresponds to the energy difference between the excited and original level. These three processes dominate the X-ray emission of the solar corona. The shape and intensity of the solar coronal X-ray spectrum depends strongly on the plasma temperature and the elemental abundances. The most simple physical model of the X-ray emission originating from the solar corona assumes a thermal equilibrium and is fully characterized with one temperature, electron density and fixed elemental abundances. The X-ray activity of the Sun has a strong temporal and spatial variability. The lowest X-ray brightness occur in coronal holes, where the open magnetic field lines stream out to outer solar system producing solar wind. They are also cooler and less dense regions containing arc-like magnetic closed filament cavities with low X-ray emission. As mentioned earlier, the active regions exhibit bipolar magnetic loop structures, containing hotter and more dense plasma. The solar corona also contains X-ray bright points, e.g. (Vilhu et al. 2002), which are smaller in size and have shorter life time. The most extreme X-ray outbursts are related to the flare events. Here a magnetic loop heats up and expands forming a neutral sheet, which causes magnetic reconnection (Culhane & Sanford 1981). At this region, the magnetic energy heats the surrounding plasma and converts the non-thermal energy into kinetic energy of different ions and electrons.
According to our experience, the X-ray spectrum of small flares up to C-level can be modeled with a single temperature at the soft X-ray range (1-10 keV). The plasma temperature can vary between 1-100 MK depending on the magnitude of the flare event. The hard X-ray spectrum of the flare above 10 keV must also include a non-thermal model component, e.g. a power law model. The non-thermal emission is caused by the acceleration of electrons and ions colliding with the more dense material in the foot-point of a loop. The emission lines of highly ionized elements are seen in the flare spectra, like Helium (FeXXVI) and Hydrogen (XXVII) like iron ions. The loop like magnetic field lines observed in EUV wavelengths are clearly seen in Fig. 7. The X-ray luminosity of the Sun can vary several orders of magnitude. Table 1 compiles the standard solar flare intensity scale applied in the GOES observations. The flux is measured in the energy range from 1.55 to 12.4 keV.

1.5 The aim of the thesis

We have designed two X-ray Solar Monitors on-board the SMART-1 and CH-1 satellites missions to the Moon. The launch of the SMART-1 S/C was on September 27th, 2003 (Racca et al. 2002). The CH-1 satellite was launched on October 22nd, 2008. This thesis describes the characterization of the performance of non-imaging semiconductor X-ray solar monitors launched on-board these two satellites. The characterization relies on the ground calibrations, which were mainly carried out at the X-ray laboratory of the De-

Level	Intensity, Wm^{-2}
Y	10^{-3}
X	10^{-4}
M	10^{-5}
C	10^{-6}
A	10^{-7}
B	10^{-8}

Table 1: *GOES standard intensity scale for solar flares.*

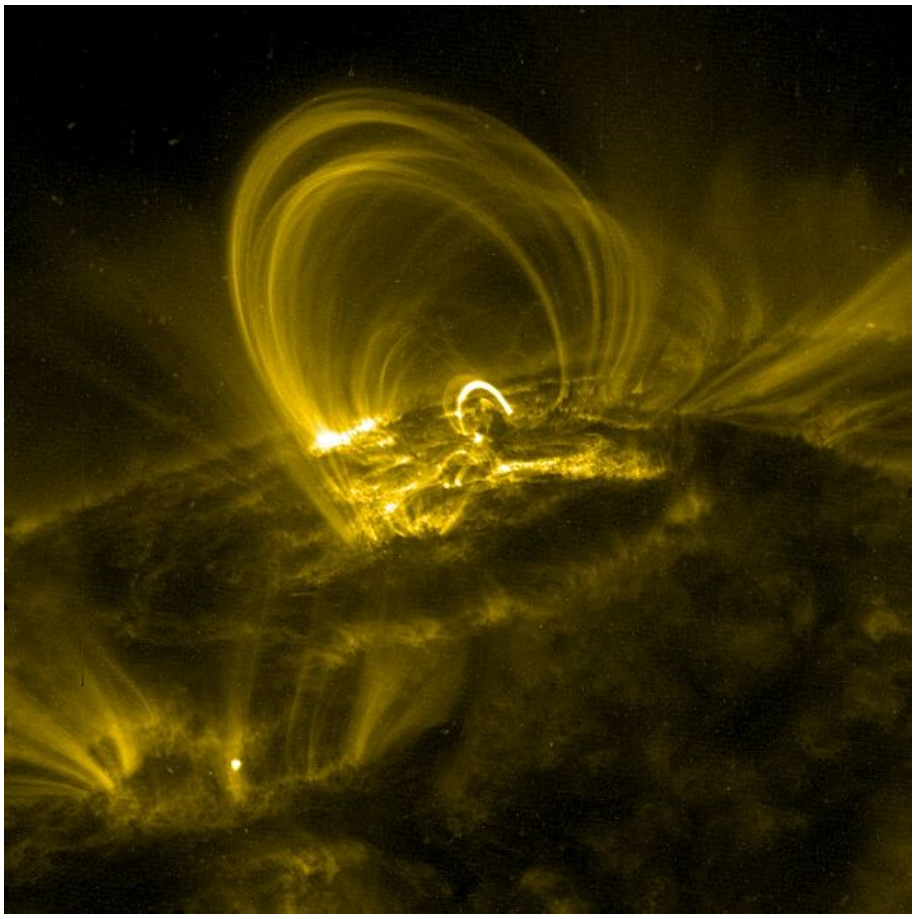

Figure 7: *Solar magnetic field loop structures at 171 Å wavelength (Fe IX) located on the Active Region 10808 observed by TRACE 6 hours after the peaking of an X17-flare on 5 September 2005 (LMSAL).*

partment of Physics of University of Helsinki. Some simple tests, which did not require vacuum conditions, were made at the manufacturer's (OIA) facilities. Chapter 2 gives a short introduction of a basic operation of a semiconductor X-ray spectrometer. The description of the mutual operation and performance of both solar monitor and Moon fluorescence detector are given in Chapter 3. Chapter 4 deals with the ground calibration methods applied. Chapter 5 describes briefly the in-flight operation of our XSMs on-board SMART-1 and CH-1 satellites. Some examples of the SMART-1 XSM data analysis are given in Chapter 6. A brief summary of the publications included into this thesis is given in Chapter 7. Concluding remarks and future prospects are presented in Chapter 8. The general method for calculating the geometric detector area for wide circular FoV solar monitors is given in Appendix 1.

2 Basics of the operation of semiconductor detectors

There is a variety of different solid state semiconductor materials. The HP (*High Purity*) silicon semiconductor PIN (*Positive-Intrinsic-negative*) diodes are described here, because our XSM detectors were equipped with Si PINs. Silicon is perhaps the most commonly used semiconductor material due to its rich abundance on the Earth, i.e. it is an inexpensive material. The production of high quality epitaxial high purity Si wafers is much more easier the than fabrication of, e.g. GaAs crystals. However, silicon detectors are much more vulnerable to the space particle bombardment than several high density compound semiconductors, like GaAs, e.g. (Owens et al. 2002). Despite this complication, Si is commonly used in space instruments. To enhance the operational life-time of a silicon detector, the diode can be shielded with a shutter mechanism. Silicon chips are suitable detector elements in the soft X-ray range between 1-20 keV. The detector chip thicknesses are less than 1 mm, when operating at the soft X-ray band. The properties of silicon are listed in Table 2.

Atomic number	Z	14
Atomic weight	M	28.09 g/mol
Mean energy of Kα lines	-	1740 eV
Crystal structure	-	Diamond
Lattice constant	a	5.43 Å
Atomic density	n	5.00 x 10^{22}
Density	ρ	2.328 g/cm^3
Static dielectric constant	ϵ	11.9
Energy band gap	$E_{\rm g}$	1.12 eV
Mean pair-creation energy	w	3.62 eV
Fano factor	F	$\sim$ 0.15 at 3 keV

Table 2: *Properties of a silicon atom and single-crystal silicon at 300K.*

2.1 Structure of a silicon PIN diode

Crystalline silicon is an intrinsic semiconductor, whose conductivity can be controlled by doping it with impurity atoms having 3 or 5 valence electrons, i.e. one more or one less than the 4 valence electrons in a silicon atom. The two most commonly used impurity elements are boron with three valence electrons and phosphorous with five valence electrons. Inside a silicon lattice, impurity atoms like phosphorous act as an N-type donor. The fifth phosphorous valence electrons do not fit into the Si lattice and those become free (N) negative charge carriers. Boron atoms with three valence electrons establish a P-type acceptor into the Si lattice. Boron atoms with electron deficiency act as positive charge carriers, i.e. holes. In a silicon PIN diode, one side of the Si chip is doped with boron atoms to form an N-type semiconductor, while the opposite side is doped with phosphorous atoms to form a P-type semiconductor. The volume between P-and N-layers has a finite extent of free charge carriers, i.e. it becomes (I) intrinsic having a high resistance (Sze 1981). The surplus electrons from N-type material diffuse into P-type material and surplus holes diffuse from P-type material into N-type material until a surplus of electrons occur in the in the P volume and *vice versa*. The rest of the free charge carriers are removed from the intrinsic region by applying an electric field across the P-N junction.

The intrinsic volume between the PN-junction is called a depletion region, which is the active detecting volume. The depletion layer is kept clean from holes and free electrons by applying an reversed high voltage across the P-N junction. These PIN diodes must be cooled down below -10°C to reduce thermally generated charge carriers, i.e. noise in the P-N junction. The schematic structure of a silicon PIN diode is shown in Fig. 8.

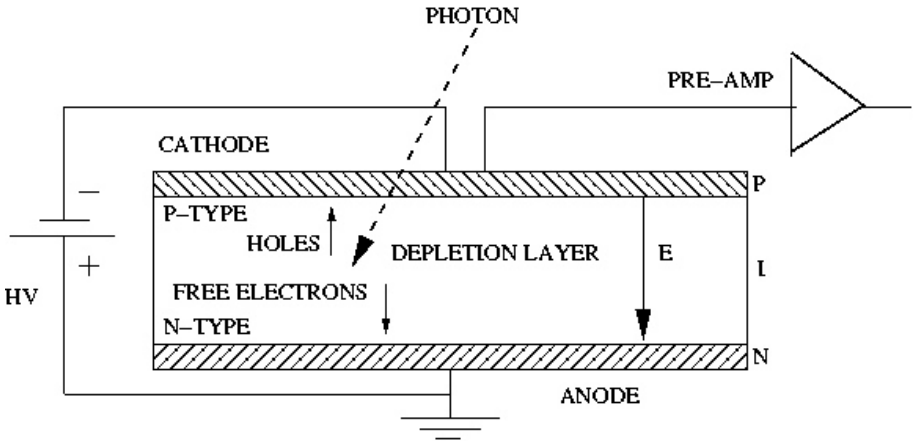

Figure 8: *The schematic drawing of a silicon PIN diode.*

2.2 Signal formation

The impinging X-ray photon ionizes the medium in the intrinsic depletion layer. This interaction generates free electrons and holes. The number of these free charge carriers depends on the energy of the impinging photon. The number of created electron-hole pairs is proportional to the photon energy. That is the reason for calling this kind of instruments energy dispersive spectrometers. The formation of free electron and hole pairs in silicon depends on the mean pair-creation energy w. In silicon the value of w is 3.63 eV at room temperature and atmospheric pressure (Alig et al. 1980). If the energy of impinging photon is E, the average number N of created electron-hole pairs can be simply calculated from $N = E/w$.
The spectral measurements are based on measuring the energy of photons, which can be transformed into the wavelength the of radiation. The reversed external bias electric field forces the free charge carriers to drift out of the depletion layer to the opposite sides of the chip, i.e. the electrons towards the anode and the holes towards the cathode. As the absorbed energy of the X-ray photon is proportional to the number of created free charge carriers, the photon energy can be derived from the induced charge. In the schematic drawing of Fig. 8, the positive holes at the cathode are collected for further signal processing.

2.3 Pre-amplifier and readout electronics

The signal charge Q created in the detector is the sum of positive holes created by the X-ray photon. The signal formation is described in time domain in Fig. 9, where t_c is the charge collection time. The detector-amplifier time constant is $t_{det} = R_i(C_{det} + C_i)$ (Spieler 2001), where R_i is the input resistance. The parameter C_{det} is the detector capacitance and C_i is the amplifier capacitance. If t_{det} is significantly longer than t_c, then the peak voltage V_s is

$$V_{\mathrm{s}} = \frac{Q_{\mathrm{tot}}}{(C_{\mathrm{det}} + C_{\mathrm{i}})}. \tag{1}$$

The voltage from the pre-amplifier is fed into the fast and slow channels. The fast channel acts as a high speed photon counter. The amplified signal voltage is converted into the corresponding photon energy in the slow channel. The measured voltage value is digitalized. The measured photon energy is stored in the respective energy channel, i.e. recorded as a count. The measured number of counts at different energy channels form the spectrum. This spectrum represents the final result from the readout electronics. In our detector systems, the number of energy channels is 512 in one spectrum, which covers the nominal energy range of 1-20 keV.

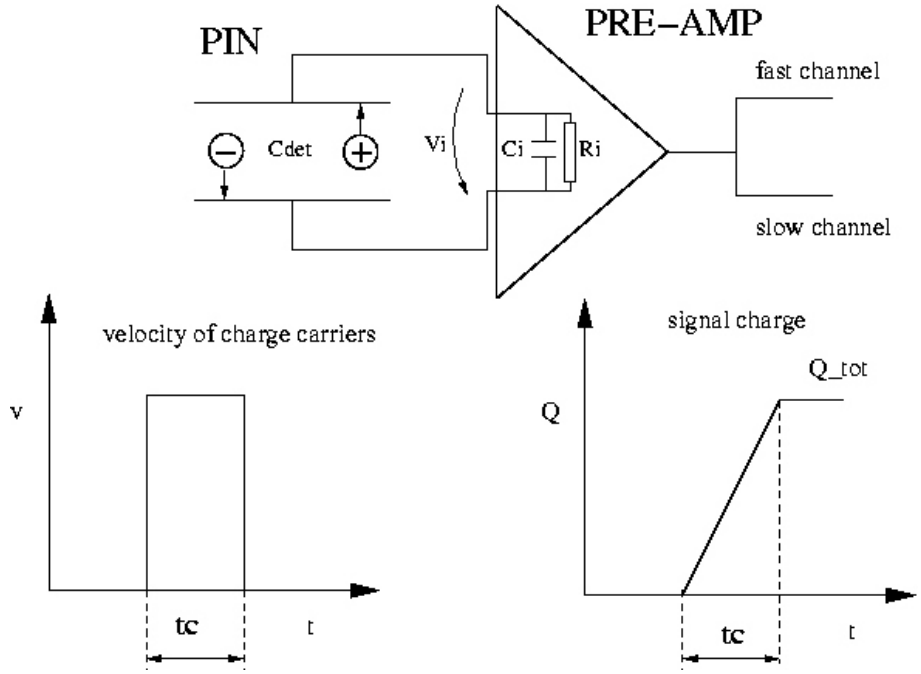

Figure 9: *Signal formation in a silicon PIN diode.*

2.4 Noise and energy resolution

There are several different sources of noise in a solid state X-ray spectrometer. This subsection gives only a brief introduction of the origin of the noise. The theory of electronic noise is a complex subject, and therefore only the main sources of noise in PIN detectors are considered here. Noise is always present in solid state X-ray spectrometers due to the statistics in the electron and hole pairs creation. The pair creation energy w of silicon can be characterized by a Poisson distribution. The number of electron and hole pairs created can fluctuate significantly for impinging photons of equal energies. This fluctuation obeys Poisson statistics and its variance σ is proportional to the square root of the number N of the created charge carrier pairs. This fluctuation is the first component of the noise affecting the performance of the PIN detector. The energy resolution is determined by the total noise of the detector. The more there is noise, the lower becomes the energy resolution. Hence noise must be minimized. The energy resolution of a spectrometer is

$$\Delta E = 2.35w\sqrt{\frac{FE}{w} + A + N_a}. \tag{2}$$

This energy resolution ΔE (Fraser 1989) or Full Width at Half Maximum ($FWHM$) denotes the width of the Gaussian line in the observed spectrum. The parameter F is called Fano factor, which is related to the energy deposition process during a photon interaction in a detection medium (Fano 1947). Part of the dissipation of a photon energy is transferred into excitation of lattice phonons. The value of F is about 0.15 for silicon at 3 keV. The detailed calculation of the value of F has been performed, e.g. in the paper of (Owens et al. 1996). The Fano factor reduces the intrinsic noise in the signal formation. The two other noise sources in Eq. 2 are the detector noise A and the amplifier noise N_{a} . The former, A, represents the detector dark current. This dark current originates from thermally generated electron-hole pairs. The fluctuation of the dark current is connected parallel to the signal current. Such a process gives rise to leakage current representing a white shot noise. The third component of noise, R, is generated in the amplifier. The magnitude of N_{a} depends on the operational temperature of the detector and amplifier system. All capacitance in the detector amplifier circuitry, like C_{det} and C_{i}, increase the value of N_{a} (Fraser 1989).

3 Scientific objectives of the X-ray instruments on the SMART-1 and CH-1 missions

The X-ray instrument system on the SMART-1 and CH-1 missions consisted of an X-ray camera for Moon observations and an X-ray monitor for solar observations. The scientific goal of the X-ray cameras was to generate a global elemental map of the Moon based on X-ray fluorescence measurements. The Moon fluorescence spectrometers (*D-CIXS* and *C1XS*) were both nadir pointing instruments measuring the X-ray glow of the lunar surface. They measured the X-ray fluorescence line emission principally from the crust elements, e.g. Mg, Al, Si, Ti, Ca and Fe, which was induced by the solar X-rays. The fluorescence analysis requires the knowledge of the simultaneous solar spectrum incident on the Moon surface. The task of the X-ray solar monitors (*XSM*) was to provide this information. In addition to serving the above purpose, the solar X-ray data was useful for coronal science.

3.1 D-CIXS and C1XS

Both Moon fluorescence spectrometers were built and designed by the instrument team at *RAL* (Grande 1999) and (Howe et al. 2009). The drawing in Fig. 10 illustrates the total FoV of the CH-1 C1XS. These fluorescence spectrometers were equipped with 24 swept charge devices (*SCD*). The operation of a SCD is analogous to a charge coupled device (*CCD*). The main difference between these devices is the method of transferring the charge. In CSD the charge is first swept into the central diagonal channels and then it is transferred to the pre-amplifier, as illustrated in Fig. 11 (Howe et al. 2009).

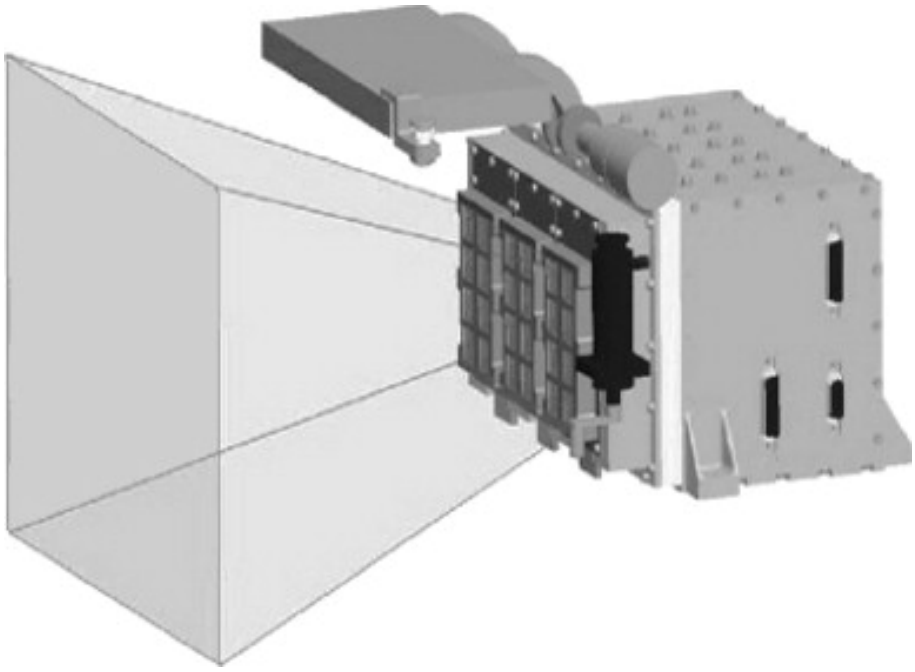

Figure 10: *Illustration of the Field of Views of the 24 SCD of the CH-1 C1XS Moon fluorescence spectrometer (RAL).*

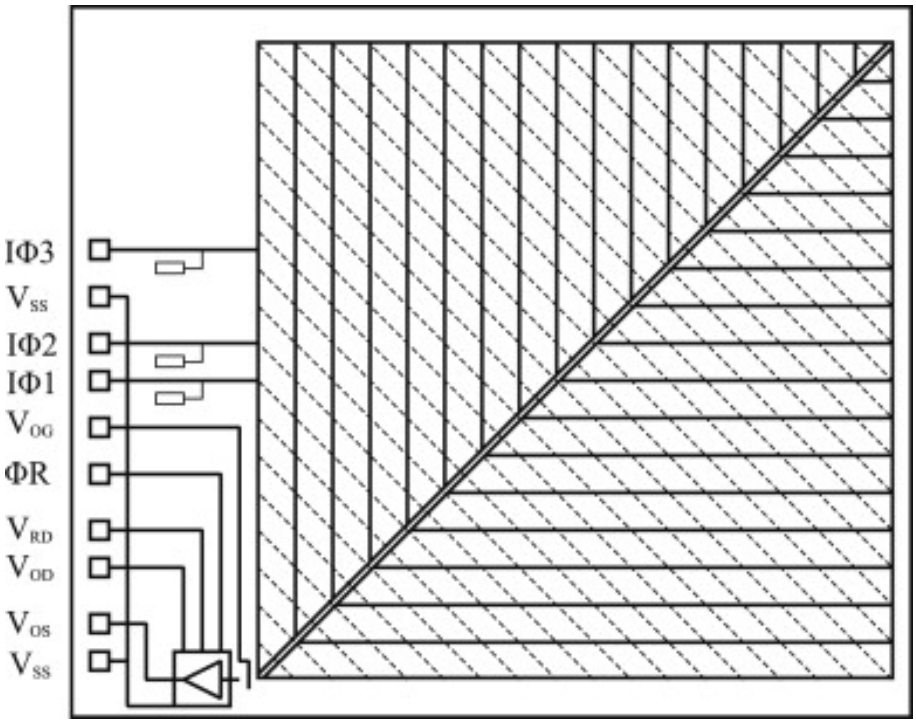

Figure 11: *A schematic of the internal structure of an SCD. The electrodes are depicted by the dashed lines, whilst the charge transport channels are indicated by solid lines. The charge is swept towards the central channels and down to the output amplifier (bottom left corner) by the action of the clock signals (Howe et al. 2009).*

Performance data	SMART-1	Chandrayaan-1
Energy resolution at 5.9 keV	230 eV	200 eV
Nominal energy range	1.88-20 keV	1.2-20 keV
Mass	4.6 kg	5.5 kg
Number of channels	512	512
Number of SDC	24	24
Spatial resolution at the altitude of 100 km	10 km	50 km
Maximum effective area (at 1.5 keV)	14 cm^2	14 cm^2

Table 3: *Key parameters of the SMART-1 and Chandrayaan-1 Moon fluorescence spectrometers.*

Detector data	SMART-1	Chandrayaan-1
Si PIN thickness	500 μm	500 μm
Si dead layer	0.1 μm	0.1 μm
Be-filter	25 μm	13 μm
PI-filter	0.25 μm	0.25 μm
Al-filter+contact	0.59 μm	0.60 μm
Au aperture stop diameter	1.5 mm	0.379 mm
Au thickness	125 μm	125 μm
On-axis A_{geom}	0.0177 cm^2	0.0011 cm^2
Nominal θ_c	52°	52°
Entrance aperture diameter	3.6 mm	4.7 mm
Detector-Aperture distance	2 mm	2 mm

Table 4: *Structural information of the SMART-1 and Chandrayaan-1 XSM detectors.*

Performance data	SMART-1	Chandrayaan-1
Energy resolution at 5.9 keV (BoL)	250 eV	200 eV
Energy range	1.88-20 keV	1.2-20 keV
Pile-up at 20 kcps	3 %	3 %
Number of channels	512	512
Nominal integration time	16 s	16 s

Table 5: *Performance features of the SMART-1 and Chandrayaan-1 XSM detectors.*

3.2 Performance of the solar monitors

Information of the properties and performance of the two different XSM detectors is given in Tables 4 and 5. The main differences between SMART-1 and CH-1 XSM are in the lower energy range limits and energy resolutions. The CH-1 XSM has a better QE at low energies, because the thickness of the Be-filter is about half of that in SMART-1 XSM. The energy resolution of CH-1 XSM is enhanced with a new low noise pre-amplifier FET. Due to the smaller active pixel area, the detector capacitance is also lower in CH-1 XSM. The XSM sensor unit is illustrated in Fig. 12.

3.3 Science goals of the solar monitors

The strength and spectral distribution of the fluorescence spectrum measured by the Moon spectrometers were strongly dependent on the solar X-ray irradiance at the surface of the Moon, and the primary task for the solar monitors was to provide solar X-ray spectra for the flux determination of the fluorescence lines. For the derivation of the expected fluorescence, the incident solar spectrum shape and intensity at energies higher than the absorption edges of relevant elements are necessary. Solar monitors observed the solar input at 1.8-20 keV, which does not include all important absorption edges connected to the spectra measured by the lunar spectrometers. This problem is solved by extrapolation of the low energy spectrum down to 1 keV by applying the model obtained with the spectral fits in the energy range of XSM. The validity of this extrapolation is restricted by the spectral model used in the fits. At present, bremsstrahlung has been applied to model the spectra, which excludes any line emission. Self consistent thin plasma spectral

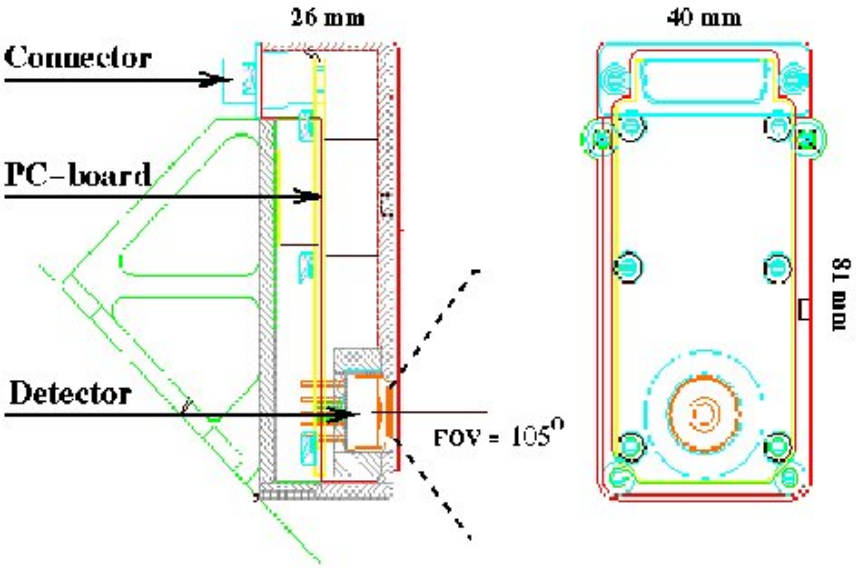

Figure 12: *Schematic illustration of the XSM sensor box. The mechanical assembly was similar for solar monitors on-board both SMART-1 and CH-1. The XSM main electronics boards were implemented into the electronic boxes of the Moon spectrometers.*

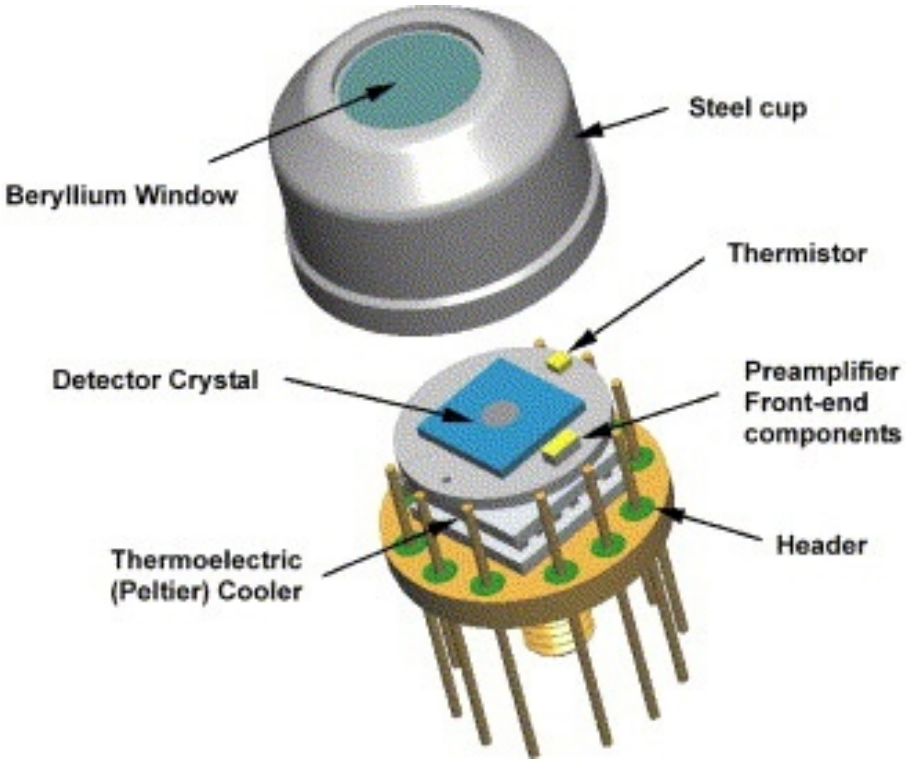

Figure 13: *An extended view of the SMART-1 XSM Si PIN-diode detector unit (OIA).*

models, e.g. Raymond-Smith (Raymond & Smith 1977) or Mekal (Mewe et al. 1985), would explain also the possible line emission component of the spectrum.
In addition to being a part of the Moon fluorescent spectrometer measuring system, the solar monitors provided significant additional information about the solar corona. The XSM spectral range is very sensitive to solar flare activity. During a flare the measured total spectra are largely dominated by the flux from the event, especially at higher energies above 3-4 keV. Following the temporal evolution of a large number of various flare events during the long observing period yielded a very useful database for studies of flare physics and flare evolution.
The time resolution of the spectra obtained with our solar monitors made it possible to follow the variability of the mean coronal temperature. Solar X-ray monitors traced the evolution of the X-ray spectrum of several C-level flares during the rise and decline phase. From the spectrum evolution it was possible to determine the temperature changes, emission measure and flux during the flare.
The motivation for independent coronal science is explained in paper I as follows. It is important to also note that our solar monitors provided a significant extension of spectral range to higher energies, and thus nicely complemented, e.g. the data of SOHO and TRACE.
Long term monitoring of the X-ray variability of the Sun can be compared to similar observations of other stars. The coronal emission is known to have a strong connection to the magnetic activity of stars, and following the behavior of the solar coronal emission together with other types of solar monitoring programs (magneto-grams, radio emission monitoring, XUV observations) will yield a more complete picture about the connections between different manifestations of the magnetic activity.

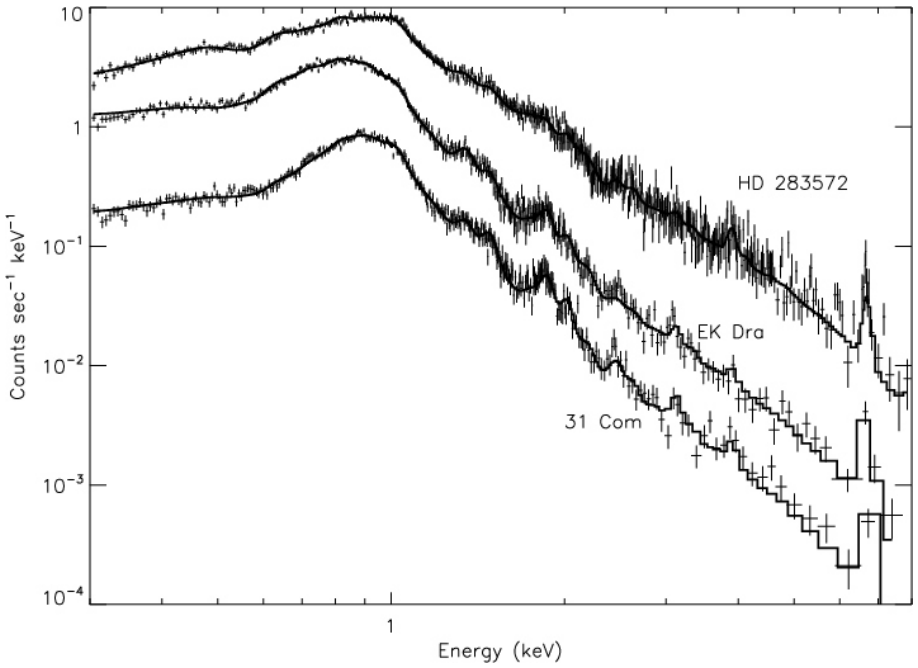

Figure 14: *Three different spectral fits between 0.3 and 8.0 keV for the data of the XMM Newton EPIC camera. The observed spectra ware obtained for HD 283572, EK Dra and 31 Com. (Scelsi at al. 2005). Respective solar coronal spectra were obtained with our solar monitors above 2 keV.*

Since the solar monitors observed the "Sun as a star", the interpretation of these data is similar to that obtained from distant point objects by large X-ray observatories. In ad-

dition, the spectral range of XSM overlaps partly with many of the modern astronomical X-ray satellites, e.g. XMM-Newton and Chandra. The spectral resolution is also similar. Therefore it is possible to make direct comparisons of the X-ray emission models of the Sun, which are based on the XSM observations, with the observations of other stars. Three different stellar X-ray spectra are shown in Fig. 14 obtained by XMM Newton (Scelsi et al. 2005).

4 Characterization of a non-imaging semiconductor X-ray solar monitor

In this section all the essential ground calibration routines are introduced, which were required to characterize the performance of the non-imaging semiconductor X-ray solar monitors. The numerical results introduced here, were all obtained from the CH-1 XSM ground calibrations. These X-ray solar monitors are composed of one silicon PIN diode, i.e. they are single pixel detectors and have a large circularly collimated FoV. Most of the calibrations were carried out at the X-ray laboratory of the Department of Physics of the University of Helsinki. Several of the tests required near vacuum conditions for measuring low energy X-ray photons below 5 keV. The attenuation of photons with energies of less than 5 keV is too dominant in free air. The test setups were built inside a vacuum chamber containing a X-ray tube with a titanium anode. The minimum chamber pressure achieved was 4 mbar. This vacuum chamber was utilized in the energy scale and energy resolution calibrations. The FoV map and cross calibrations were also made in this vacuum chamber. These calibrations were done on the FM sensor box, which included the detector PIN, pre-amplifier and Peltier cooler. The data were read into the laboratory MCA, which consisted of 2048 channels. The pile-up and low energy threshold measurements were carried out at the manufacturer's (*OIA*) facilities with the flight electronic box. All X-ray lines and the related line energies applied in these calibrations are compiled in Table 6. The final ground calibration data analysis was made with the IDL (*Interactive Data Language*) software.

Fluorescence line	Line energy, keV
Al Kα	1.487
Pb Mα	2.345
Ca Kα	3.692
Ti Kα	4.511
Mn Kα	5.898
Mn Kβ	6.490
Cu Kα	8.047
Cu Kβ	8.905
Pb Lα	10.50
Pb Lβ	12.62
Rb Kα	13.395
Rb Kβ	14.961

Table 6: *Fluorescence lines used in the calibrations.*

4.1 Determination of the energy scale vs. channel relation

The purpose of this test was to check the linearity of the energy scale of the detector at different PIN temperatures at a constant room temperature, i.e. the sensor box temperature was about +20°C inside the vacuum chamber. The test setup was simple. The X-ray tube with a Ti-anode was the primary source. To cover the detector energy range of interest (1.5 keV-20 keV), a multi element fluorescence sources were used. We fabricated two different fluorescence sources. The first one was a pure Pb-plate. The second one was a button-.like pressed powder mixture composed of Al, Ca and Cu. All fluorescence

line energies of these two samples are given in Table 6. The primary beam from an X-ray tube was collimated against the fluorescence sample. Hence we made two separate tests one with the AlCaCu-sample and the other with the Pb-sample. The calibrated detector was set to measure the fluorescence emission induced by the primary beam. Both tests were repeated at several operational PIN temperatures, i.e. -20°C, -15°C, -10°C, -5°C and 0°C with a constant ambient temperature of +20°. As a result of these tests, we got two fluorescence spectra both containing three fluorescence lines and the scattered Ti Kα that originated from the X-ray tube. Each of the lines listed in table 6 was analyzed with the IDL S/W using Gauss-fit routine to determine the respective channel numbers for the line centroid. After the line centroids were derived, the channel versus energy scale relations were calculated with the IDL line-fit routine. The results of this routine were gain and offset, which determined the energy scale of the PIN detector. The numerical results of these calibrations are compiled in Table 7 and Table 8. It is clearly seen from the results, that the line centroids had a tendency to shift towards lower channels, at least when the PIN temperature was less than -5°. Despite of this "creeping" of the line centroids, the derived gains stayed almost steady about 0.0205 keV/channel. The offset values also increased with the decreasing PIN temperature. The outcome of this test was, that the PIN temperature must be keep as steady as possible during the observations. The shift of the detector energy scale due to the PIN temperature variations caused additional inaccuracies in the final data analysis. There was an even more crucial factor affecting the energy scale, as explained later, i.e. the sensor box temperature. Before the calibration of the CH-1 XSM FM, we first checked the linearity of the laboratory MCA with an ^{55}Fe-, copper- and rubidium sources to investigate a wide energy range. The linearity test results are shown in Fig. 15 and Fig. 16.

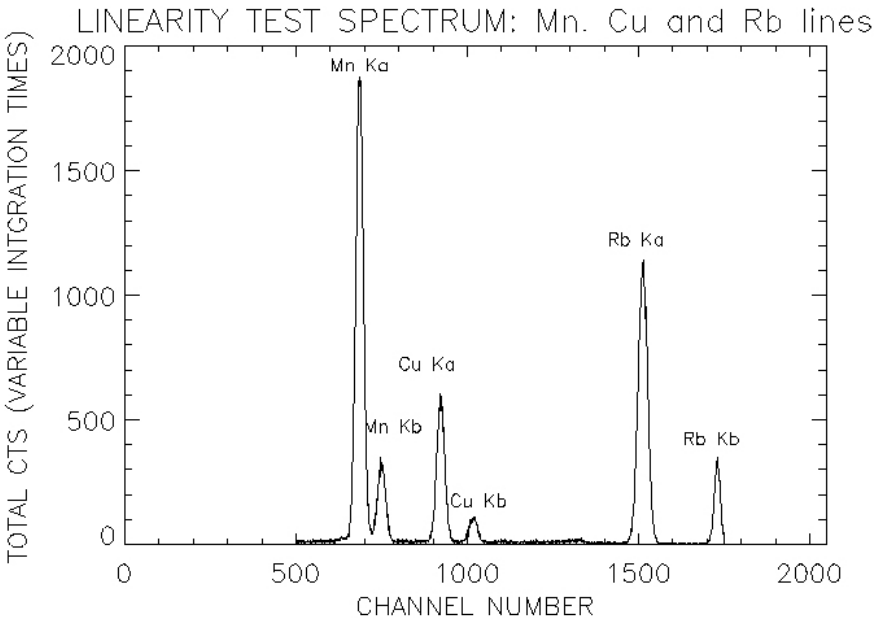

Figure 15: *The MCA linearity test spectrum was composed of six distinct lines. Those were Mn Kα (5.90 keV/ch#686.1), Mn Kβ (6.49 keV/ch#750.3), Cu Kα (8.05 keV/ch #922.3), Cu Kβ (8.91/ch#1017.0), Rb Kα (13.39 keV/ch#1512.8), Rb Kβ (14.96 keV/ch#1730.1).*

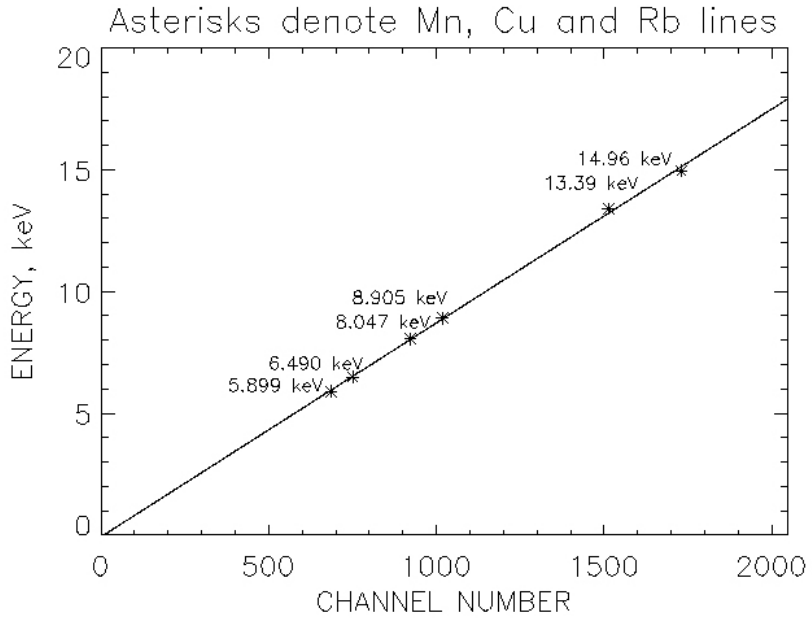

Figure 16: *The gain of the laboratory MCA was linear as can be seen in the plot above. The asterisks denote the line centroid positions, which were derived by IDL Gauss-fit routine from the test sample spectrum. The solid line joining the data points was derived with the IDL line-fit routine.*

PIN temperature	Al Kα	Ca Kα	Ti Kα	Cu Kα	gain	offset
+0°C	73.36	180.92	220.22	392.53	0.0206	-0.023
-5°C	72.61	179.80	219.30	392.53	0.0206	-0.012
-10°C	72.68	180.69	220.47	393.26	0.0205	-0.003
-15°C	72.10	179.92	219.39	392.20	0.0205	+0.008
-20°C	71.62	179.04	218.47	390.16	0.0206	+0.008
Mean value	72.47	180.08	219.57	391.80	0.0206	-0.004
Standard deviation	0.658	0.752	0.798	1.263	3.0E-09	-0.256

Table 7: *The channel numbers of the fluorescence line centroids of the AlCaCu-sample at five different PIN temperatures and the derived gains (keV/ch) and offsets (keV). The mean values and standard deviations were calculated also for all measured values.*

PIN temperature	Pb Mα	Ti Kα	Pb Lα	Pb Kβ	gain	offset
+0°C	117.64	221.05	514.53	615.30	0.0206	-0.062
-5°C	117.42	221.55	516.28	617.16	0.0205	-0.051
-10°C	116.97	221.08	515.98	616.89	0.0205	-0.040
-15°C	116.15	220.09	514.41	615.39	0.0205	-0.026
-20°C	115.52	218.79	511.87	612.02	0.0206	-0.025
Mean value	116.74	220.51	514.61	615.35	0.0205	-0.041
Standard deviation	0.793	1.212	3.064	4.177	3.0E-09	0.0003

Table 8: *The channel numbers of the fluorescence line centroids of the Pb-sample, otherwise as in Table 7.*

4.2 Determination of the energy resolution as a function of photon energy

The energy resolution determination utilized the same data, which were obtained in the calibration test described in the previous subsection. The detector gain must be also known to determine the energy resolution (Tikkanen 1994). It is

$$\Delta E = \sqrt{2ln2}\sigma g \approx 2.35\sigma g, \tag{3}$$

where σ is the standard deviation of the fitted line energy and g represents the detector gain (keV/channel). This test revealed the BoL (Beginning of Life) energy resolution, which is an important performance parameter for a spectrometer. Resolutions, line centroids, gains and offsets of each fluorescence line were calculated by using the Gaussian fitting routine of the IDL S/W. The final relation between a photon energy and energy resolution is

$$\Delta E = \sqrt{aE + b}, \tag{4}$$

where the parameters a and b are empirical parameters connected to the detector electronic noise. The energy resolution was determined at five different PIN temperatures, i.e. -20°C, -15°C, -10°C, -5°C and 0°C with a constant ambient temperature of +20°. The superimposed plot of these two fluorescence spectra used in this test is shown in Fig.17. The resolution curves and related parameters a and b were determined with a linear fitting routine of IDL by squaring both sides of the Eq. 4 ($\Delta E^2 \propto aE + b$). The energy resolution fitting results are given in Table 9. The final resolution curves at five different PIN temperatures between 0-10 keV are plotted in Fig. 18. The higher PIN temperature gave a lower energy resolution. The reason for that was the higher leakage current level at higher PIN temperatures.

PIN temperature	a (keV)	b (keV^2)	FWHM (eV) @ 5.9 keV
+0°C	0.0031	0.0306	221
-5°C	0.0028	0.0287	212
-10°C	0.0020	0.0260	195
-15°C	0.0019	0.0260	193
-20°C	0.0025	0.0200	186

Table 9: *The results for the energy resolution at 5.9 keV of the CH-1 XSM .*

4.3 Determination of the FoV sensitivity map

The sensitivity of the detectors depended on the position of the Sun in the circular FoV. The off-axis angle θ is the angular distance between the optical axis and the position of the Sun in the FoV. The roll angle ρ represents the azimuthal position angle measured from a fixed direction in the FoV. The FoV sensitivity map must be determined as a function of these two angles. The maximum geometric area of the detector is determined by the hole area of the golden aperture stop right above the PIN. The schematic drawing in Fig. 19 illustrates the dimensions of the detector package. The maximum angular size (θ_c) of the FoV depends on the aperture diameters (d and D) and of the distance between detector and entrance aperture (H). The limiting off-axis angle is

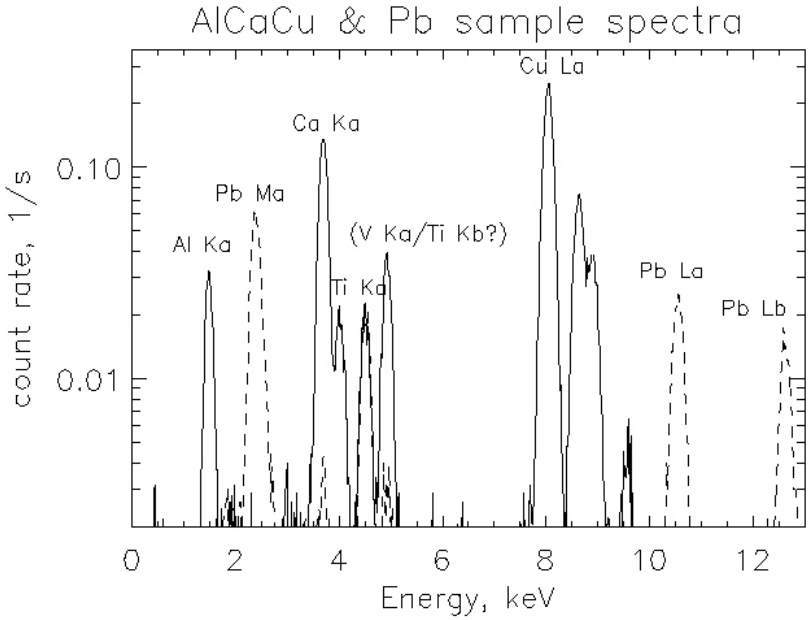

Figure 17: *A superimposed plot of the fluorescence spectra of the AlCaCu and Pb samples used in energy resolution and energy scale calibrations. These two spectra were obtained at the PIN temperature of -15° C. The Pb-sample spectrum plot is denoted with the dashed line. All the lines applied in this calibration are marked in the plot. The Ti Kβ (4.932 keV) line given in parenthesis was probably superimposed with the V Kα (4.952 keV) from the sample container. This particular Ti Kβ was therefore not used.*

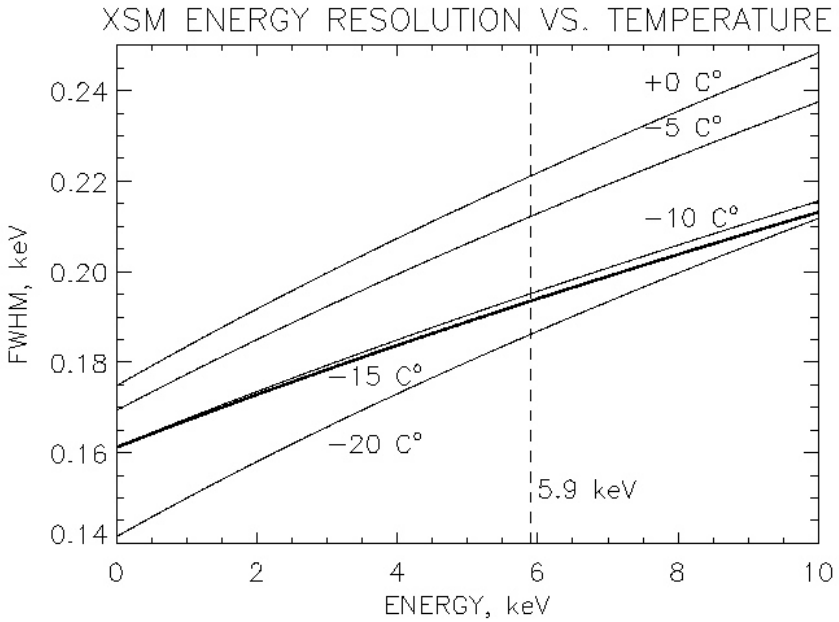

Figure 18: *CH-1 XSM energy resolution curves at five different PIN temperatures. The bold curve represents the PIN temperature of -15° C.*

$$\theta_c = \arctan(\frac{D+d}{2H}). \quad (5)$$

The parameter x in Fig. 19 denotes the distance between the stopper and detector surface, which was about 0.1 mm. If the assembly of the detector PIN in the steel enclosure were ideal with respect to these dimensions (i.e. d, D and H), the FoV sensitivity map calibrations would be unnecessary. The sensitivity map could then be derived mathematically (Lehtolainen 2009). The aperture stop was glued manually on the top of the PIN. This procedure required the aid of a microscope. The fixing was never perfect with respect to the concentric matching of the aperture entrance and aperture stop. The real sensitivity map of the SMART-1 XSM is shown in Fig. 33 of Section 6.1. It exhibits a clear asymmetry. This FoV sensitivity map was generated by scanning the FoV with X-ray tube beam. The X-ray tube beam size was 10 mm x 10 mm and there were four kapton (polyimide) foil filters in front of the entrance aperture of the detector for reducing the count rate. The PIN temperature was set -15°C. The X-ray tube current was 0.005 mA and the respective voltage was 10 kV. The test detector was rotated with respect to the θ angle at 1° step intervals and illuminated for a constant integration time at each step. The total count rates between 7 and 9 keV were used to determine the final FoV sensitivity map. This test was carried out at several different roll angles ρ. This test revealed the shadowing effect, i.e. the obscuration factor OB. The entrance aperture edge of the collimator cast a shadow onto the detector. The size of the active detector area, which fell under this shadow, depended on the angles θ and ρ. The generation of the obscuration factor array was determined from the normalized total counts measured for each respective θ and ρ pair of angles. In practice, OB was proportional to the detector area outside the shadow of the collimating entrance aperture. The tests gave the final values of OB for every FoV angle pair θ and ρ.

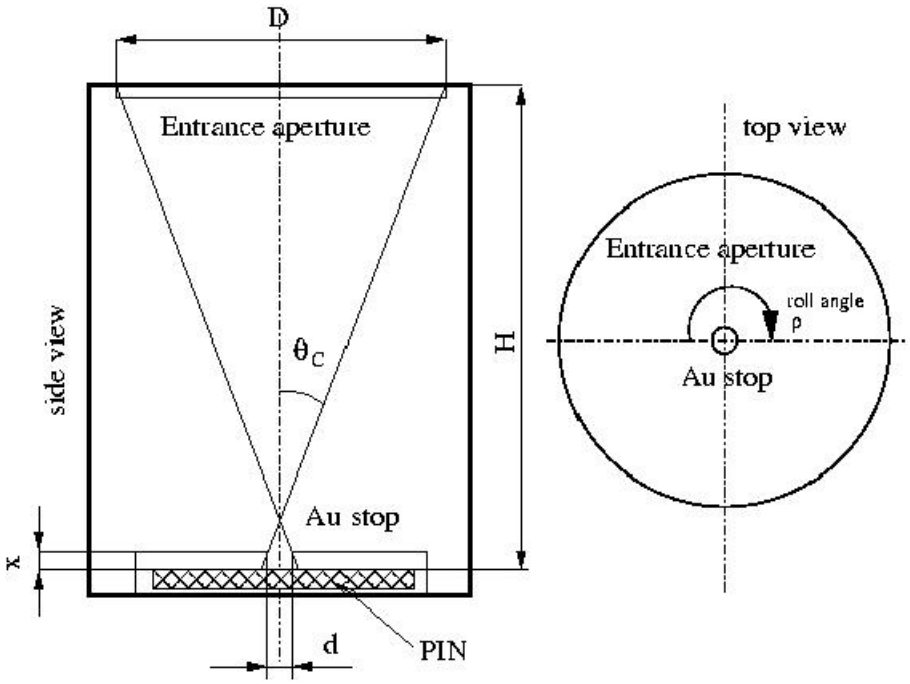

Figure 19: *Schematic dimensional drawing of the detector geometry.*

One FoV map scanning test of the SMART-1 XSM FM is shown in Fig. 20. The specimen was attached to the goniometer, which enabled the rotations of the detector in front of

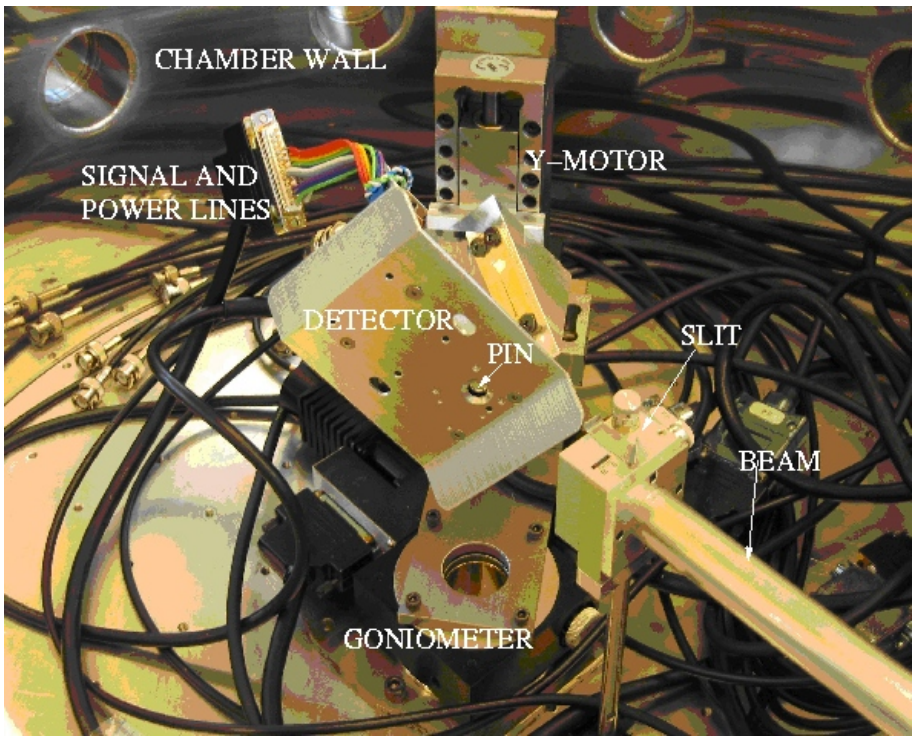

Figure 20: *SMART-1 XSM FM in the vacuum chamber during the FoV map test.*

the X-ray tube beam.

4.4 Cross calibration

The cross calibration aimed at comparing the sensitivity of the specimen detector to another detector with a well known performance. This cross calibration compared the physical fluxes measured by the two detectors under identical test conditions. This would require, that the distance measured from the X-ray emitting source (X_1) and the related distance between the fluorescence source and the detectors (X_2) must have been the same for both setups. The measured fluorescence emission intensity is inversely proportional to the distance square X_2 (see Fig. 21). The distance X_1 between the fluorescence sample and the X-ray tube must also be identical in this comparison test. The X-ray tube power has been adjusted so that the control voltage and current were exactly the same. The phase angle ϕ and the ambient pressure should also be equal for both specimens during this test. The integration time may have been different for both detectors, but this is taken into account in the final comparison analysis. The line fluxes measured in these tests must be scaled according to the integration times. The lead plate suited well for being a fluorescence sample in these tests. The fluorescence emission lines of the Pb-sample covered a sufficient energy range. The applicable line energies were Pb Mα at 2.345 keV, Pb Lα at 10,5 keV and Pb Lβ at 12.62 keV. The scattered X-ray tube anode element line can also be utilized in these tests, e.g. Ti Kα line at 4.5 keV. The measured fluorescence spectra were first analyzed with spectral fitting S/W. Then the measured line intensities were compared. The differences of the derived line flux ratios between the SMART-1 FS XSM and CH-1 FM XSM were less than 5%. One typical cross calibration test setup configuration is shown in Fig. 21.

Before the cross calibration can be done, the on-axis effective area A_{eff} of the test detector

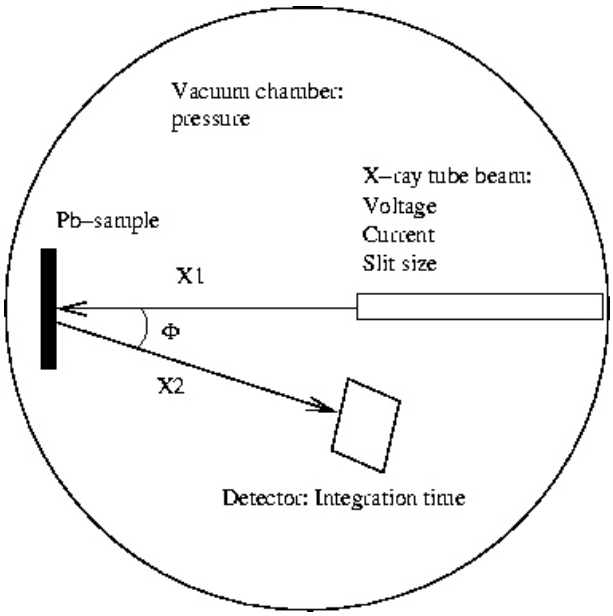

Figure 21: *The schematic illustration of the comparison calibration test setup in the vacuum chamber. The reference detector, i.e. SMART-1 flight spare XSM was placed first in the test chamber to measure the fluorescence from the Pb-sample. The test specimen, i.e. CH-1 FM XSM was performed the same measurement in identical conditions. The absolute Pb-line intensities were derived with spectral fitting S/W and these intensities obtained from the SMART-1 FS XSM and CH-1 FM XSM were compared.*

must be determined as accurately as possible. The value of $A_{\rm eff}$ depends on detector geometric area $A_{\rm geom}$ and quantum efficiency *QE*.

4.4.1 Determination of the detector geometric area

The value of $A_{\rm geom}$ was equal to the area of the hole of the aperture stop, but the measurement of this area was not a simple task. The nominal diameter of the aperture stop was 1.5 mm in SMART-1 XSM and only 0.35 mm in CH-1 XSM. Depending on the drilling process of this hole, the shape of the edge of the hole usually deviates more or less from an ideal circle. The value of $A_{\rm geom}$ is one of the most important factors in the characterization of a single pixel wide FoV detector. The error in the physical flux calculated in the final spectral analysis is directly proportional to the error of $A_{\rm geom}$. For example, the designed stopper diameter of the CH-1 XSM was 0.35 mm. This hole was made manually with a drill bit of 0.35 mm. The photograph of this aperture stop is shown in Fig. 22. The edge of the hole is quite rough. Therefore the area of this aperture stop hole had to be determined from an image analysis based on photographs taken by the manufacturer. The same Au-stop is also shown in Fig. 23.

4.4.2 Determination of the QE-curve

The quantum efficiency *QE* depends on the filter and detector materials and their respective thicknesses. The general formula (Fraser 1989) is

$$QE = [1 - exp(\mu_{\rm det} x_{\rm det})] \prod_{i=0}^{n} exp(\mu_{\rm i} x_{\rm i}), \qquad (6)$$

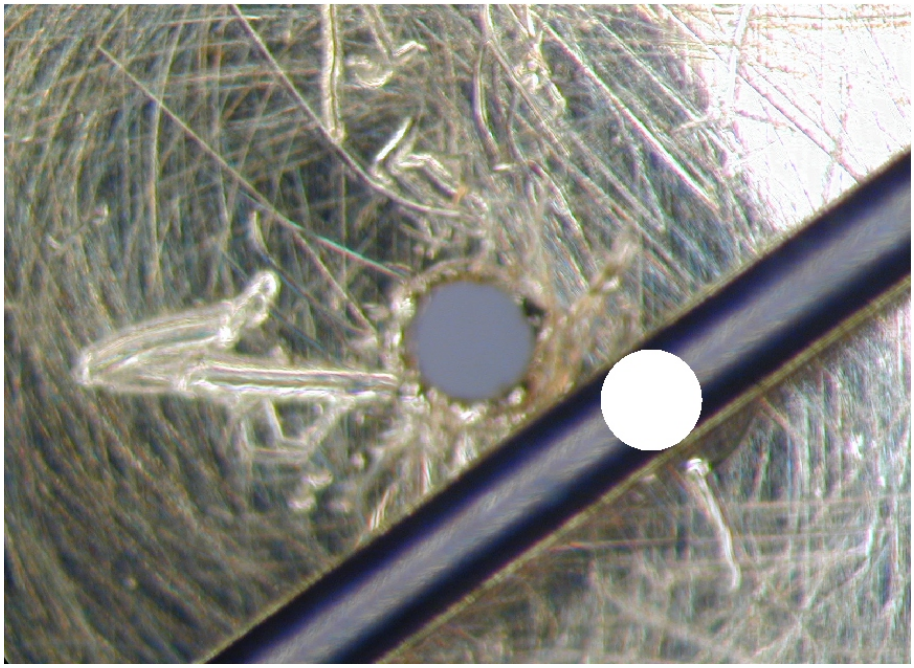

Figure 22: *CH-1 XSM aperture stop with a scale drill bit of 0.35 mm. The white circle was drawn on the drill bit, which enabled scaling the photographic pixel size.*

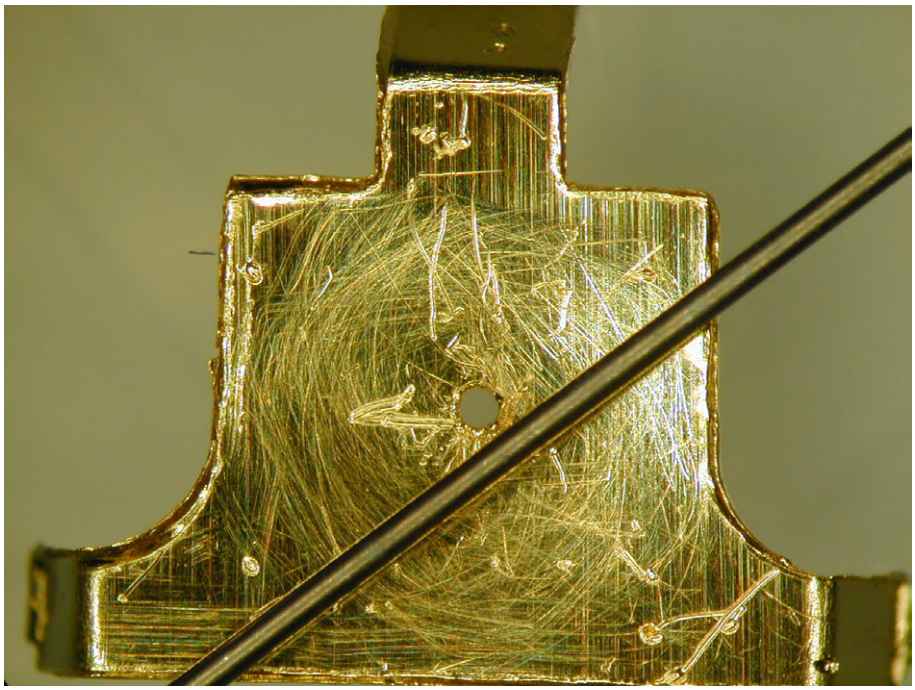

Figure 23: *A less magnified photo of the same golden aperture stop structure shown in Fig 22.*

where $\mu_{\rm det}$ is the mass attenuation coefficient of the detector and $x_{\rm det}$ is the thickness of the detector. The parameters $\mu_{\rm i}$ and $x_{\rm i}$ are the respective coefficients for filters. It is a straightforward task to calculate the on-axis QE, if the filter and detector dimensions are known. This on-axis effective area is

$$A_{\rm eff}(0^\circ) = A_{\rm geom}(0^\circ) QE(0^\circ). \tag{7}$$

4.5 Low energy limit test

The low energy limit is a detector specific feature, which was fixed in our detector readout systems. The lowest recorded photon energy could be adjusted with a changeable on-board S/W parameter. The purpose of this low energy limit was to reduce low energy noise. Furthermore, it also inhibited the generation of spurious or phantom counts in the detector read-out electronics. The generation of these phantom counts was related to the loss free counting system (Westphal 1979), which is introduced in the next subsection. The low energy limit could be empirically determined by operating the detector with different parameter values. The lower this limit was the lower the possible recorded photon energy. One strong ^{55}Fe-source was sufficient for carrying out this test. The detector was illuminated at a constant low count rate with different parameter values. Each of the obtained spectra corresponded to a different parameter value (S/W parameter p $\in$ [0,50]). The obtained spectra were analyzed with respect to the number of total counts and the number of counts composing the low energy noise. It was found that the low energy noise generated phantom counts in the recorded spectrum. The lowest applicable parameter value could be determined by finding the number of total counts as a function of the parameter value. The lowest limiting parameter value corresponded to the spectrum, in which the number of total counts stabilized, i.e. the count rate became constant above this limiting parameter value. The low energy limit could also been found from a measured spectrum. One had to determine the lowest energy channel, which corresponded to the onset of the low energy tail of the Mn Kα line. The parameter values used in this test should have covered the energy range of interest, i.e. between 1 keV and 2 keV. This procedure was then repeated at a moderate and at a high count rate.
Our plot in Fig. 24 illustrates a single test spectrum obtained with an ^{55}Fe-source for the S/W parameter 21 during a low energy limit test of CH-1 XSM. There was no low energy noise below channel number 34 except in the first channel, which was ignored since it was found that it did not contribute to the phantom counts. This limiting channel number 34 here defined the starting point of the low energy tail of the spectrum. The channel versus energy relation is shown in Fig. 25. It was solved with the aid of the Si escape peak and Mn-lines. The lowest readable photon energy corresponded to about 1.2 keV at the S/W parameter 21 used in the test example.

4.6 Pile-up test

The pile-up phenomenon is connected to the count rate level. The higher the measured count rate, the more pile-up counts are recorded in the spectrum. Pile-up photons are recorded in the spectrum when the detector measures an energy of two or more photons at the same time, instead of measuring the energy of each photon separately. Dead time, on the other hand, is a time interval when a detector is insensitive to incoming signal. For X-ray spectrometers, this interval is the time required to measure the energy of a photon. If this measurement process is still unfinished, the successive photons are ignored.

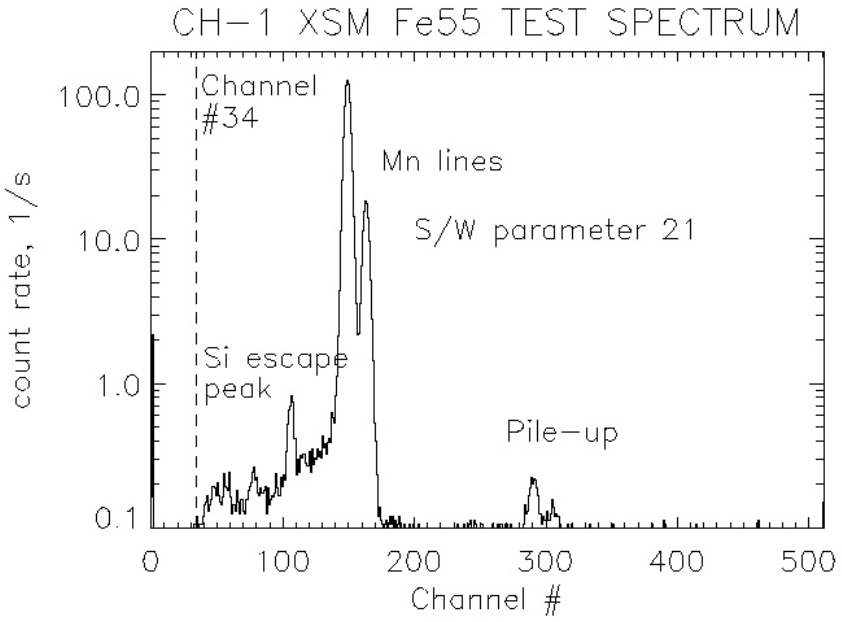

Figure 24: *Low energy limit test spectrum obtained with the S/W parameter 21.*

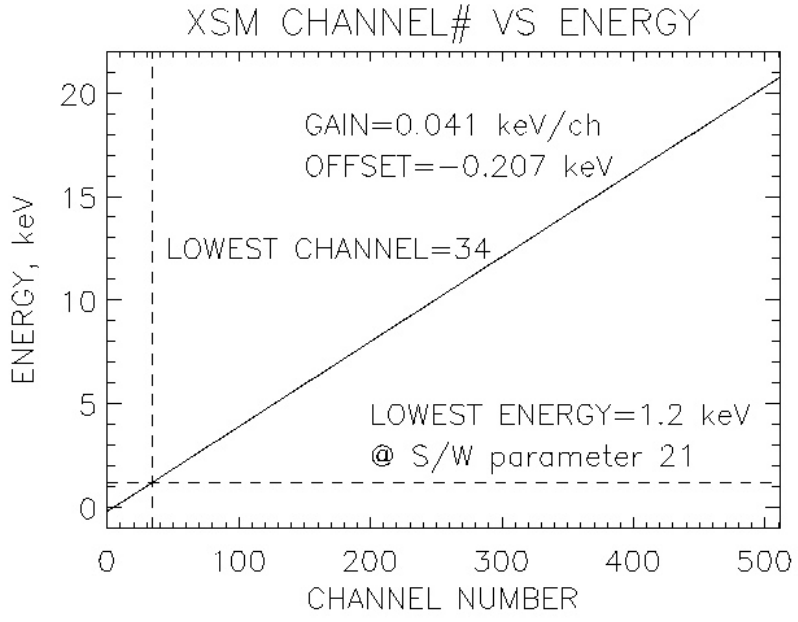

Figure 25: *The results for the single test spectrum of Fig. 24.*

A traditional pile-up rejection is based on the idea of blocking an energy measurement channel as soon as this channel has recorded a photon. The typical time delay between the moment of detecting a photon and blocking that channel is of the order of a few microseconds. If the time interval of two consecutive photons entering the detector is shorter than this time, the second photon is able to slip into the energy measurement together with the previous photon. Hence the measured photon energy will be erroneous and can be as high as the arithmetic sum of the energies of the two (or more) consecutive photons. The pile-up rejection performance depends on the speed of the measurement system versus recorded count rate level. Within our detectors, the dead time correction utilized the so called loss free counting system, where there were two channels recording entering photons. The first channel was the fast channel and the other one was the slow channel. The slow channel performed the energy measurement. The fast channel counted incoming photons with a time resolution of less than 1.5 μs. The slow channel was blocked with a specific time delay, while a photon was under energy measurement. The processing time of the slow channel depended on the energy of the measured photon. The higher the energy, the longer was the measurement time, i.e. the dead time. All photons entering the detector during this dead time were lost. The loss free counting system reduced this dead time. While the slow channel was blocked, the fast channel was counting the incoming photons. All these photons were recorded into the final spectrum. Each of these fast channel photons were given the same energy, which was measured for the previous photon in the slow channel. This type of artificial adding of the fast channel counts in the spectrum, with no energy measurement, did not statistically deteriorate the shape of the observed spectrum. This loss free counting also suffered from the pile-up effect, like all conventional detectors equipped with a traditional pile-up rejection, but this loss free counting system reduced the dead time significantly.
The detector pile-up could be easily determined with an ^{55}Fe-source in free air conditions. The detector was illuminated by the ^{55}Fe emitter located at different distances from the detector. The longer distance between the source and detector gave a weaker count rate. The total counts versus pile-up counts could be then determined from these spectra taken at different count rate levels. The results from the CH-1 XSM FM calibrations indicated a pile-up of about 3 % at 2×10^4 counts/s. We were also able to derive the dead time or the pulse per resolution time for the CH-1 XSM. Actually, the fast channel operation was better (1.57 μs) than that specified by the manufacturer (2.0 μs). A spectrum showing a low level pile-up is shown in Fig. 24.

4.7 Thermal effects on the detector gain and offset

The aim of this test was to be supplemental for the test described earlier in subsection 4.1, where the detector PIN temperature versus gain was investigated. The temperature of the applied vacuum chamber could not controlled. The temperature was always approximately the same as the ambient temperature of the laboratory room, i.e. about +20°C. Hence this test had to be carried out elsewhere. We decided to use a thermally controlled oven at RAL. An ^{55}Fe emitter would have been a sufficient source for this test procedure. Unfortunately, we were never able to perform a successful temperature test on the CH-1 XSM FM. This detector was sent to RAL for testing with the flight electronics about one month before its final delivery to India. These tests failed due to the malfunctions related to the operation of XSM FM with the flight electronics. XSM was sent back to OIA with flight electronics for investigation. The failure was found and it was related to the 20 kHz interference in the signal line, which spoiled the energy resolution. It was caused by a new

type of DC-converter. This interference signal was filtered out with an extra capacitor and after that the detector operation became normal again. There was unfortunately no further testing at that time due to the delivery schedule.
This test would have been carried out very simply. The planned test procedure was as follows. The detector is illuminated at a constant count rate at different temperatures. These integrations will cover the expected operational temperature range between -40°C and +40°C. The detector PIN temperature will be the same as the operational temperature during these tests. The shifting of the Mn Kα and Mn Kβ line centroids at different sensor box temperatures will be measured. Hence the changes in gain and offset of the energy scale as a function of the sensor box temperature can be determined. If this shift is accurately known, this information can be applied during in-flight calibration. This information is valuable when the sensor box temperature changes significantly during a long integration. The gain and offset varies also as a function of the PIN temperature, but this is not so problematic, because the PIN temperature can be controlled very accurately during an observation. The problem is related only to the control of sensor box temperature. The reason for the gain shifting is the shaper transistor in the pre-amplifier. To avoid the gain shift, the sensor box would need an extra Peltier for controlling the temperature of this part of the electronics.
We have made a preliminary analysis of the gain versus sensor box temperature relation. The calibration data used in this analysis were obtained from one long calibration run and separate observations done by CH-1 XSM on the Moon orbit. The PIN temperature was about -9°C during the early phase of the mission and it was lowered later on down to -18°C. The plots illustrates the analysis results done at -9°C. These data suffer from the low statistics. The curves representing the fits are second degree polynomials (Alha et al. 2009).

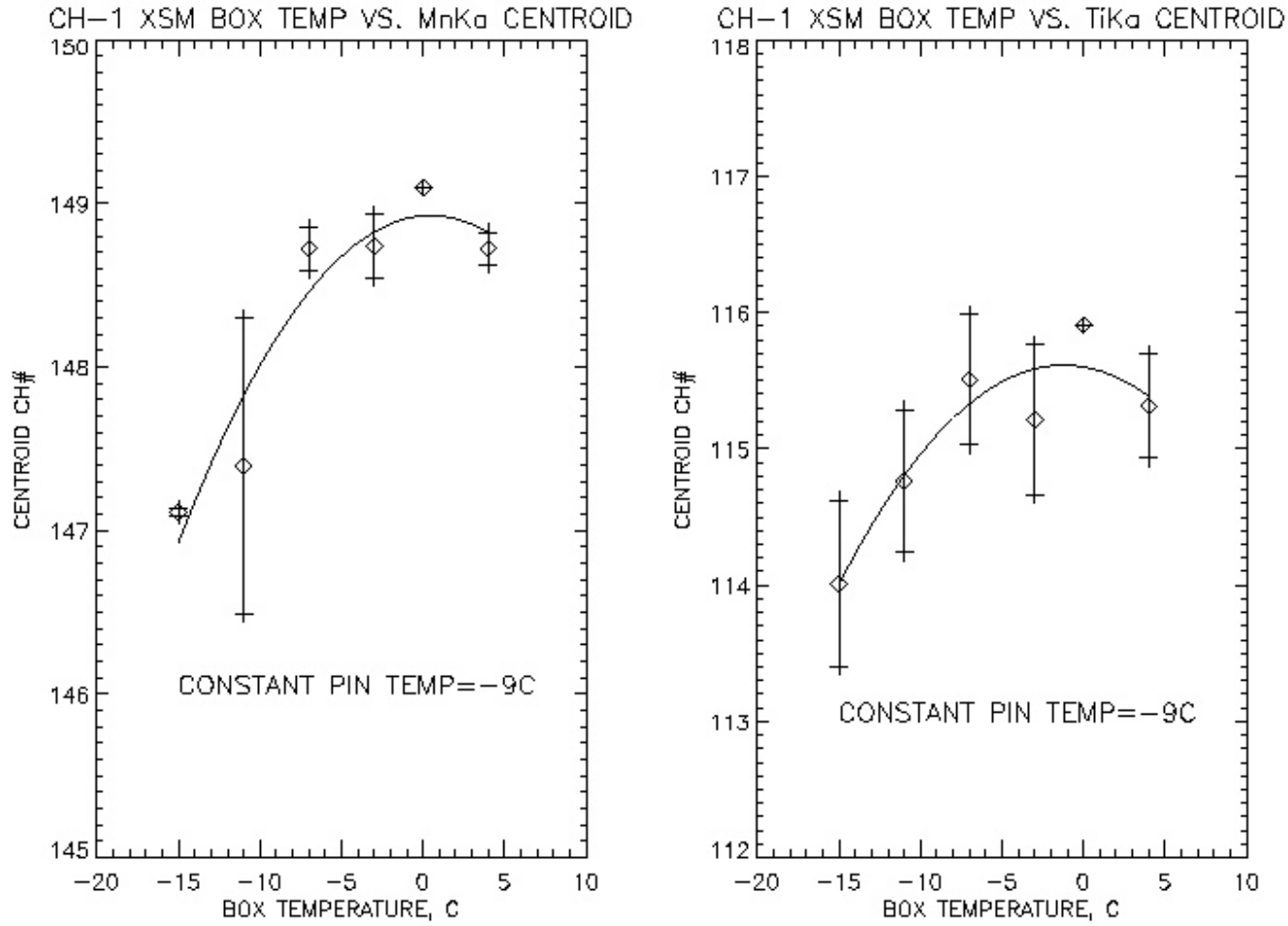

Figure 26: *These plots illustrate the relation between the sensor box temperature and the shifting of the Mn Kα and Ti Kα lines at a constant PIN temperature of -9°. The shifting of the line centroids is fitted with the second degree polynomial. This in-flight calibration data were obtained during the the Moon orbit. We didn't obtain enough calibration data at different box temperatures for performing a more confident statistical analysis. This analysis is still going on and we have to collect separate calibration data piecewise from different observations to determine the statistics.*

5 In-flight operations

The utilization of the solar monitor data for the SMART-1 and CH-1 Moon spectrometers are discussed in this section. The operational strategy of solar monitors is also introduced. Considerations of the quality and volume of the data from these two missions are also presented.

5.1 SMART-1 and Chandrayaan-1 mission time lines

The ESA's SMART-1 mission was launched on 27 September 2003 on Ariane 5 to the geostationary transfer orbit. The cruise phase to the Moon capture took 14 months using solar electric propulsion (Racca et al. 1998). The extended lunar science phase terminated with a controlled Moon crash on 30 August 2006. Our solar monitor on-board SMART-1 produced nearly 439 hours of solar spectral data. During the off-solar observations, i.e. when the Sun was outside of the FoV, XSM observed the X-ray sky background. We have made a preliminary X-ray sky background analysis based on these off-solar integrations with typical length of several hours. During SMART-1 mission, XSM observed during on-solar observations mainly C-level flares, but also two M flares and a number of lower level flares. A detailed analysis of the flare data is still in progress, the main reason being the lack of funding to allocate resources for the work. Some preliminary results are introduced in section 6. The solar activity during SMART-1 mission is shown in Fig. 27. This GOES data, of 5 min integrations, clearly illustrates the strong variability of solar activity.
Chandrayaan-1 was the first Indian lunar mission, which was launched on 22 October 2008. This mission was terminated due to the accidental loss of radio contact on 28 August 2009. Our solar monitor on-board the CH-1 was almost identical with the SMART-1 XSM. The main differences were in spectral resolution, Be filter and aperture size (Tables 4 and 5 of section 3.2). The very weak solar activity during CH-1 mission is shown in Fig. 28. XSM on-board the CH-1 caught only a few C-level flares. These solar data showed very low count rates. The total solar integration time of XSM was approximately 32 hours during the CH-1 mission.

5.2 Operation of solar monitors

The in-fight operation of these non-imaging semiconductor wide FoV X-ray solar monitors is simple. These detectors have three operational modes, calibration mode, observing mode and annealing mode. Only the position of the shutter is different in the calibration and observing modes. The shutter is open during the observing mode and closed during calibration mode. An ^{55}Fe source is attached on the inner surface of the shutter. This source is covered with a Ti-foil having a thickness of 5μm. The calibration spectrum includes four emission lines: Ti Kα (4.5 keV), Ti Kβ (4.9 keV), Mn Kα (5.9 keV) and Mn Kβ (6.5 keV). The calibration time must be long enough to achieve sufficient photon statistics for the energy resolution and energy channel calibrations. Each nominal observation starts and stops with calibrations. A typical calibration included 25 spectra of 16 s duration at the beginning and in the end of each observation. The required calibration time increases during the mission, because the half life of ^{55}Fe is about 2.7 years. The silicon PIN detector was cooled with a Peltier cooler. The operational temperature was between 0°C and -20°C. The detector HV (High Voltage) could be switched on across the PIN only after this temperature range has been reached. To shut down the detector, both

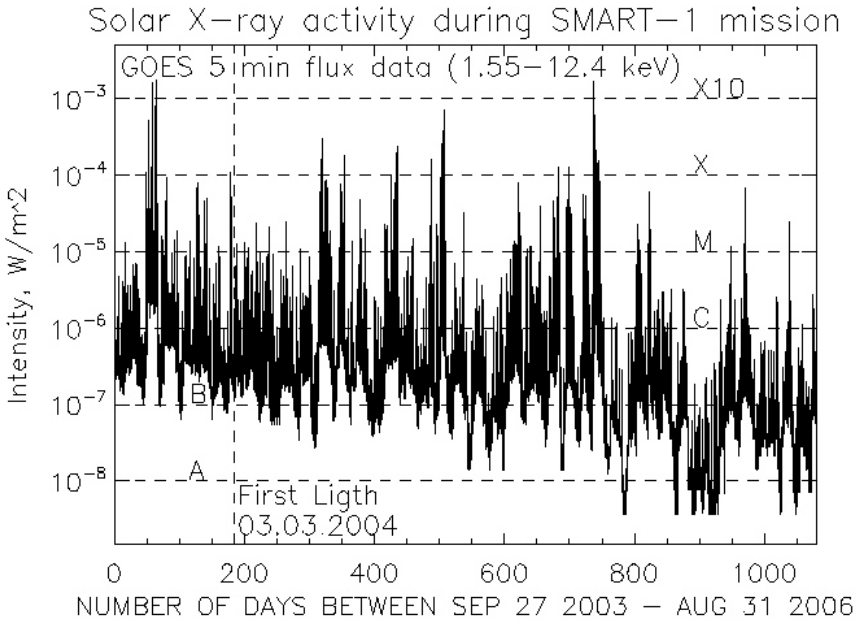

Figure 27: *The solar activity during the SMART-1 mission (NOAA).*

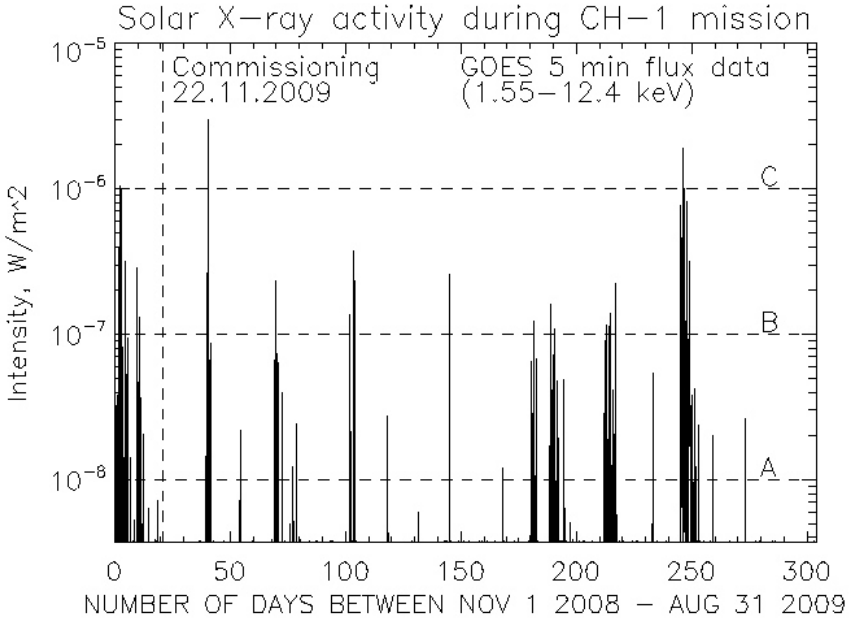

Figure 28: *The solar activity during the CH-1 mission (NOAA).*

HV and Peltier had to be switched off. There was also a third specific mode for recovering the detector performance, i.e. the annealing mode. In this mode, the Peltier current was reversed and it heated the PIN instead of cooling it. The purpose of this annealing was to heat the PIN up to +80°C for an extended, up to 5 hour period, because this reduces the defects in the detector crystal, and constantly improves the spectral resolution. The bombardment of high energy protons causes crystal defects. The accumulation of these defects increases leakage current. The increase of leakage current causes a degradation in energy resolution. A more detailed description of the XSM annealing and radiation hardness studies is shown, e.g. in the paper of (Laukkanen et al. 2005).
These solar monitors require no special pointing. They can be operated nominally as long as desired without any restrictions. According to our experience, the only operational restrictions have been a simultaneous malfunction of other detectors operated with the same control electronics as our detector.

5.3 Scientific outcome of the mutual operation solar monitors and Moon spectrometers

The link relating the common science results for XSM and D-CIXS can be found in (Grande et al. 2009). Their main achievement in this publication is the D-CIXS observation of the Ca-line from the Moon soil. The solar spectral intensity of the XSM raw data spectra are plotted as a function of time during the simultaneous D-CIXS observations. The solar activity was very high, including M- and X-level flares. Unfortunately the XSM integration was interrupted during the onset of these two M-flares and the Sun was not in the XSM FoV during the peak of the X-flare. The interruptions were mainly caused by the overheating of the common electronic box for D-CIXS and XSM.
The analysis of the CH-1 mission data is being conducted as a collaboration between the Finnish, UK, and Indian teams. The XSM solar spectral data contain only three C-level flares. The rest of the data are A- and B-level activity and are therefore statistically less important. The Moon spectrometer science team will also use the XSM spectral data to predict X-ray line fluxes from the derived composition using the GEANT4 S/W (Agostinelli et al. 2003) Monte Carlo model, compare with the observed spectrum and thus cross validate the final weight fractions. The Indian science team is very optimistic related to the data obtained by our XSM and they have already started working on it, and currently a scientific paper is being prepared as a collaboration with the Finnish team.

6 Data analysis

The section 4 dealt with the procedures required to characterize a semiconductor detector in ground calibrations. The next step is to utilize this information and generate specific tools for the final data analysis.
The raw XSM telemetry data was converted and sorted into two different FITS files. One file for HK data and an other for spectral data. The second step was to generate a FITS table, which used HK and spectral data as inputs with the corresponding S/C attitude data. This FITS table includes all essential HK values and pointing-related geometrical parameter values. The effective areas for each spectrum were also included, as well as all the data needed for the final spectral data analysis.
The analysis tool was a non-commercial spectral fitting S/W package XSPEC (Arnaud 1996). XSPEC S/W needs three standard FITS formatted files as inputs to run it. These are: a RMF *(Redistribution Matrix File)*, an ARF (*Ancillary Response File*) and a file containing the data to be analyzed. XSPEC includes a number of emission models of different kinds of astrophysical X-ray objects. First the fitted raw data, i.e. an observed spectrum containing counts in detector channels, is loaded into software. Secondly, a theoretical emission model is chosen to represent the observed target. The initial model parameters are given and the fitted data is folded with the detector response. The fitting process varies the model parameters and it is based on the minimization using the Levenberg-Marquardt algorithm. The respective best-fit parameters optimize the χ^2 statistic, which also measures the goodness of the fit. Practically one wants the reduced χ^2, i.e. χ^2/ν, to be approximately equal to one, where ν is the number of channels minus the number of model parameters. The final result of the fitting is a spectral model describing the intrinsic radiation of the observed target in physical units.
An Ancillary Response File (ARF) is also a FITS formatted file, which includes information of the effective area of the detector as a function of photon energy. The effective area depends on the QE and the obscuration factor in our solar monitors, as shown later. The effective area in the ARF provides information of the sensitivity of the detector as a function of photon energy and pointing geometry.
The spectral response of the detector is characterized by the RMF. This FITS file contains two extensions, one for the photon distribution and the other for the energy scale determination. The essential feature of the first extension of the RMF is a redistribution function, which represents the probability of a single photon to be read into a certain energy channel. This is a matrix containing probability distribution functions calculated at different energy channels. The function for silicon PIN spectrometers is composed of two Gaussian functions, one represents the main photon energy and the other represents the energy peak caused by the escape photon. The generation of these three files and the related data analysis examples are specified below.
The whole characterization process and data analysis flowchart is described in Fig. 29. The science data contains solar spectral and calibration data. The energy scale and resolution are derived from the in-flight calibration spectra, which are the inputs for the RMF. Satellite auxiliary data includes spacecraft attitude information, which is used to derive the position of the Sun in the detector FoV, i.e. ρ and θ. Angle θ influences two factors in the derivation of an effective area. Those are the obscuration factor and the QE value. Roll angle ρ is only affecting the obscuration factor. The effective area is loaded into the ARF and all these FITS-formatted three files are included into the spectral fitting with XSPEC.

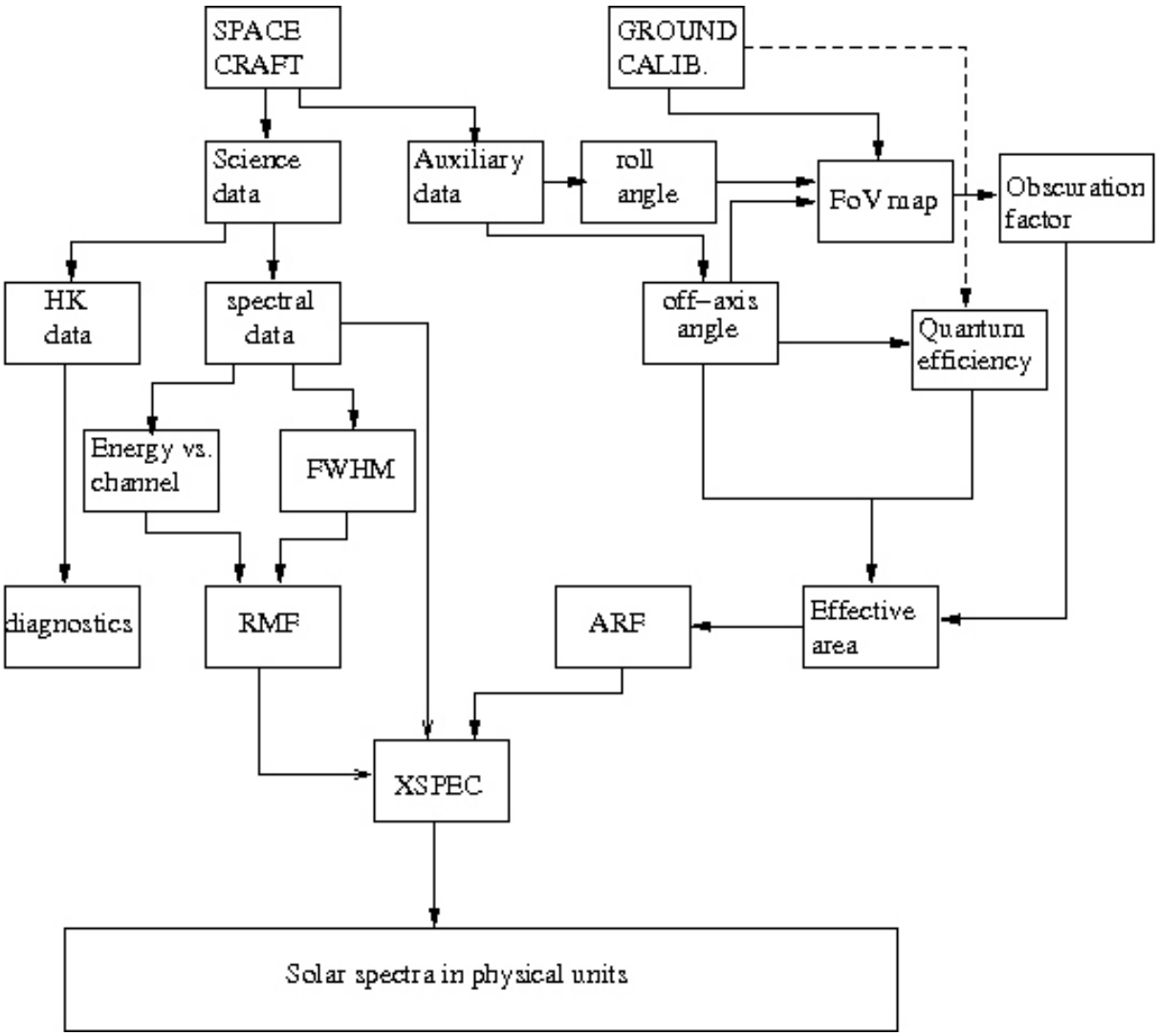

Figure 29: *A flowchart describing the generation of the instrument response for the spectral data analysis with the XSPEC S/W. The FoV map is derived from the data obtained from the ground calibrations. This array contains obscuration factors as a function of ρ and θ. The quantum efficiency curves are calculated theoretically beforehand for θ in the interval between 0° and 52°.*

6.1 Generation of the Ancillary Response File

The HK data contains several parameters controlling the in-flight operation and physical values for diagnostic purposes. The most important HK values are the sensor box and PIN detector temperatures, because the variations in temperatures modifies the detector gain. Leakage current level also has a direct influence on the detector performance. These HK values are shown in Fig. 30 and 31. The dashed vertical lines denote the epoch when the data were obtained in the following plots. These data were obtained from the SMART-1 XSM observation on the June 8th, 2004.

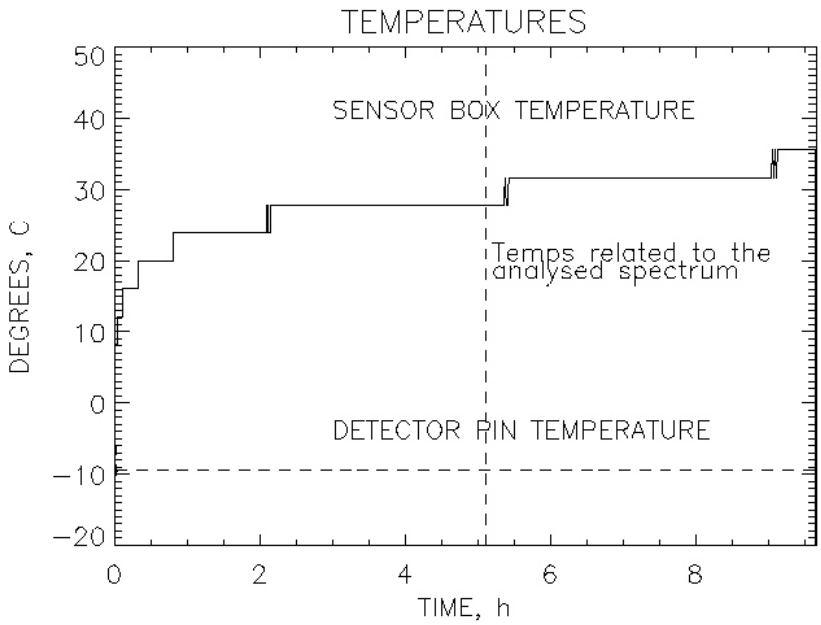

Figure 30: *Sensor box and detector PIN temperatures.*

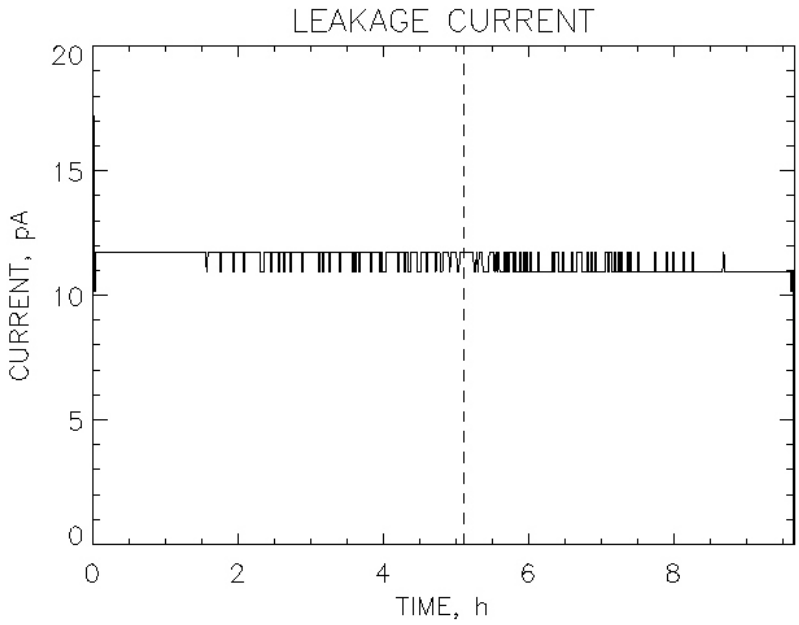

Figure 31: *Leakage current during a long observation.*

This particular integration lasted about 9h 40m. All following examples are based on this observation. The first example is the ARF, which contains information of the effective area. This effective area describes the geometric detection area of the PIN detector as a function of photon energy. To build up this file, the pointing geometry during the observation must be known, i.e. the angles θ and ρ must be calculated from the S/C attitude data. This gives the position of the Sun in the FoV. The next example shows the changes of these angles during a long integration (Fig. 32). The general formula describing the effective area is

$$A_{\rm eff}(\theta, \rho) = A_{\rm geom} QE(\theta) OB(\theta, \rho). \tag{8}$$

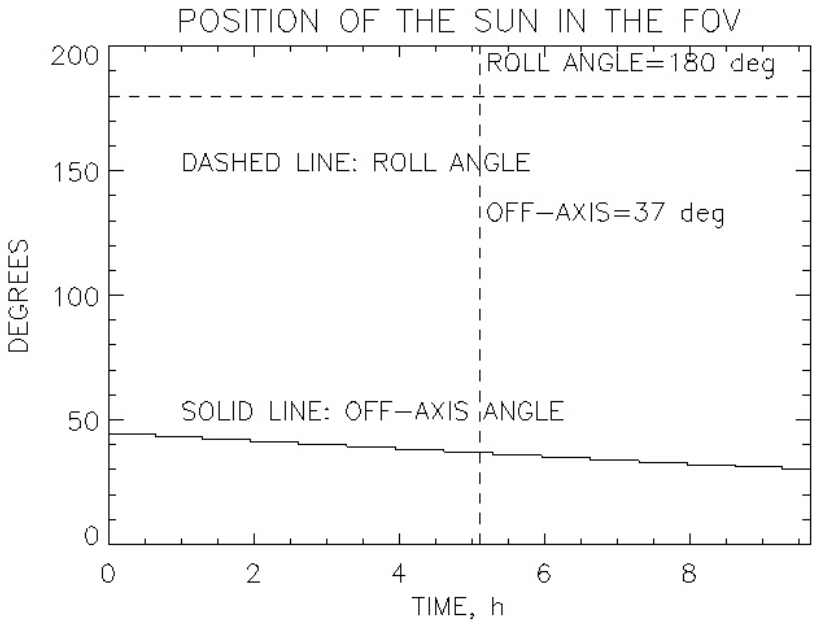

Figure 32: *Off-axis and roll angles.*

The geometrical area $A_{\rm geom}$ has a constant value, which is determined as explained in Section 4.1.1. (In an ideal conditions this value can be calculated as as a function of θ and neglecting the use of the value OB. The mathematical formula for this parameter is solved separately in Appendix 1). The second parameter, quantum efficiency QE, depends only on θ. When the incident angle is steeper, the photons have to penetrate a longer path through the filters. The third parameter, obscuration factor, OB, is also a function of θ and ρ. The applied and suitable OB was selected from the calibrated FoV map array. This array contains the OB factor values for each θ and ρ pair. The OB range is between 0 and 1. If OB is equal to 1, the whole PIN is illuminated by the Sun. If OB is 0, the Sun is beyond the horizon of the collimator, i.e. the PIN is fully in shadow. A contour plot of the FoV map is shown in Fig. 33. The respective $OB \approx 0.8$ for θ=37° is marked with an asterisk. It is horizontally left from the origin on the X-axis.

The final $A_{\rm eff}$-curves for all θ angles during this particular integration are shown in Fig. 34. The enhanced bold curve represents the $A_{\rm eff}$ for θ= 37° and ρ=180°.

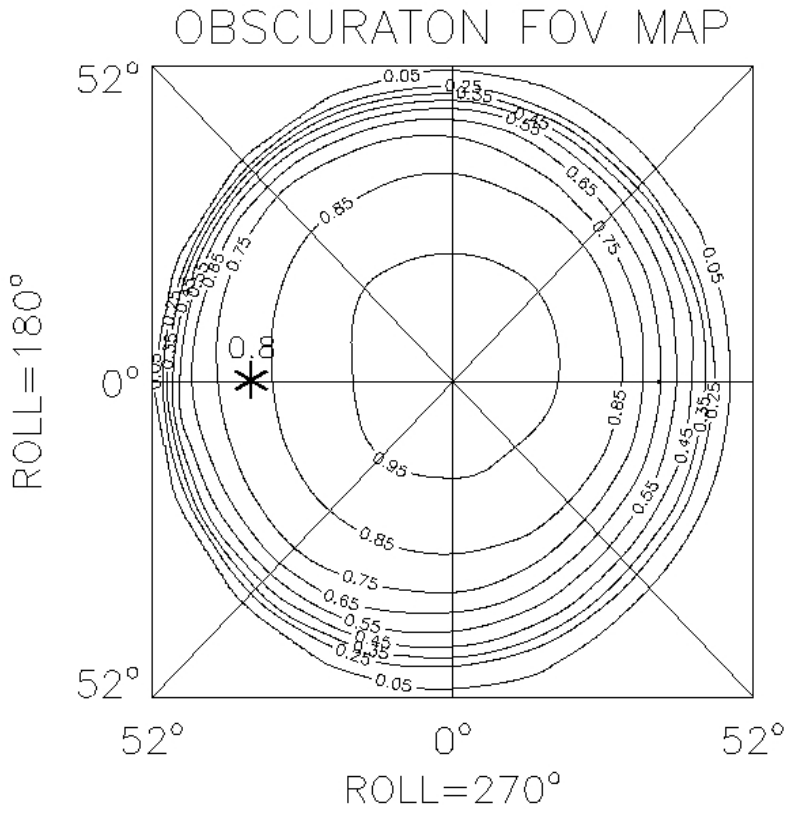

Figure 33: *A contour plot representing the numerical values of the obscuration factor array, OB(θ, ρ). The accuracy of the OB decreases in the peripheral area of the array vales due to the steep declining of sensitivity. The angular size of the Sun is about 0.5° at 1 AU. The coronal X-ray emitting area expands during a high solar activity. The X-ray emitting area within the solar corona is more or less arbitrary, and it is impossible to determine exact values for θ and ρ. This must be taken into account when analyzing data obtained at greater θ angles.*

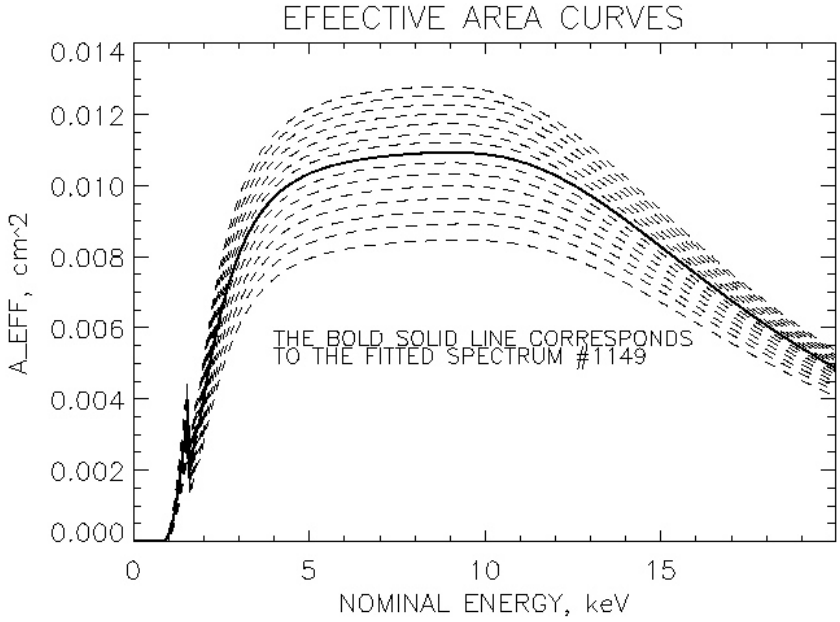

Figure 34: *Effective area curves with different θ angles. The ρ angle is constant 180° during this observation.*

6.2 Generation of the Redistribution Matrix File

The Redistribution Matrix File was generated from the in-flight calibration spectra. The in-flight calibration source attached to the shutter emits four fluorescence lines: Ti Kα (4.5 keV), Ti Kβ (4.9 keV), Mn Kα (5.9 keV) and Mn Kβ (6.5 keV). The two α-lines were used for the channel versus energy calibration. The calibration integrations were made before and after the solar observation (see Fig. 35). This gave two sets of calibration spectra for the spectral fitting. The energy scale gain shifts, if the box temperature changes. It is therefore necessary to check the evolution of the sensor box temperature in the HK data. This allows the application of a corrected energy scale. One can "tune" by interpolation for the exact epoch when the analyzed spectrum was measured. The line centroids of the two emission lines at 4.5 keV and 5.9 keV were derived by Gaussian routine of IDL S/W. The line centroid locations were then used for solving the linear relation between the channel and photon energy. This energy versus channel information was then fed into the second extension of the RMF called as *EBOUNDS*. This extension solves the energy scale of the data. The energy versus channel plot is shown in Fig. 36. The linearity of the PIN detectors were tested between 1.487 keV (Al Kα) and 14.96 keV (Rb Kα) with the laboratory MCA. It was assumed, that the flight electronics operated linearly trough the whole energy scale. There was no reason to suspect non-linearity between 1.8 and 10 keV, which was the energy range of interest. This scale was also used for the observation made on June 8th, 2004. The Mn Kα and Ti Kα lines were only utilized in energy scale and resolution determination. The Ti Kβ lines were too weak for this purpose and more or less blended with the Kα lines. It was also noticed, that the centroid of the Mn Kβ line suffered from the blending effect with the Kα and could therefore be generally too difficult task for the IDL Gauss-fit routine to perform it with a sufficient accuracy. Hence this Mn Kβ line was not used.

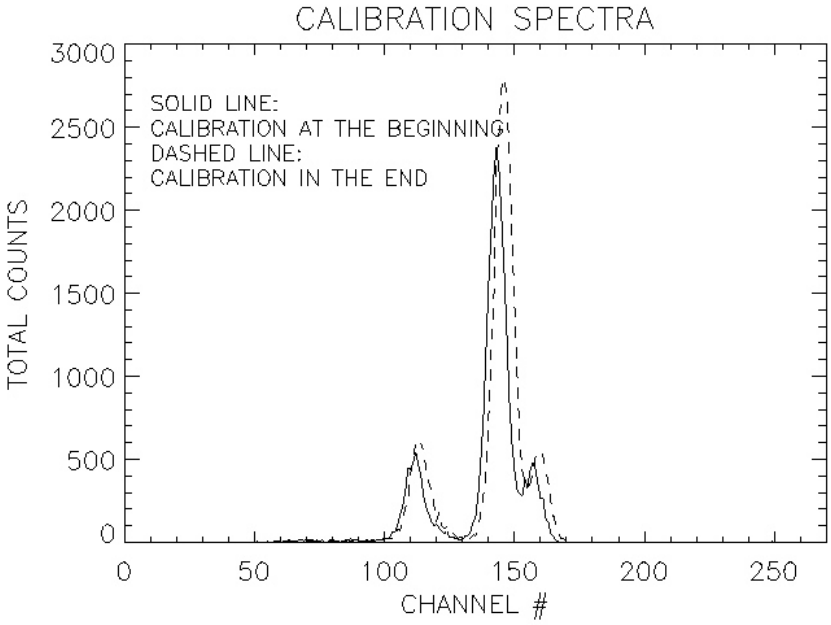

Figure 35: *Calibration spectra (June 8th, 2004).*

The same calibration data yielded the respective energy resolution of the detector. Only Ti Kα and Mn Kα lines were used to determine the channel energy resolution. Again, the same IDL Gaussian fitting routine gave the FWHM for these two lines. The Ti Kα

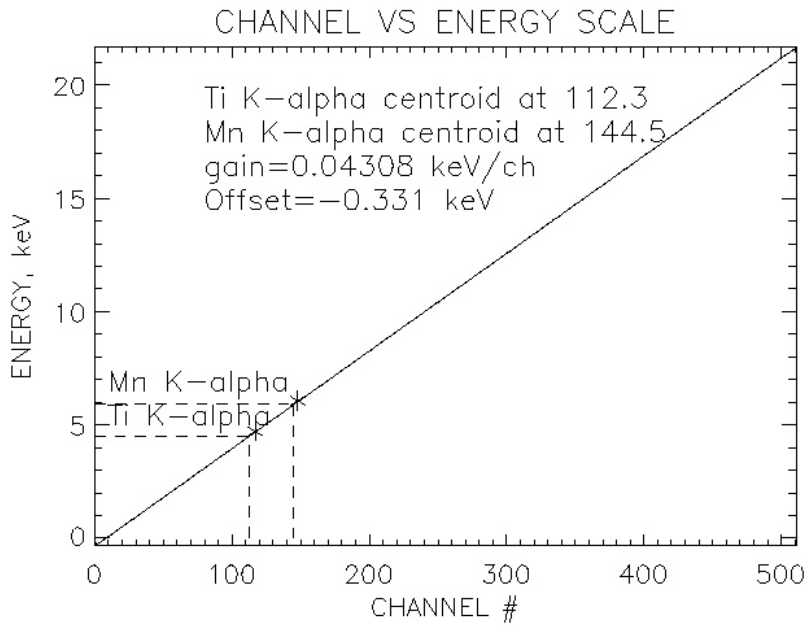

Figure 36: *Energy versus channel relation (June 8th, 2004).*

was occasionally quite weak and blended with the Ti Kβ line, which made it impossible to obtain the correct line width with the Gaussian IDL routine. The relation between the energy resolution and photon energy was

$$\Delta E = \sqrt{aE + b},$$

where the parameter a represents the detector PIN and pre-amplifier noise. The parameter b represents the noise generated in the the readout electronics. By squaring the formula to the form $\Delta E^2 = aE + b$, one can solve a and b from a linear fit. The solution for the June 8^{th} 2004 data is illustrated in Fig. 37.

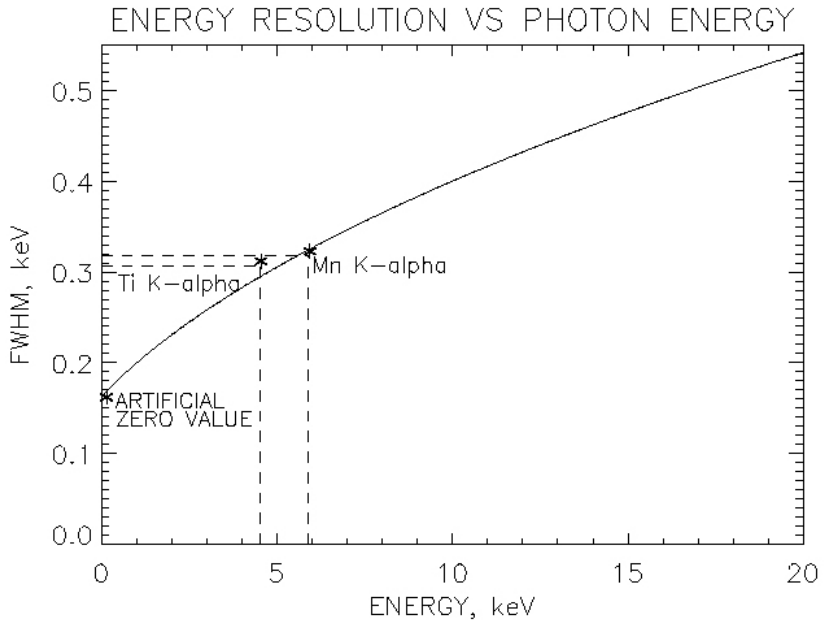

Figure 37: *Energy resolution as a function of photon energy (June 8th, 2004.)*

The energy resolution versus photon energy calibration was then used in the first extension of the RMF, which is an array containing redistribution functions for specific energy intervals. These redistribution functions merely determine the probability of detecting a mono-energetic photon of energy $h\nu$ at E. For a lower resolution, the measured photon of energy $h\nu$ deviates more from the real value E. In an ideal detector, this probability would always be 1, i.e. $h\nu$ would be equal to E for every measured photon. The shape of the RMF contour map is shown in Fig. 38. This function is a sum of two Gaussian functions. The higher main peak represents the distribution for the mono energetic photons detected. The smaller Gaussian represents the silicon escape peak. The silicon escape peak is always 1.747 keV lower than the main peak. This constant shift is equal to the energy of a photo electron, which escapes from the detector without delivering its energy inside the active volume of the PIN. The Gaussian functions (Tikkanen 1994) in Fig. 38 have the form

$$G(E) = I_{\mathrm{h}\nu} \exp\left[-\frac{(E - h\nu)^2}{2\sigma^2}\right] \tag{9}$$

$$Esc(E) = I_{\mathrm{esc}} \exp\left[-\frac{(h\nu - E - E_{\mathrm{esc}})^2}{2\sigma^2}\right], \tag{10}$$

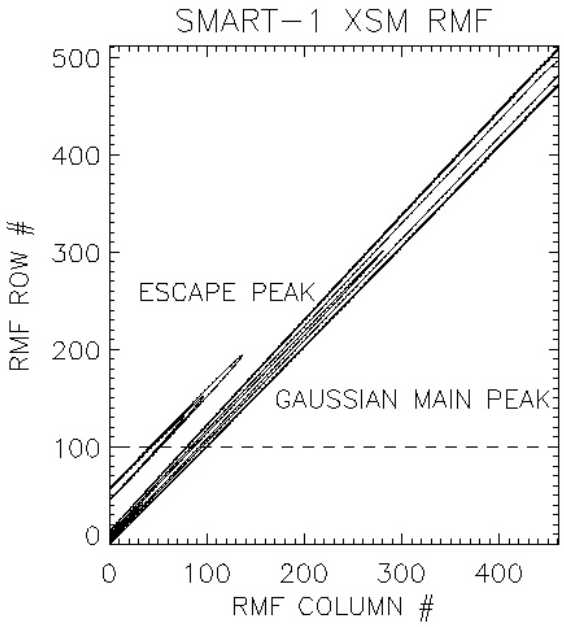

Figure 38: *A contour plot representing the Redistribution Matrix File (June 8th, 2004).*

where the parameter $h\nu$ is the photon energy. The standard deviation σ represents the total noise of the detector system determined from the FWHM-curve. A single logarithmic redistribution function obtained from the row 100 of this particular RMF is shown in Fig. 39. The dashed horizontal line in the previous Fig. 38 indicates the location of this single redistribution function.

6.3 Spectral fitting

Two different data analysis examples are given here. The first example deals with the data of the previous section, i.e. the spectrum obtained from the onset of the C1 flare on the 8^{th} of June 2004. This example of fitting a single solar spectrum is introduced for

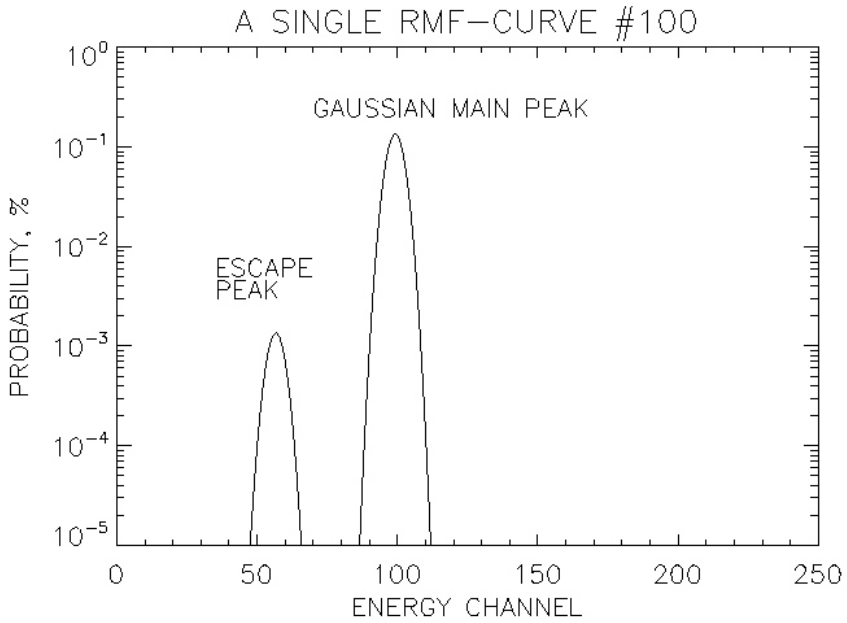

Figure 39: *A single redistribution function representing the row 100.*

showing the performance of our spectrometer equipped with 512 channels each having a width of about 40 eV. Our solar monitors operated as spectrometers capable of measuring simultaneously the continuum and the line emission of a C-flare within 16 s. It is also worth to point out, that our solar monitors had an in-flight calibration source, which made them more reliable than similar PIN spectrometers, e.g. on-board MESSENGER and NEAR.
The second example deals with the C4.6 flare data observed on May 24th, 2004. This analysis example illustrates the ability of our solar monitors to measure the time evolution of the spectral parameters with a time resolution of 16 s. The applied bremsstrahlung spectral model enables to derive the respective temperature, emission measure and flux as a function of time along the flare event. The time evolution of the line emission components can be also modeled.

6.3.1 Example of a C1 flare analysis

The raw data X-ray light curve is shown in Fig. 40. The vertical dashed line represents the 16 second integration of the solar X-ray spectrum used in this example. The example data plot is shown in Fig. 41. The vertical axis gives the number of counts measured during 16 s.

The fitted energy interval was between 1.88 keV and 9.0 keV. The applied spectral model was a bremsstrahlung with two Gaussian lines. The results are given in Table 10. The folded spectral model and the residuals of this model are shown in Fig. 42. The final unfolded solar spectrum is shown in Fig. 43. This solar spectrum is in real physical units, i.e. the desired final result of this analysis. The respective GOES flux (1.1×10^{-6}W/m^2) for this event was the same as derived from the simultaneous XSM data.

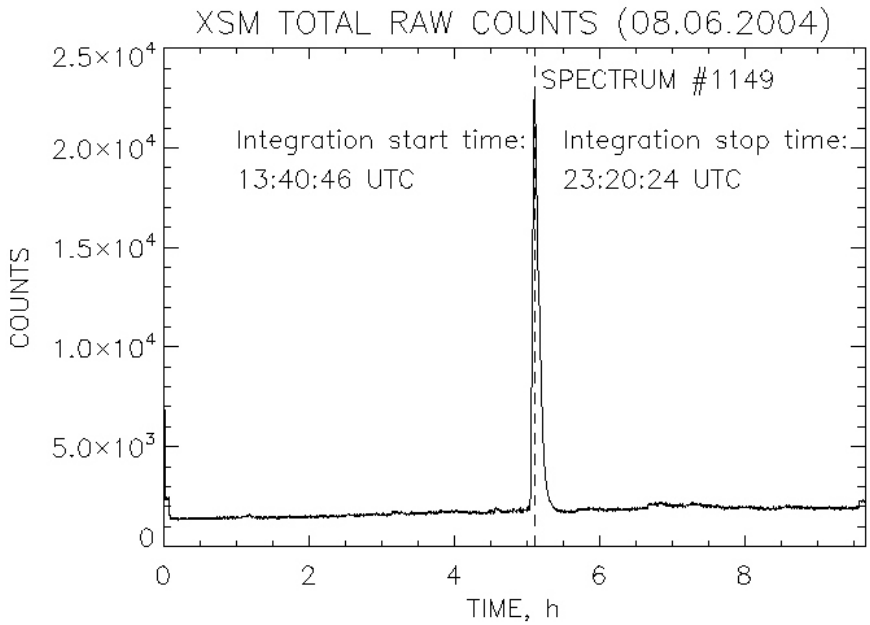

Figure 40: *Raw data total counts as a function of time. The dashed vertical line indicates the position of the analyzed spectrum of 16 s.*

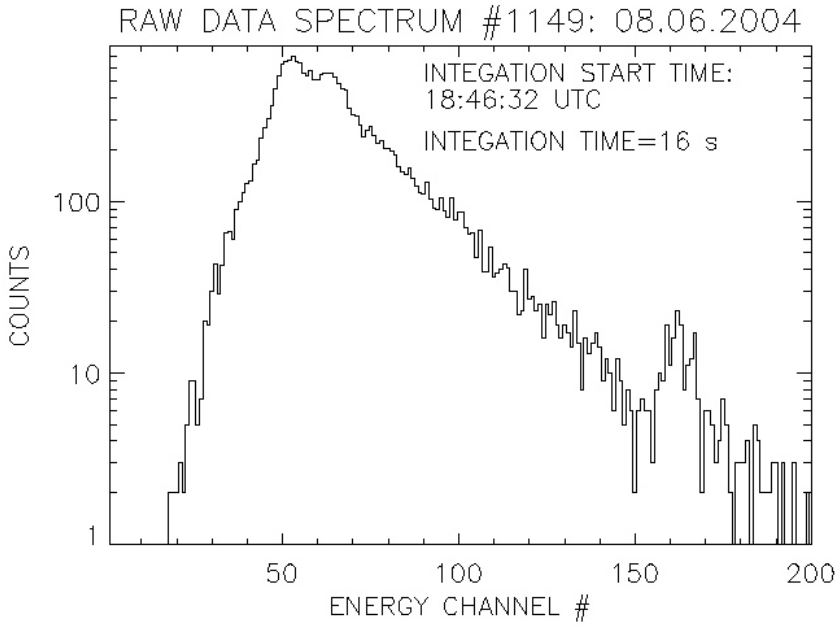

Figure 41: *Raw data spectrum.*

Model Component	Unit	Value	Error	Line flux ($photons/cm^2/s$)
bremss (kT)	keV	0.929	±0.003	-
Gaussian (LineE)	keV	2.49	±0.012	8695±805
Gaussian (LineE)	keV	6.50	±0.214	592±71

Table 10: *The spectral fitting parameters of the analyzed C1-flare. The derived flux of* $1.1 \times 10^{-6}\mathrm{W/m^2}$ *in the range of 1.55-12.4 keV was exactly the same as the simultaneous flux measured by GOES. The flare temperature corresponds to about 11 MK. The most probable candidate for the line at 2.49 keV would be S XV and the line at 6.50 keV would belong to Fe XX.*

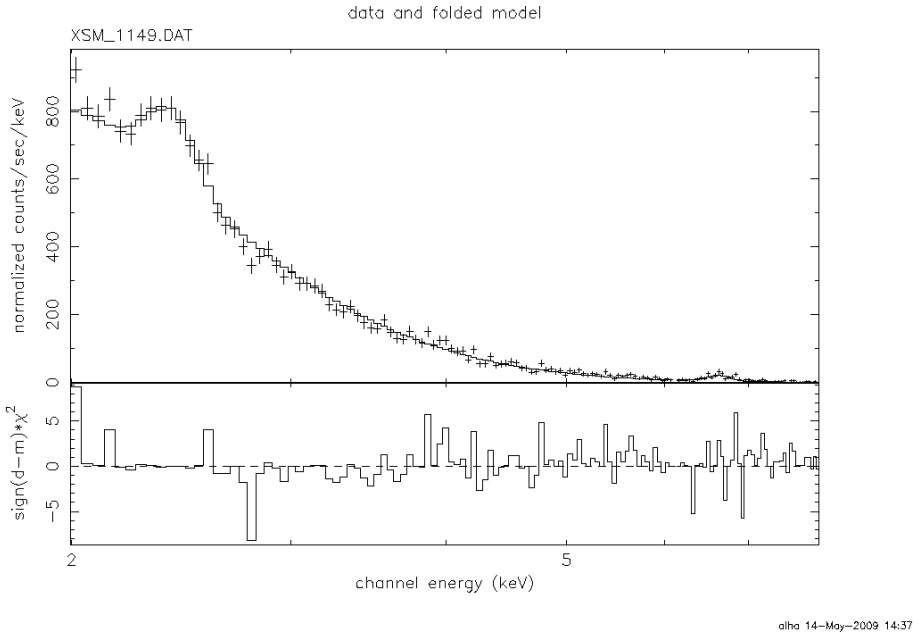

Figure 42: *Folded spectrum and the residuals of the fit obtained from the XSPEC S/W. The plus signs represent raw data points.*

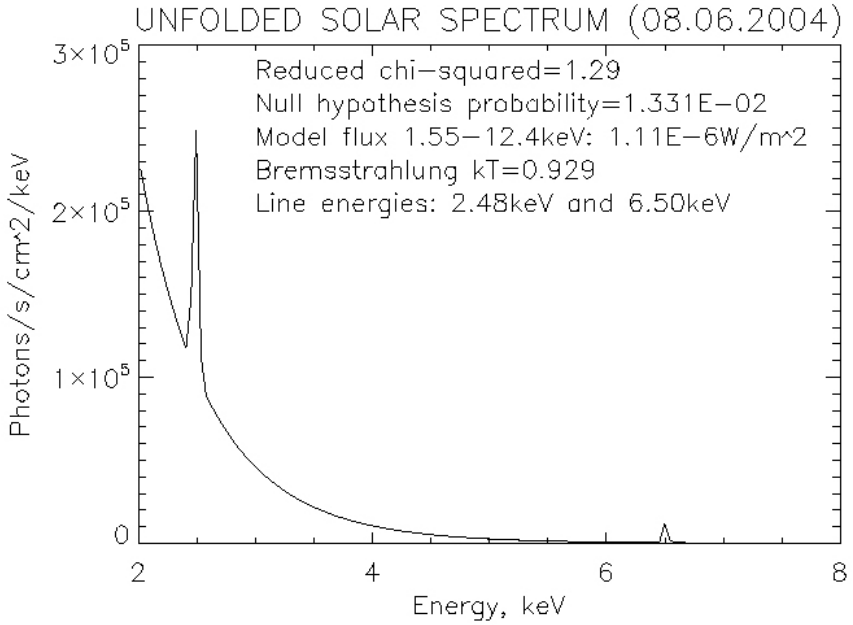

Figure 43: *Unfolded solar C1-flare spectrum.*

6.3.2 Temporal evolution of a C-level flare

Our XSM on-board SMART-1 observed a C4.6 level flare on May 24th, 2004. These data were spectroscopically fitted with XSPEC S/W from the onset to the declining phase of the flare. This event was analyzed with time resolution of 16 seconds. This gave 175 individual spectra. The spectroscopic model in this analysis was a bremsstrahlung with several Gaussian lines. The line energies and respective line intensities varied during the flare. The analysis of this flare showed how the plasma temperature (T), flux (F) and emission measure (EM) evolved as a function of time. The XSM flux curve was also compared to the simultaneous GOES 1 minute data as shown in Fig. 44. The temperature versus flux and temperature versus emission measure were also determined.

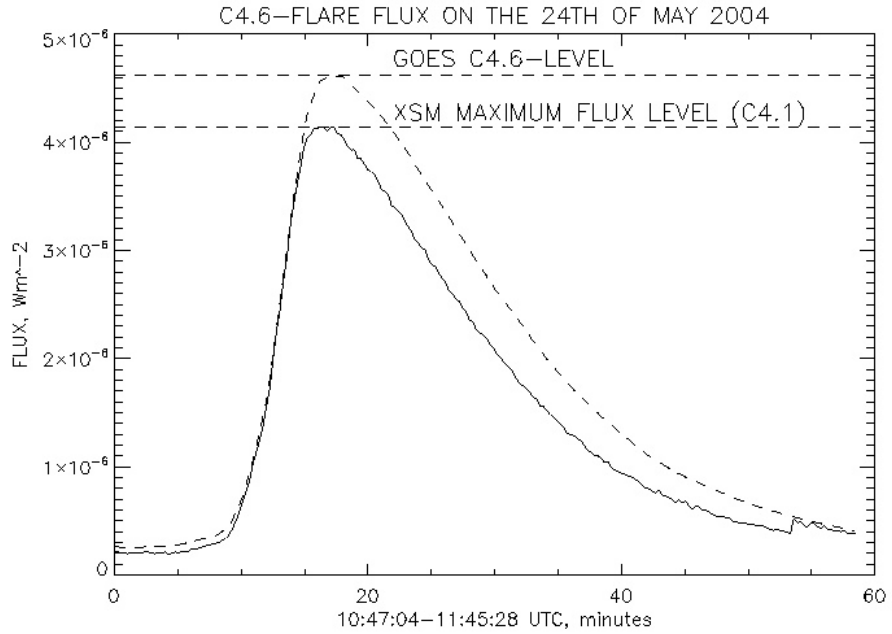

Figure 44: *XSM and GOES fluxes in the range of 1.55 keV - 12.4 keV. The XSM observed fluxes (solid line) were spectroscopically fitted with the energy resolution less than 250 eV at 5.9 keV and the time resolution of 16 s.*

The XSM fluxes were calculated at the same energy band as is used in the lower GOES band, between 1.44 and 12.4 keV. In this observation, the constant off-axis angle was 39° and roll angle was 0°, i.e. the pointing was steady. There was about 10 % difference between GOES and XSM fluxes at the peak of the flare. The reason for this difference might be the large value of θ=39°. The obscuration factors OB for larger off-axis angles are more prone to error, since the OB changes very steeply with respect to θ, and even errors of the order of 1° may cause large errors in OB.

The temperature for each spectrum was calculated with the aid of XSPEC bremsstrahlung model parameter 1, i.e. the plasma temperature in keV (1 eV corresponds to 11600 K). The maximum C4.6 flare temperature was 21.5 MK. The temperature evolution is plotted in Fig. 45.
The flux versus temperature is plotted in Fig. 46. One can clearly see that the flux at any T is stronger during the onset of the flare than during the decay. This curve shows a hysteresis like loop, where the flux is much lower at the declining phase.
The emission measure describes the amount of emitting plasma that causes the observed

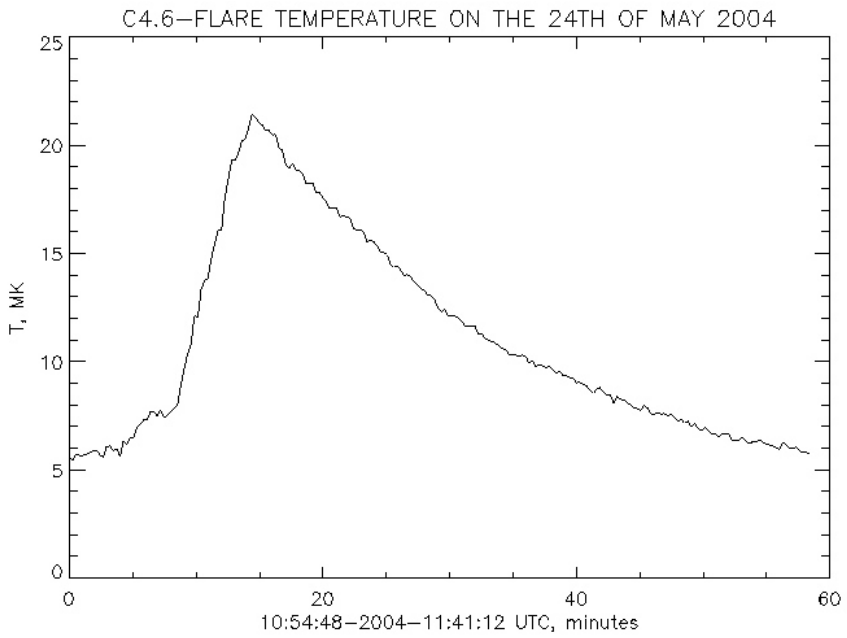

Figure 45: *Evolution of the flare temperature.*

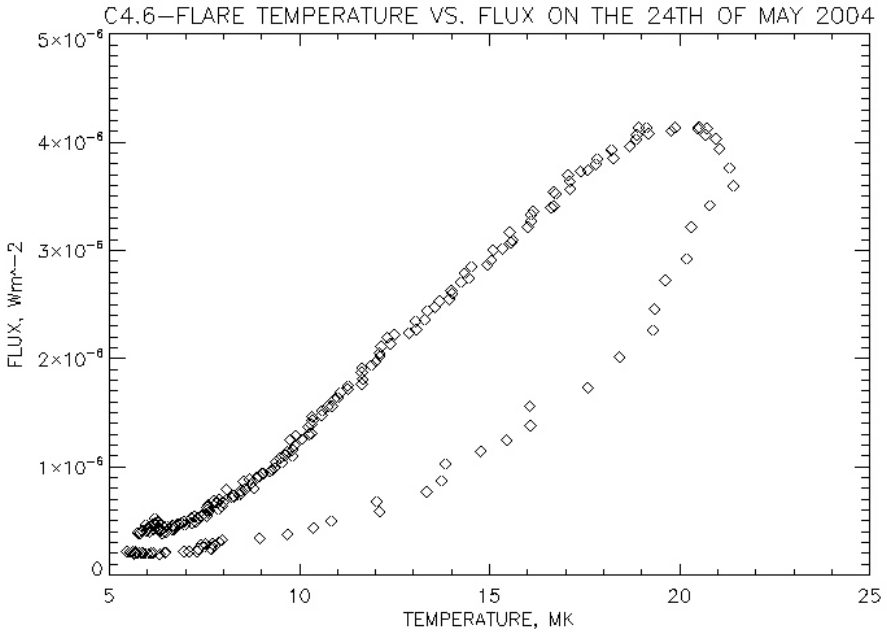

Figure 46: *Flux vs. temperature during the flare.*

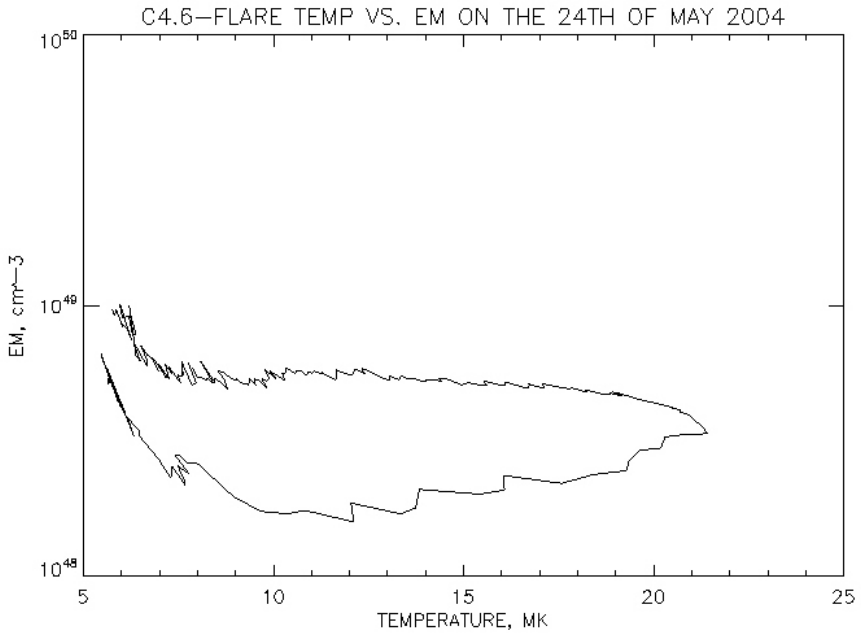

Figure 47: *Temperature vs. emission measure during the flare.*

X-ray flux. Emission measure is derived from spectroscopic observations. Its value depends on assumptions about the absolute element abundances and ionization fractions of the emitting ions. The emission measure of the plasma could be also derived from the XSPEC modeling. The bremsstrahlung parameter (Kellogg et al. 1975) is

$$K = \frac{3.02 \times 10^{-15}}{4\pi D^2} \int n_{\rm e} n_{\rm I} dV, \tag{11}$$

where D is the distance to the Sun (cm), while $n_{\rm e}$ and $n_{\rm I}$ are the electron and ion densities (cm^{-3}). The emission measure is

$$EM = \int n_{\rm e} n_{\rm I} dV = \frac{4K\pi D^2}{3.02 \times 10^{-15}}. \tag{12}$$

The correlation between temperature and emission measure based on the above relations is shown in Fig. 47. The connection between these two physical parameters also show a loop like structure. The emission measure is lower during the flare onset and higher at the declining phase. This *EM-T* diagram of this particular C-flare agrees well with earlier results for the stellar and solar flares (Shibata 2002). The log-log plot in Fig. 48 includes observed emission measures and electron temperature relations of different targets, e.g. solar flares and solar micro-flares observed by Yohkoh SXT (stripped areas). Four stellar flares (asterisks), a protostellar flare (diamond), a T Tauri stellar flare (weak-lined diamond T Tauri star) and a stellar flare of AB Dor (plus sign) are shown in Fig. 48. These stellar data are based on the BeppoSax observations. The gray rectangle in the plot below represents the emission measure and temperature values derived from the XSM C-level flare. It covers the same area as derived from the Yohkoh SXT solar observations. Hence a single XSM observation of a C flare with an integration time less than 1 hour can reveal the relation between the EM and flare temperature very efficiently.

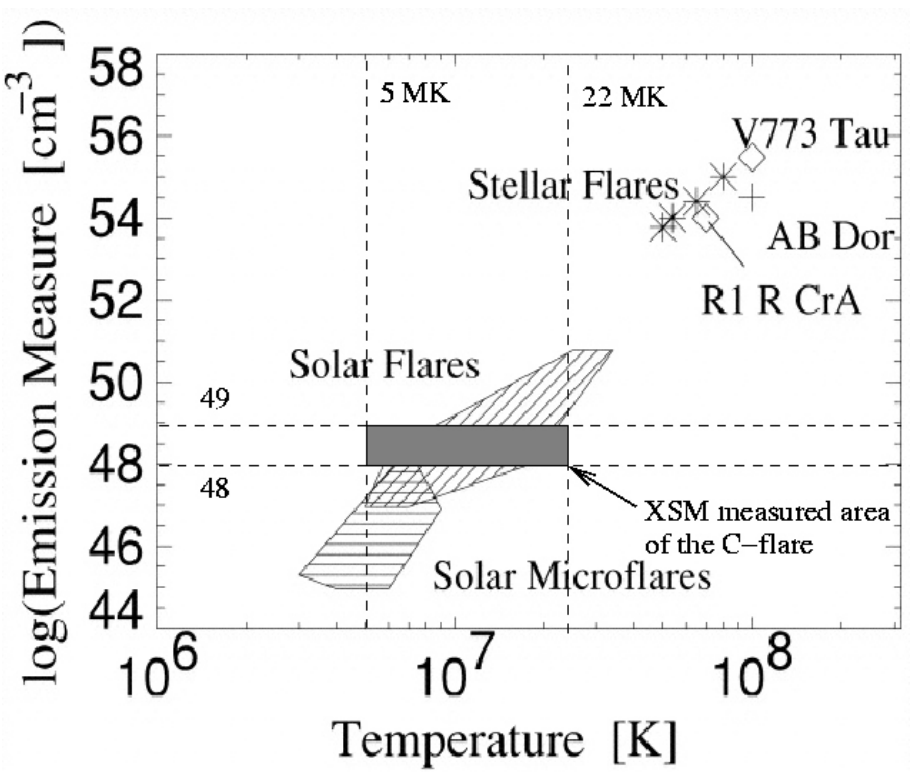

Figure 48: *Temperature vs. emission measure derived with Yohkoh XST and BeppoSAX. SXT was a Wolter type-1 X-ray telescope dedicated to solar observations. BeppoSAX was an astrophysical X-ray observatory (Shibata 2002). The gray elongated rectangle in the middle of the plot represents our results derived from the single C4.6-flare observed by SMART-1 XSM through the whole flare with the total integration time of about 46 min. The dashed lines limiting the box were obtained from Fig. 47.*

7 Summary

Here I will give an overview of the publications of this thesis. Author's contribution to these papers is also briefly explained.

7.1 Paper I

The SMART-1 X-ray solar monitor (XSM): calibrations for D-CIXS and independent coronal science. This publication presents the science goals of XSM. The main task of XSM was to be an auxiliary detector for the D-CIXS, which measures solar X-ray induced fluorescence emission from the surface of the Moon. XSM was able to do independent solar science. The performance of XSM was thoroughly tested at different solar activity levels. The supplementing data were obtained from GOES detectors, which operate in an over-lapping energy band. The technical design and the operation of XSM was described. This SMART-1 XSM was our first wide FoV non-imaging X-ray solar monitor, which used HP silicon PIN as an X-ray detecting element.

7.2 Paper II

The in-flight performance of the X-ray Solar Monitor (XSM) on-board SMART-1. This paper was the follow-up of Paper I. It concentrates on the real XSM in-flight performance. The ground calibration results versus in-flight performance were discussed. The first solar data analysis was also presented. The generation of the required standard S/W files for spectral analysis were also described.

7.3 Paper III

Solar Intensity X-ray and particle Spectrometer (SIXS). This paper introduced a new solar X-ray spectrometer equipped with three similar wide FoV PIN detectors, each pointing to different directions. These X-ray detectors will be on-board the ESA's Bepi-Colombo MPO mission to Mercury. This instrument also has a particle detector. The instrument performance was simulated with SMART-1 XSM data, which was scaled to observations made at 0.4 AU. The technical design and science goals were described. The basic operation of the instrument was also explained.

7.4 Paper IV

Off-solar observations and a new detector concept with a concentrator optics. In this paper, I introduced two specific off-solar observations made by SMART-1 XSM. During these two observations, the Sun was outside the detector FoV and the observed spectra included several clearly distinguishable X-ray emission lines originating from the expanded solar corona. Some odd emission lines were also found in these spectra, e.g. the Cr $K\alpha$ line at about 4.5 KeV. This Cr fluorescence line most probably originated from our own PIN aperture made of steel alloy containing chromium.
The last sections of this paper describe the design of a new type an X-ray concentrator equipped with XSM generic spectrometer. The moderate size FoV optics of this kind would enable the mapping of the spatial distribution of the X-ray emission from expanded

solar corona.

7.5 Paper V

Ground calibrations of the Chandrayaan-1 X-ray Solar Monitor (XSM). This publication summarized the ground calibrations of the CH-1 XSM. It described all necessary calibrations routines for characterizing this non-imaging semi-conductor X-ray solar monitor. The first data acquired with this instrument and the in-flight operation were also briefly described.

7.6 Author's contribution

My personal contribution to the above five publications is the following. In Paper I, I made the GOES related flux plots. The sensitivity calculation of the QE-curve and the determination of effective area of of the detector were also mine, as well as the schematic drawing in Fig. 6. I also contributed to the detector technical and operational design and determined the final performance and properties of XSM. I participated to the detector ground calibrations. For paper II, I generated the files required for spectral analysis using the ground and in-flight calibrations. All the data analysis examples described in Paper II were made by Author. I wrote the first versions of Paper II. For paper III, I did all the SIXS X-ray performance and science simulations described in section 4.1. I also contributed to the technical design and operation planning of the instrument. I wrote Paper IV. In Paper V, I did the ground calibrations in collaboration with another person from the X-ray laboratory. I wrote Paper V alone, but naturally received some editorial help from my co-authors.

8 Conclusions and future prospects

The single pixel non-imaging detector is the most simple type of solid state detector. Despite of their simplicity, the characterization of these detectors is a demanding process. Every PIN detector has its own individual characteristics. The fabrication of a PIN detector and the collimating structures is mainly hand made. Hence the dimensional tolerances must be considered by performing careful ground calibrations, as explained in this thesis. The actual detector performance is known after the calibration process. All other procedures connected to different operational modes must also be tested. There is always a brief time slot between the ground calibrations and the launch when the possible malfunctions and anomalous behavior of the detector can be fixed. It is worth pointing out that the development of the analysis S/W for the detector is closely connected to the results obtained from the ground calibrations. The reliable final spectral analysis requires extreme care in the following two tasks: 1. The detector must be adequately characterized together with the flight electronics. The properties of the detector under every imaginable operational conditions must be thoroughly described. 2. The analysis S/W must include all the performance values of the detector.

8.1 XSM generic detector equipped with a concentrator optics

The FoV sizes in our two XSM detectors have been large, about 52°. This large FoV simplified the operation of the instrument during observations. The pointing requirements of such detectors are not very strict. These wide FoV detectors were operated as auxiliary instruments for main nadir pointing fluorescence X-ray spectrometers, which were mapping elemental abundances of the surface of a planetary bodies (Crawford et al. 2009). The main scientific task of these auxiliary X-ray instruments was to support the final spectral analysis made by the Moon fluorescent instrument. Our auxiliary measurements delivered the primary solar X-ray emission spectrum for scaling purposes. Despite of this auxiliary role, our XSM on-board SMART-1 acquired plenty of solar X-ray data independently of the operational requirements set by the main lunar soil observing DCIXS spectrometer (Grande 2009).

The FoV size of a PIN detector can be reduced with concentrator optics. The Author has made a rough design for concentrator optics in XSM generic detector. This tubular reflector system with baffles reduces the circular FoV half cone angle to less than 1°. The optics enhance the efficiency of the system, if the dimensions were optimally designed. This kind of a detector with a moderate size FoV would enable a morphological spectroscopic study of the expanded solar corona during high activity levels. Such instrument system would be ideal for mapping radial distribution of the coronal X-ray emission. This moderate size FoV detector would require a 3D-stabilized or a rotating platform, which would allow flexible observing programs. This relatively inexpensive and simple instrument would suit well for an auxiliary instrument on-board some future solar mission having an EUV or an X-ray telescope. The optical axis of this instrument optics should point a few degrees off from the optical axis of the main telescope. This would allow the measurement of X-ray emission originating only from the outer corona, i.e. the solar disc would be fully out of the FoV.

8.2 Solar Intensity X-ray Spectrometer (SIXS) on-board BepiColombo

The design and fabrication phase of the scientific instruments of the ESA's BepiColombo mission to Mercury began a few years ago (Schulz & Benkhoff 2006). The launch should take place in 2014. The operational phase on the Hermean orbit should begin in 2020. One of the scientific payload instrument on-board BepiColombo S/C will be an XSM generic X-ray solar spectrometer named as SIXS. This instrument will be equipped with three Si PIN detectors. The selected detector material was changed from GaAs into Si in June 2009. The optical axis of each of these PIN detectors will point to a different direction. The detector FoVs will cover a one quadrant of the whole celestial sphere. The mechanical design of the SIXS pointing geometry is shown in Fig. 49, while the Mercator projection map of the SIXS FoV configuration is shown in Fig. 50. The bold closed curve represents the spherical lune of π sterad, i.e. it equals 1/4 of the whole sky. Each of the FoV is circular, having the theoretical half cone angles of 50.4° (middle detector) and 48.5° (side detectors).

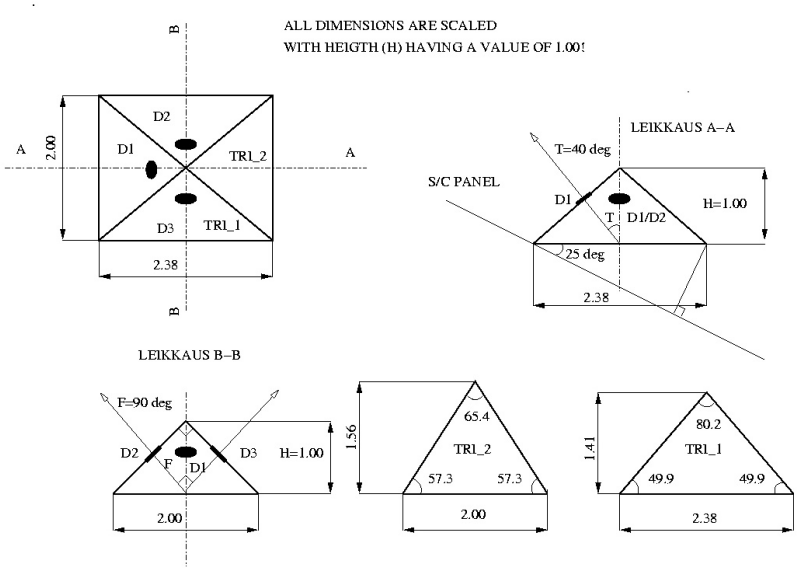

Figure 49: *A tetrahedral structural model of SIXS clarifying the detector configuration and helping the mechanical design.*

The QE-curves of the Si PINs were determined and the effective areas for each of the detector $A_{\rm eff}$ were modeled as of function of θ. The calibration for SIXS started in May 2009. The aim was to carry out similar ground calibration routines, as explained before. These calibrations will be more demanding than with the two former XSM detectors. The FoV sensitivity scan will pose a methodological challenge, because the aperture stop diameters of the side detectors will only be 0.3 mm. Due to the complex geometrical pointing configuration, some special mechanical adapters for fixing purposes must be designed. This will enable accurate rotations of the calibrated detector on the horizontal plane during the FoV scanning. If we fail to do this test, then we can in any case calculate the FoV map theoretically. The calculation of geometric detector area $A_{\rm geom}$ for a circular FoV as a function of an off-axis θ angle is presented in Appendix 1. Our plot in Fig. 51 illustrates the SIXS geometric detector areas calculated with the nominal dimensions. The offset-

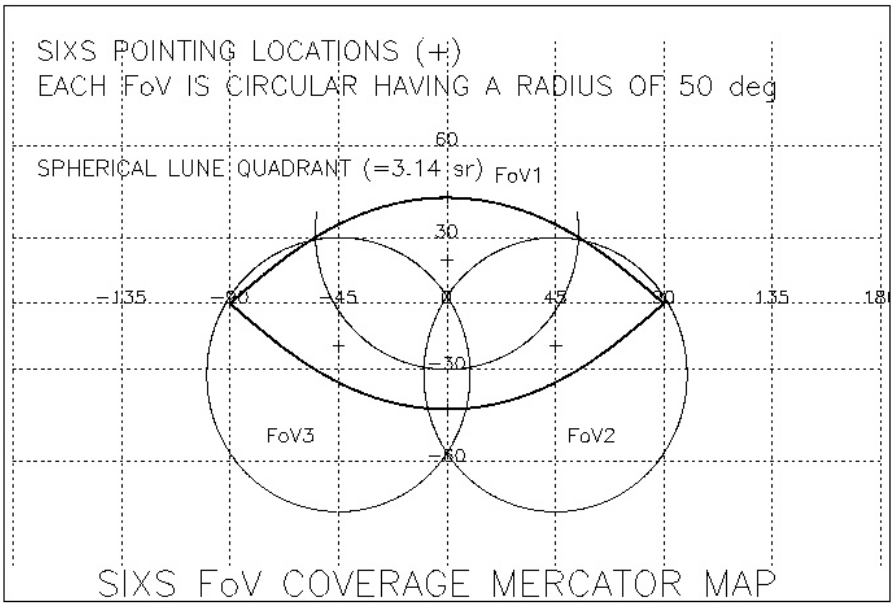

Figure 50: *Mercator map illustrating the detector pointing configuration and the sizes of FoV of the SIXS instrument.*

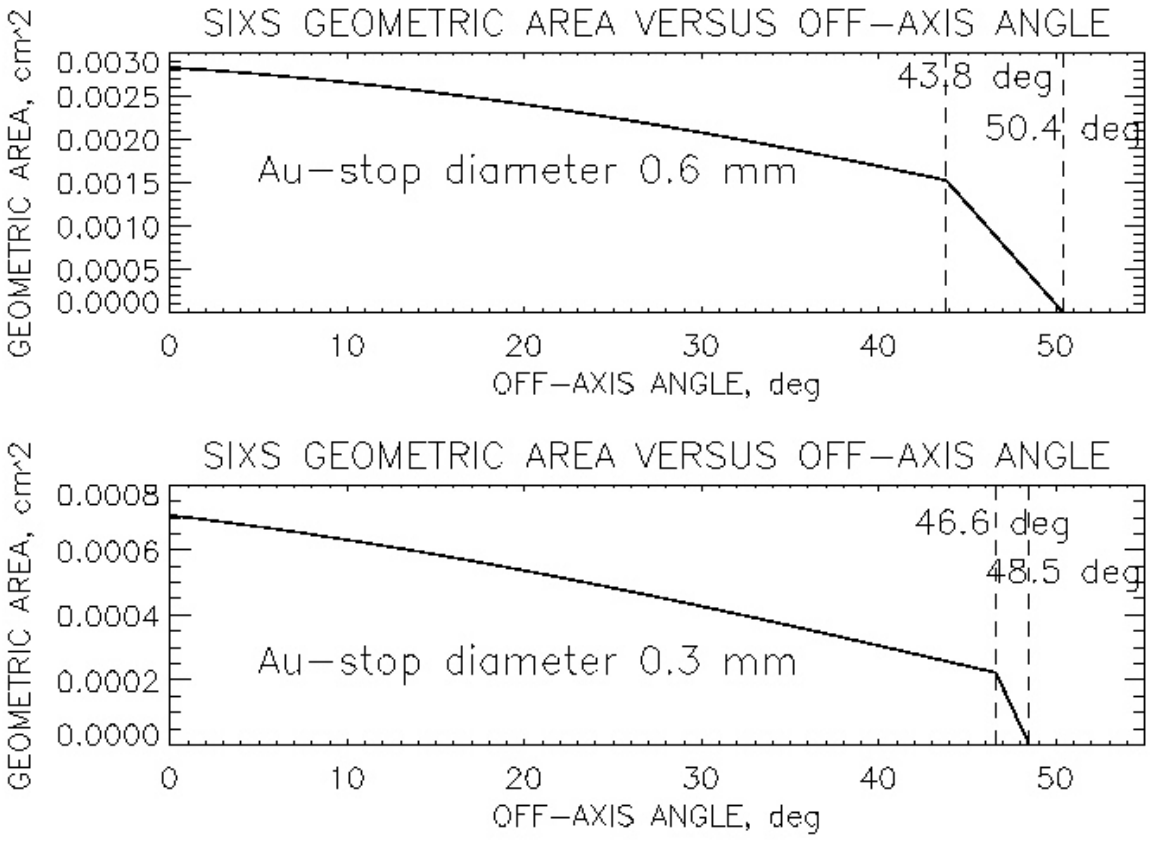

Figure 51: *SIXS geometric areas as a function of θ with H=1.9* mm, *R=2.0* mm *and r=0.6* mm *(on the top) and 0.3* mm *(below). The vertical dashed lines correspond the limits of the region calculated with linear approximation, i.e. the casting of double shadow on the detector plane.*

angle regions between the dashed vertical lines must be rejected in the final data analysis. These off-axis regions are approximated with a linear fit to avoid a confusing triple circle intersection calculation. Both the aperture stop and the entrance aperture cast shadow on the detector between this approximated off-axis region. The steep slopes in these regions reduce the accuracy of the final analysis due to the apparent size of the Sun. This peripheral FoV annulus area for the side detectors is between 46.6° and the limiting off-axis angle of 48.5°, which is insignificant in the operation of the SIXS X-ray side detectors. The respective region for the middle detector PIN is between 43.8° and 50.4°. We should seriously consider the need of performing the FoV sensitivity map ground calibrations. The FoV sensitivity map can be solved from geometrical considerations up to the point, where the entrance aperture begins to cast shadow on the detector active area. This solution would naturally ignore all errors originating from the mechanical tolerances. The solar angular radius seen on the Hermean orbit at about 0.4 AU is 1.25°. The Sun can not therefore be regarded as a point source. This will also reduce the operational limiting off-axis angle. The solar disc must be at least totally inside the detector FoV, if one desires to model the respective detector sensitivity. Taking into account this requirement, the final limiting off-axis angle for the side detectors is 46.6°-1.25°=45.35°. The limiting angle for the middle detector is 42.65° respectively.

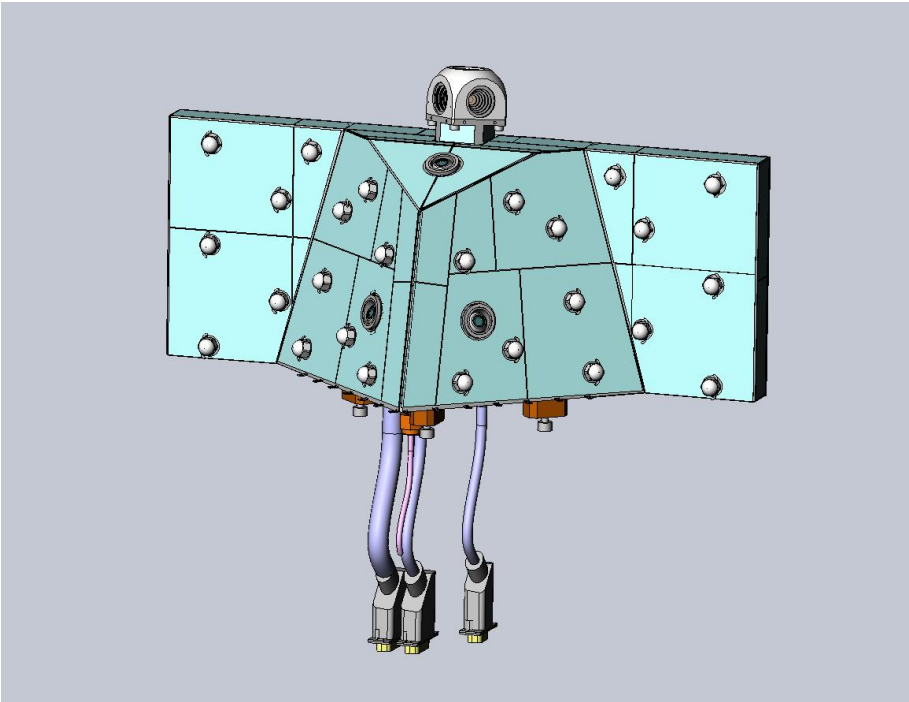

Figure 52: *Technical drawing of BepiColombo SIXS instrument. Picture courtesy of OIA.*

The SIXS mechanical drawing is illustrated in Fig. 52. The "head of the bat" is the particle detector.

8.3 Final conclusions of the solar monitors on-board SMART-1 and Chandrayaan-1

In general, the SMART-1 mission was very successful, considering the data obtained from our first X-ray solar monitor. These data include several hundred hours of high

quality observations of solar B- and C-level solar spectra. The data obtained from the Chandrayaan-1 mission suffered from low signal due to the unexpected low activity of the Sun during this mission. Therefore the aperture stop diameter should have been larger than 0.0379 mm used in XSM. The aperture diameter size was optimized to cover the dynamic range from B- to X-level activity using the experience heritage from the SMART-1 XSM. Only a few C-flares occurred during CH-1 mission and XSM caught three of them. Hence the data for independent coronal science is scarce. However, a fraction of the data will be still applicable for contributing to the Moon fluorescence analysis made by the C1XS science teams at RAL and ISRO.

8.3.1 Ground calibrations

Our instrument team has learned a lot of practical issues, which should be investigated in greater detail during the incoming ground calibrations, e.g. procedures related to the SIXS instrument for BepiColombo. The most significant issue is the control of the detector gain shift as a function of sensor box temperature. A second important issue is to ensure the measurement of X-rays between 1 and 2 keV. There is one new technical solution related to the gain shift. The temperature of the specific component, which causes this phenomenon should be stabilized with an extra Peltier cooler. This will naturally increase the power budget and requires major design change in the existing electronics. A more rational solution would be an accurate thermal test, i.e. the detector electronics could be calibrated at different temperatures at a constant operational PIN temperature, e.g. at -15C°.

8.3.2 Data quality

The flux cross-calibrations with the GOES showed, that SMART-1 XSM measured solar X-ray fluxes at the same energy range with an agreement of 10 %.
There is still plenty of analysis to do with the XSM data, e.g. fitting all the observed flares from the onset down to the declining phase in oder to determine the evolution of temperature and emission measure with time. The two C-glass flare analysis examples introduced in chapter 6 show the power of our solar monitors in deriving the continuum and line emission at once. There are also interesting emission lines seen in the solar flare spectral data, which will be studied in the future.
There were some drawbacks compared to the expected operation of XSM, e.g. the thermal problems, phantom counts and the unused energy range between 1 and 2 keV. The nominal lower end of the energy range of the XSM was designed to be 1 keV. Due to a misunderstanding, the real measured energy range was limited significantly above 1 keV, i.e. about 1.8 keV. This was the worst drawback related to the in-flight operation of the XSM. However, we were able to extrapolate the spectrum in the energy interval between 1 and 2 keV with the aid of spectral fitting done above 1.8 keV (Alha et al. 2008).
The in-flight calibration source activity of the CH-1 XSM was the same as for the SMART-1 XSM, but the measured calibration count rates were significantly lower due to the smaller aperture stopper hole of the CH-1 XSM. The low count rate required longer in-flight calibration integrations to achieve sufficient photon statistic for energy scale and resolution determination.

References

Agostinelli, S., Allison, J., Amakoe, K. A., Apostolakis, J., Araujo, H., Arcel, P. & et al. (2003), 'Geant4-a simulation toolkit', *Nuclear Instruments and Methods in Physics Research Section A* **3**, 250–303.

Alha, L., Huovelin, J., Hackman, T., Andersson, H., Howe, C. J., Esko, E. & Väänänen, M. (2008), 'The in-flight performance of the x-ray solar monitor (xsm) on-board smart-1', *Nuclear Instruments and Methods in Physics Research Section A* **596**, 317–326.

Alha, L., Huovelin, J., Nygård, K., Andersson, H., Esko, E., Howe, C. J., Kellett, B. J., Narendranath, S., Maddison, M. J., Crawford, I. A., Grande, M. & Shreekumar, P. (2009), 'Ground calibration of the chandrayaan-1 x-ray solar monitor (xsm)', *Nuclear Instruments and Methods in Physics Research Section A* **607**, 544–553.

Alig, R., Bloom, S. & Struck, W. (1980), 'Scattering by ionization and phonon emission in semiconductors', *Physical Review B* **22**, 5565–5582.

Arnaud, K. A. (1996), XSPEC: The first ten years, *in* G. Jacoby & J. Barnes, eds, 'Astronomical Data Analysis Software and Systems V', Vol. 101, Astronomical Society of the Pacific, p. 17.

Bhandari, N. (2005), 'Chandrayaan-1: Science goals', *Journal of Earth System Science* **114**, 701.

Blake, R. L., Chubb, T. A., Friedman, H. & Unzicker, A. E. (1963), 'Interpretation of x-ray photograph of the sun', *Astrophysical Journal* **137**, 3.

Bowen, I. S. (1927), 'The origin of the the nebulium spectrum', *Nature* **120**, 473.

Crawford, J., Joy, K., Kellett, B., Grande, M., Anand, M., Bhandari, N., Cook, A. C., d'Uston, L., Fernandes, V. A., Gasnault, O., Goswami, J., Howe, C. J., Huovelin, J., Koschny, D., D.Lawrence, D., Maddison, B., Maurice, S., Narendranath, S., Pieters, C. & T., O. (2009), 'The scientific rationale for the c1xs x-ray spectrometer on india's chandrayaan-1 mission to the moon', *Planetary and Space Science* **57**, 725–734.

Culhane, J. L. & Sanford, P. W., eds (1981), *X-ray Astronomy*, Faber and Faber.

Data (1996), 'X-ray sensor', *GOES I-M data book,NASA Goddard Space Flight Center, Greenbelt, MD, U.S.A* p. 61.

Delaboudinière, J. P., Artzner, G. E., Brunaud, J., Gabriel, A. H., Hochedez, J. F., Millier, F., Song, X. Y., Au, B., Dere, K. P., Howard, R. A., Kreplin, R., Michels, D. J., Moses, J. D., Defise, J. M., Jamar, C., Rochus, P., Chauvineau, J. P., Marioge, J. P., Catura, R. C., Lemn, J. R., Shing, L., Stern, R. A., Gurman, J. P., Neupert, W. M., Maucherat, A., Clette, F., Cugnon, P. & Van Dessel, E. (1995), 'Eit: Extreme-ultraviolet imaging telescope for the soho mission', *Solar Physics* **162**, 291.

DeLuca, E. E., Weber, M. A., Sette, A. L., Golub, L., Shibasaki, K., Sakao, K. & Kano, R. (2005), 'Science of the x-ray sun: The x-ray telescope on solar-b', *Advances in Space research* **36**, 1489–1493.

Dennis, B. R., Phillips, K. J. H., Sylwester, J., Sylwester, B., A., S. R. & Tolbertd, A. K. (2005), 'The thermal x-ray spectrum of the 2003 april 26 solar flare', *Advances in Space Research* **35**, 1723–1727.

Dennis, B. R. & Starr, R. (2008), 'Flare plasma abundances - new x-ray observations', *www.sprg.ssl.berkeley.edu/∼tohban/* .

Eddy, J. (1980), 'The ancient sun, fossil record in the earth, moon and meteotites', *Pergamon Press, New York* p. 119.

Fano, U. (1947), 'Ionization yield of radiations.ii. the fluctuatiosn of the number of ions', *Physical Review* **72**, 26.

Fraser, G. (1989), *X-ray detexctors in astronomy*, Cambridge Astrophysics Series.

Giacconi, R. & Gursky, H., eds (1974), *X-ray Astronomy*, D. Reidel Publishing Company.

Grande, M. (1999), 'The d-cixs x-ray spectrometer on esa's smart-1 mission to the moon', *Earth, Moon, and Planets* **85**, 143.

Grande, M. (2009), 'The c1xs x-ray spectrometer on chandrayaan-1', *Planetary and Space Science* **57**, 725–734.

Grande, M., Kellett, B. J., Howe, C., Perry, C. H., Swinyard, B., Dunkin, S., Huovelin, J., Alha, L., D'uston, L. C., Maurice, S., Gasnault, O., Couturier-Doux, S., Barabash, S., Joy, K. H., Crawford, I. A., Lawrence, D., Fernandes, V., Casanova, I., Wieczorek, M. & Thomas, N. (2009), 'The d-cixs x-ray spectrometer on the smart-1 mission to the moon: First results', *Earth, Moon, and Planets* **57**, 725–734.

Handy, B. N., Acton, L. W., Kankelborg, C. C., Wolfson, C. J., Akin, D. J., Bruner, M. E., Caravalho, R., Catura, R. C., Chevalier, R., Duncan, D. W., Edwards, C. G., Feinstein, C. N., Freeland, S. L., Friedlaender, F. M., Hoffmann, C. H., Hurlburt, N. E., Jurcevich, B. K., Katz, N. L., Kelly, G. A., Lemen, J. R., Levay, M., Lindgren, R. W., Mathur, D. P., Meyer, S. B., Morrison, S. J., Morrison, M. D., Nightingale, R. W., Pope, T. P., Rehse, R. A., Schrijver, C. J., Shine, R. A., Shing, L., Strong, K. T., Tarbell, T. B., Title, A. M., Torgerson, D. D., Golub, L., Bookbinder, J. A., Caldwell, D., Cheimets, P. N., Davis, W. N., Deluca, E. E., McMullen, R. A., Warren, H. P., Amato, D., Fisher, R., Maldonado, H. & Parkinson, C. (1999), 'The transition region and coronal explorer', *Solar Physics* **187**, 229.

Hill, S. M., Pizzo, V. J., Biesecker, D. A., Bornmann, B., Hildner, E., Lewis, L. D., Grubb, L. N., Husler, M. P., Prendergast, K., Vickroy, J., Greer, S., Defoor, T., Wilkinson, D. C., Hooker, R., Mulligan, P., Chipman, E., Bysal, H., Douglas, J. P., Reynolds, R., davis, J. M., Wallace, K. S., Russell, K., Freestone, K., Bagdigian, D., Page, T., Kerns, S., Hoffman, R., Cauffman, S. A., Davis, M. A., Studer, M. A., Berthiaume, F. E., Saha, T. T., Berthiume, G. D., Farthing, H. & Zimmermann, F. (2005), 'The noaa goes-12 solar x-ray imager (sxi) 1. instrument, operations, and data', *Solar Physics* **226**, 225.

Howard, R. A., Moses, J. D., Socker, D. G., Dere, K. P. & Cook, J. W. (2002), 'Sun earth connection coronal and heliospheric investigation (SECCHI)', *Advances in Space Research* **29**, 2017–2026.

Howe, C. J., Drummond, D., Edeson, R., Maddison, B., Parker, D. J., Parker, R., Shrivastava, A., Spencer, J., Kellett, B. J., Grande, M., Sreekumar, P., Huovelin, J., Smith, D. R., Gow, J., C., N. K. & d'Uston, L. (2009), 'Chandrayaan-1 x-ray spectrometer (c1xs) instrument design and technical details', *Planetary and Space Science* **57**, 735–743.

Huovelin, J. (2006), Space weather, *in* S. Maravell, ed., 'Space Science: New Research', Nova Science Publishers Inc, New York, pp. 329–351.

Huovelin, J., Vainio, R., Andersson, H., Valtonen, E., Alha, L., Mälkki, A., Grande, M., Fraser, G. W., Kato, M., Koskinen, H., Muinonen, K., Näränen, J., Schmidt, W., Syrjäsuo, M., Anttila, M., Vihavainen, T., Kiuru, E., Roos, M., Peltonen, J., Lehti, J., Talvioja, M., Portin, P. & Prydderch, M. (2009), 'Solar intensity x-ray and particle spectrometer (sixs)', *Planetary and Space Science* .

Jain, R., Bhatt, L. & Bharti, L. (2001), Solar x-ray spectrometer (soxs) mission: Observations and new results, *in* N. Gopalswamy & A. Battacharyya, eds, 'Solar influence on the heliosphere and Earth's envirinment: Recent progress and prospects', pp. 54–60.

Jain, R., Dave, H. & Desphande, M. R. (2001), Solar x-ray spectrometer (soxs) development at physical research laboratory/isro, *in* B. Battrick & H. Sawaya-Lacoste, eds, 'Solar Encounter: Proceedings of the First Solar Orbiter Workshop', ESA SP-493, Noordwijk: ESA Publications Division, pp. 109–119.

Kellogg, E., Baldwin, J. R. & Koch, D. (1975), 'Studies of cluster x-ray sources. energy spectra for the perseus, virgo, and coma clusters', *ApJ* **199**, 299–306.

Kosugi, T., Matsuki, K., Sakao, T., Shimizu, T., Sone, Y., Tachikawa, S., Hashimoto, T., Minesugi, K., Ohnishi, A., Yamada, T.and Tsuneta, A., Hara, H., Ichimoto, K., Suematsu, T., Shimojo, M., Watanabe, T., Shimada, S., Davis, J. M., Hill, L. D., Owens, J. K., Title, A. M., Culhane, J. L., Harra, L. K., Doschek, G. A. & Golub, L. (2007), 'The hinode (solar-b) mission: An overview', *Solar Phys* **243**, 3–17.

Laukkanen, J., Lämsä, V., Salminen, A., Huovelin, J., Andersson, H., Alha, L., Hämäläinen, K., Nenonen, S., Sipilä, H. & Tillander, M. (2005), 'Radiation hardness studies for the x-ray solar monitor (xsm) onboard the esa smart-1 mission', *Nuclear Instruments and Methods in Physics Research Section A* **538**, 496–515.

Lehtolainen, A. (2009), 'Sixs fov calculation, university of helsinki, department of physics'. Internal report.

Lin, R. P., Dennis, P. R., Hurford, G. J., Smith, D. M., Zehnder, A., Harvey, P. R., Curtis, D. W., Pankow, D., Turin, P., Bester, M., Csillaghy, A., Lewis, M., Madden, N. and. Vanbeek, F., Appleby, M., Raudorf, T., McTiernan, J., Ramaty, R., Schmail, E., Schwartz, R., Krucker, S., Abiad, R., Quinn, T., Berg, P., Hashii, M., Sterling, R., Jackson, R., Pratt, R., Campell, R. D., Malone, D., Landis, D., Barrington-Leigh, C. P., Slassi-Sennou, S., Cork, C., Clark, D., Amato, D., Orwig, L., Boyle, R., Banks, I. S., Shirey, K., Tolbert, A. K., Zarro, D., Snow, F., Thomsen, K., Henneck, R., Mchedlishvili, A., Ming, P., Fivian, M., Jordan, J., Wanner, R., Crubb, J., Preble, J., Matranga, M., Benz, A., Hudson, H., Canfield, R. C., Holman, G. D., Crannell, C., Kosugi, T., Emslie, A. G., Vilmer, N., Brown, J. C., Johns-Krull, C., Aschwanden, M., Metcalf, T. & Conway, A. (2002), 'The reuven ramaty high-energy solar spectroscopic imager (rhessi)', *Solar Physics* **210**, 3–32.

Lyot, P. (1939), 'The study of the solar corona and prominences without eclipses (george darwin lecture, 1939)', *MNRAS* **99**, 580.

Mewe, R., Gronenschild, E. & van den Oord, G. (1985), 'Calculated x-radiation from optically thin plasmas. v', *Astronomy and Astrophysics Supplement Series* **62**, 197.

Orlando, S., Peres, G., Reale, F., Rosner, R. & Hudson, H. (1998), Solar-stellar connection: Relevance of yohkoh data, *in* Donahue & J. A. R. A. Bookbinder, eds, 'The Tenth Cambridge Workshop on Cool Stars, Stellar Systems and the Sun', Vol. 154, ASP Conf., pp. 1130–1137.

Owens, A., Bavdaz, M., Peacock, A., Andersson, H., Nenonen, S., Krumrey, M. & Puig, A. (2002), 'High resolution x-ray spectroscopy using a gaas pixel detector', *Nuclear Instruments and Methods in Physics Research A* **479**, 531.

Owens, A. Frazer, G. W., Abbey, A. F., Holland, A., McCarthy, H., Keay, A. & Wells, A. (1996), 'The x-ray energy response of silicon (b): Measurements', *Nuclear Instruments and Methods in Physics Research A* **382**, 503–510.

Parker, E. N. (1958), 'Dynamics of the interplaentary gas and magnetic fields', *Astrophysical Journal* **128**, 664.

Racca, G. D., Marini, A., Stagnaro, L., van Dooren, J., di Napoli, L., Foing, B. H., Lumb, R., Volp, J., Brinkmann, J., Grunagel, R., Estublier, D., Tremolizzo, E., McKay, M., Camino, E. O., Schoemaekers, J., Hechler, M., Khan, M., Rathsman, P., Andersson, G., Anflo, K., Berge, S., Bodin, P., Edfors, A., Hussain, A., Kugelberg, J., Larsson, N., Ljung, B., Meijer, L., Mortsell, A., Nordeback, T., Persson, S. & Sjoberg, F. (2002), 'Smart-1 mission description and development status', *Planet. Space Sci.* **50**, 1323.

Racca, G. D., Whitcomb, B. G. & Foing, P. H. (1998), 'The smart-1 mission', *ESA bullentin* **95**, 72–91.

Raymond, J. C. & Smith, B. W. (1977), 'Soft x-ray spectrum of a hot plasma', *Astrophysical Journal Supplement Series* **35**, 419–439.

Scelsi, L., Maggio, A., Peres, G. & Pallavicini, R. (2005), 'Coronal properties of g-type stars in different evolutionary phases', *A&A* **432**, 671–685.

Schlemm, C. E., Starr, R. D., Ho, G. C., Bechtold, K. E., Hamilton, S. A., Boldt, J. D., Boynton, W. V., Bradley, W., Fraeman, M. E., Gold, R. E., Goldsten, J. O., Hayes, J. R., Jaskulek, S. E., Rossano, E., Rumpf, R. A., Schaefer, E. D., Strohbehn, K., Shelton, R. G., Thompson, R. E., Trombka, J. I. & Williams, B. D. (2007), 'The x-ray spectrometer on the messenger spacecraft', *Space Sci Rev* **131**, 393.

Schulz, R. & Benkhoff, J. (2006), 'Bepicolombo: Payload and mission updates', *Advances in Space Research* **38**, 572.

Shibata, K. (2002), 'A hertzsprung-russel-like diagram for solar/stellar and corona emission measure versus temperature diagram', *Astrophysical Journal* **577**, 422.

Spieler, H. (2001), 'Radiation detectors and signal processing', *www-physics.lbl.gov* .

Starr, R., Ckark, P. E., Evans, L. G., R., F. S., McClanahan, T. P., Trombka, J. I., Goldsten, J. O., Maurer, R. H., McNutt, R. L. & Roth, D. R. (1999), 'Radiation effects in si-pin detector on the near earth asterois rendezvous mission', *Nuclear Instruments and Methods in Physics Research A* **428**, 209–215.

Starr, R., Clark, P. E., Murphy, M. E., Floyd, S. R., McClanahan, T. B., Nittler, L. R., Trombka, J. I., Evans, L. G., Boynton, W. V., Bailey, S. H., Bhangood, J., Mikheeva,

I., Brückner, J. Squyres, S. W., McCartney, E. M., Goldsten, J. O. & McNutt, R. L. J. (2000), 'Instrument calibrations and data analysis procedures of for the near x-ray spectrometer', *Icarus* **147**, 498–519.

Sze, S. N. (1981), *Physics of semiconductor devices*, John Wiley & Sons.

Tikkanen, T. (1994), 'Characterization of the sixa x-ray spectrometer'. Licentiate thesis.

Vilhu, O., Huovelin, J., Pohjolainen, S., Virtanen, J. & Curdt, W. (2002), 'Microflaring of a solar bright point', *Astronomy and Astrophysics* **395**, 977–981.

Westphal, G. P. (1979), 'On the performance of loss-free counting-a method for real-time compensation of dead-time and pile-up losses in nuclear pulse spectroscopy', *Nucl. Instr. and Meth.* **163**, 189.

Yoshimura, H. (1992), 'The solar dynamo and planetary dynamo', *The cosmic dynamo: proceedings of the 157th Symposium of the International Astronomical Union held in Potsdam; F.R.G.; September 7-11; 1992. Edited by F. Krause, K. H. Radler, and Gunther Rudiger. International Astronomical Union. Symposium no. 157; Kluwer Academic Publishers* .

Appendix 1

A general calculation method of the geometric area for a circular FoV as a function of the off-axis angle θ:

Fig. 19 on the page 26 illustrates this calculation, where *R=D/2* and *r=d/2*.
H is the distance between the lower surface of Au-stop and entrance aperture.
d is the thickness of the Au-stop (125μm).
R is the collimating aperture radius.
r is the aperture stop radius.
θ_1 is the limiting angle of main aperture.
θ_2 is an intermediate angle needed to perform the calculation shown below.
θ_3 is critical angle, i.e. at this angle the whole detector area is in the shadow.

$$\theta_1 = \arctan(\frac{R-r}{H-d})$$

$$\theta_2 = \arctan\sqrt{\frac{R^2-r^2}{H^2-Hd}}$$

$$\theta_3 = \arctan(\frac{R+r}{H})$$

$$A_1 = 2r^2\arccos[\frac{d\tan\theta}{2r}] - \frac{d}{2}\tan\theta\sqrt{4r^2-(d\tan\theta)^2}$$

$$A_{21} = 2r^2\arccos[\frac{d\tan\theta}{2r}] + r^2\arccos[\frac{[(H-d)\tan\theta]^2+r^2-R^2}{2r(H-d)\tan\theta}]$$

$$A_{22} = R^2\arccos[\frac{[(H-d)\tan\theta]^2+R^2-r^2}{2R(H-d)\tan\theta}] - \frac{d}{2}\tan\theta\sqrt{4r^2-(d\tan\theta)^2}$$

$$A_{23} = \frac{1}{2}\sqrt{4r^2[(H-d)\tan\theta]^2-[((H-d)\tan\theta)^2+r^2-R^2]^2} - \pi^2r^2$$

$$A_2 = A_{21} + A_{22} - A_{23}$$

$$A_{31} = r^2\arccos[\frac{(H\tan\theta)^2+r^2-R^2}{2rH\tan\theta}] + R^2\arccos[\frac{(H\tan\theta)^2+R^2-r^2}{2RH\tan\theta}]$$

$$A_{32} = \frac{1}{2}\sqrt{4(rHd\tan\theta)^2-[(H\tan\theta)^2+r^2-R^2]^2}$$

$$A_3 = A_{31} - A_{32}$$

The final geometric area must be calculated piecewise as a function of the off-axis angle θ by applying the above equations as follows.

$$A_{\text{geom}} = A_1 \cos\theta, \ if \ 0 \leq \theta \leq \theta_1$$

$$A_{\text{geom}} = A_2 \cos\theta, \ if \ \theta_1 < \theta \leq \theta_2$$

$$A_{\text{geom}} = A_3 \cos\theta, \ if \ \theta_2 < \theta \leq \theta_3$$